Towards Understanding the Influence of Surface Integrity on Mechanical Behavior of Additively Manufactured Ti-6Al-4V

by

Nabeel Ahmad

A dissertation submitted to the Graduate Faculty of
Auburn University
in partial fulfillment of the
requirements for the Degree of
Doctor of Philosophy

Auburn, Alabama
August 9, 2025

Keywords: Additive manufacturing, Surface Texture, Fatigue, Ti-6Al-4V, Failure analysis

Approved by

Nima Shamsaei, Chair, Philpott-WestPoint Stevens Distinguished Professor, Department of Mechanical Engineering
Shuai Shao, McWane Associate Professor, Department of Mechanical Engineering
Robert L. Jackson, Albert Smith Jr. Professor, Department of Mechanical Engineering
Daniel Silva, Assistant Professor, Department of Industrial and Systems Engineering
Aleksandr Vinel, Associate Professor, Department of Industrial and Systems Engineering

Abstract

Additively manufactured components often exhibit shorter fatigue lives in their unmachined state compared to machined or wrought counterparts mainly due to the presence of surface micro-notches. While post-processing treatments can improve performance, they increase lead times, may not always be feasible or desired, and can compromise the advantages of AM, such as near-net shape fabrication. This dissertation aims to investigate the influence of surface integrity on the mechanical behavior of laser powder bed fused (L-PBF) Ti-6Al-4V specimens. First, a novel framework was developed to quantify surface micro-notches using X-ray computed tomography, where key geometrical features such as width, depth, opening angle, and radius of curvature were captured. These features were then combined in the fatigue stress concentration formula, K_f, to assess the fatigue criticality of each notch. It was found that the crack-initiating features ranked within the top 1% of all notches based on the calculated K_f. Fatigue life predictions, employing the fatigue notch factor approach that incorporated localized geometrical features of micro-notch, demonstrated reasonable accuracy for unmachined L-PBF Ti-6Al-4V specimens. This framework was then further validated for conditions where process parameters were systematically varied (i.e., specifically, combination of different infill and contour parameters), and a wide range of surface and near-surface conditions were produced. Moreover, the modelling approach was further applied to partially treated specimens to assess its broader applicability. The results demonstrated that the developed fatigue modelling framework could reasonably predict lives across a wide range of surface textures including partially treated specimens. In addition to modelling, the influence of a wide range of surface conditions on the mechanical performance was investigated. Results showed that avoiding contour passes increased surface roughness and reduced tensile ductility due to early void nucleation. While contour passes enhanced fatigue life for default and underheated infill settings, this beneficial effect was diminished for overheated conditions due to increased roughness and near-surface defects. Moreover, the impact of surface material removal methods, including direct polishing, shallow machining and polishing, deep machining (DM), and deep machining with polishing (DM+P) on the mechanical performance was evaluated. The results showed that polishing alone did not improve tensile behavior and fatigue resistance due to persistence of surface valleys, while DM and DM+P improved tensile ductility and fatigue life by removing surface and near-surface defects.

Acknowledgments

I would like to sincerely thank my Ph.D. advisor, Dr. Nima Shamsaei, for his unwavering support, patience, and mentorship throughout this journey. His guidance, both technical and personal, shaped my development as an independent researcher. I am also sincerely thankful to Dr. Shuai Shao, who, in addition to serving on my committee, offered guidance, sharp, insightful feedback that challenged me to think more critically and write more clearly. His guidance enriched my work in ways I will carry forward beyond this dissertation. My heartfelt thanks also go to Dr. Robert L. Jackson and Dr. Daniel Silva for serving on my committee and for their time, feedback, and encouragement during FAA meetings. I am equally grateful to Dr. Aleksandr Vinel for serving as the university reader, offering thoughtful input during the FAA discussions, and providing valuable input at the final stage of this process. I would like to offer gratitude to Dr. Jeffrey Suhling and Dr. Hareesh Tippur, Chair and Associate Chair of Graduate Studies in the Department of Mechanical Engineering, for their continued support and assistance over the past six years.

I am also incredibly thankful to my PhD colleagues, post-doctoral associates, and research engineers at the National Center for Additive Manufacturing Excellence (NCAME) for their unlimited support, both professionally and personally, in completion of this work. Finally, I dedicate this dissertation to my family who have stood by me through every step of this long journey: my mother, Surraya Begum; my father, Muhammad Ashiq, who patiently waited six years without seeing me; and my wife, Maria Nasir, whose unwavering love and support carried me through the difficult times. This achievement is as much theirs as it is mine.

Table of Contents

List of Tables

List of Figures

List of Equations

Abbreviations

AM	Additive manufacturing/Additively manufactured
BM	Block maxima
DM	Deep machining
DM+P	Deep machining and polishing
EVT	Extreme value theory
GEV	Generalized extreme value
HCF	High cycle fatigue
HIP	Hot isostatic pressing
KDE	Kernel density estimation
KH	Keyholes
LCF	Low cycle fatigue
LoF	Lack of fusion
L-PBF	Laser powder bed fusion/fused
MLE	Maximum likelihood estimation
N/OH	No overhang method
OH	Overhang method
OM	Optical microscopy
P	Polishing
PDF	Probability density function
SEM	Scanning electron microscopy/microscope
SM+P	Shallow machining and polishing
UT	Untreated
UTS	Ultimate tensile strength
XCT	X-ray computed tomography
YS	Yield strength

Nomenclature

α	Opening angle of notch
C1	No-contour and default infill
C2	No-contour and keyhole
C3	No-contour and lack of fusion
C4	Default-contour and default infill
C5	Default-contour and keyhole
C6	Default-contour and lack of fusion
C7	Single-contour and default infill
C8	Beam-offset and default infill
d	Depth of notch
EL	Elongation to failure
ε_f	Strain at fracture
γ	Material's characteristic length
K_f	Fatigue notch factor
K_t	Stress concentration factor
μ	Mode of distribution
$N_f/2N_f$	Cycles/Reversals to failure
ρ	Radius of curvature
$\bar{\rho}$	Effective radius of curvature
R_σ	Stress ratio
R_v/S_v	Maximum valley depth of the profiled line/surface
S_{vb}	Maximum pit/valley depth from each block
σ_e	Endurance limit of machined and polished specimens
σ_e^D	Fatigue limit of defective specimens
σ_e^{um}	Endurance limit of unmachined specimens
σ_{max}	Maximum applied stress
w	Width of notch

1 Introduction

The ability of additive manufacturing (AM) to fabricate parts in layer-by-layer fashion has enabled design freedom over conventional fabrication techniques for producing parts with complex geometries [1,2]. In addition, it allows part consolidation and combines what would traditionally be multi-component assemblies into a monolithic structure. A prominent example is the GE fuel nozzle, where several individual parts were consolidated into one integral part that reduced weight by ~25% and improved cost efficiency by ~30% [3,4]. Moreover, the ability of AM to manufacture and operate in remote locations such as in space or on battlefields significantly reduces the logistical challenges and supports rapid production and deployment of essential components. For example, the army's "Rapid Fabrication via Additive Manufacturing on the Battlefield (R-FAB)" lab demonstrated on-demand fabrication in isolated areas and operational readiness [5].

Among various AM techniques, laser powder bed fusion (L-PBF) stands out as it provides good dimensional accuracy compared to other technologies due to relatively fine laser spot sizes, thin layer thickness (20 to 200 μm), and small hatch distances [6]. These characteristics make L-PBF a potential candidate to replace the conventional manufacturing in many practical applications. Nonetheless, laser powder bed fused (L-PBF) parts in their as-fabricated state often have high roughness and are prone to contain volumetric defects such as lack of fusion (LoF), gas-entrapped pores (GEP), and keyholes [7–9]. Both the micro-notches on the surface and volumetric defects serve as stress risers with the former being more detrimental one. Even in the presence of volumetric defects, cracks often favor initiation from the rough surface of unmachined specimens; consequently, the mechanical performance of unmachined parts is often inferior compared to their wrought counterparts [9].

To address these issues, various post-processing treatments such as hot isostatic pressing (HIP) and surface treatments (e.g., machining) are often adopted. However, these treatments typically come with trade-offs: they increase the lead time and cost and may not always be effective in improving fatigue behavior. For instance, heat treatment followed by HIP has been shown to lead to pore regrowth in the material volume [10,11] and machining can unintentionally open near-surface defects to the surface, which may cause early fatigue crack initiation and reduce the fatigue life [1]. In fact, machining may not be feasible, desired, or practical in some complex geometries such as internal flow channels and lattice structures [12,13]. This makes it even more important to understand the effects of surface texture, specifically surface features most critical to mechanical performance, for the adoption of AM technologies in fatigue-critical applications.

Historically, standard surface texture parameters defined in ISO 25178-2021 [14–17] have been used to quantify the severity of surface roughness. Among them, the maximum valley depth, R_v, and maximum areal valley depth, S_v, have been reported to adequately capture the severity of the surface micro-notches. This usage is based on its definition of maximum pit height relative to the mean line and the fact that in-plane micro-notches greatly influence the crack initiation behavior. These parameters have been reported to be effective in estimating the fatigue behavior of conventionally manufactured parts [18]. However, in the context of AM, there are some inconsistencies: while some studies [19] have found good correlation of S_v with fatigue life, others have reported weak correlation [20,21]. This discrepancy could be due to the fact that fatigue-critical stress concentrations are influenced not just by depth but also by other geometric factors like notch sharpness.

Notably, the standard parameters tend to provide an overall description of the surface texture parameter and ignore the localized nature of fatigue damage. While advanced approaches such as combining X-ray computed tomography (XCT) with finite element analysis could be utilized [22], their computational costs make them unsuitable for routine batch analysis. This gap in understanding has also been recognized in America Makes and ANSI Additive Manufacturing Standardization Collaborative (AMSC) roadmap; specifically, Gap D23 “Documentation of New Functional Surface Features” has been identified as medium priority, with the need for further research and development [23]. Therefore, identification of the most critical surface roughness characteristics that influence the mechanical performance of L-PBF parts is essential for advancing their reliable use in fatigue-critical applications.

The surface texture of L-PBF parts can greatly vary, mainly due to differences in thermal history, which are influenced not only by process parameter adjustments but also by local geometry and location within the same build. Specifically, thermal history of a material point is partially governed by the thermal dissipation pathways available to it during fabrication [1,24,25]. Accordingly, even with the manufacturer’s recommended process settings, factors such as the local part size, geometry, and build orientation can make the thermal history of a part highly heterogeneous. As a result, parameters optimized for small witness coupons may not scale effectively to larger or more complex components [25]. Still, the standard practices typically employ manufacturer’s recommended process parameters uniformly across the part without considering variation in thermal and resulting effects on the surface texture.

Beyond the variability in the surface texture, the widespread adoption of L-PBF is hindered by the operational issues of slow build rates and low productivity [26]. This bottleneck poses a challenge for high-volume manufacturing. A potential strategy to enhance productivity is to increase the build rates by adjusting the process parameters (e.g., increasing laser speed and either reducing or avoiding contour passes altogether) in the non-critical regions of the component.

However, such adjustments in process parameters will influence the surface texture and in turn mechanical performance. Therefore, a better understanding of how process variation influences surface and near-surface features, and subsequently mechanical behavior, is needed.

A key advantage of AM is its ability to fabricate near-net shape geometries without the need for additional post-processing. To leverage this benefit, particularly in fatigue critical applications, it becomes crucial to develop an understanding of the surface texture in the unmachined state for material qualification and standardization. This has traditionally been achieved through extensive mechanical testing and generating MMPDS-style databases for material qualification [23,27], a prohibitively expensive approach. On the other hand, the fatigue prediction models could potentially circumvent or minimize these efforts, particularly in situations where experimental fatigue data is limited, while also supporting the qualification and standardization efforts. For L-PBF parts, there are mainly two primary approaches adopted in literature for modelling of unmachined L-PBF parts: (1) evaluation of the stress concentration induced by surface anomalies [16,20] (2) estimation of the empirical or equivalent initial flaw size approach of the surface features proposed by Murakami [28–30]. While Murakami's framework is reasonably effective for estimating fatigue behavior, its application typically requires fatigue testing and fractography to measure defects size. This may not be a robust approach, considering these defects can also be measured non-destructively using XCT.

Since fatigue cracks predominantly initiate from the surface micro-notches, it may be more practical and scalable to non-destructively identify and evaluate stress concentration directly from surface texture and correlate it with fatigue behavior (Approach 1). While optical and line profilometers can capture surface texture, they often fail to detect hidden valleys, sharp features, and near-surface defects common in the complex surface topography and material volume of AM parts. By leveraging the ability of XCT to capture the surface and subsurface defects, there is a need for a non-destructive framework to predict fatigue life of specimens with prominent roughness. Addressing this gap would greatly accelerate material qualification efforts and reduce the dependence on costly physical testing.

1.1 Project Goal and Objectives

The overall goal of this dissertation is to understand the influence of surface integrity on the tensile and fatigue behaviors of L-PBF Ti-6Al-4V. This alloy was selected because of its popularity and widespread use across critical engineering sectors including aerospace, automotive, and medical industries, and its well-known sensitivity to both surface and volumetric defects, which is largely attributed to its fine microstructure [11,31].

To accomplish this goal, several objectives have been established. The **first objective (Chapter 2)** is to determine the critical surface features affecting the fatigue behavior of Ti-6Al-4V. As part of this objective, it is hypothesized that using XCT to capture and quantify the geometrical features of micro-notches (e.g., width, depth, opening angle) will better identify fatigue-critical surface features than surface roughness metrics (Hypothesis 1a). Moreover, fatigue life predictions incorporating localized geometrical features of micro-notches will be more accurate than those based on conventional surface texture parameters (Hypothesis 1b). The **second objective (Chapter 3)** is to assess the individual and combined influences of different infill and contour process parameters on the surface texture and near-surface conditions and in turn, their tensile and fatigue behaviors. For this objective, it is hypothesized that avoiding contour passes will deteriorate surface quality and decrease mechanical performance (Hypothesis 2a). Moreover, deviating from recommended infill conditions will exacerbate surface texture and further reduce mechanical performance (Hypothesis 2b). The **third objective (Chapter 4)** is to evaluate the influence of surface texture and material removal on the tensile and fatigue behaviors. For this objective, it is hypothesized that direct polishing alone is insufficient to enhance fatigue and tensile performance (Hypothesis 3a). Moreover, fatigue life predictions using a notch factor approach that incorporates localized geometrical features of micro-notches can more accurately estimate fatigue lives of surface-treated specimens (Hypothesis 3b).

1.2 Outline of Dissertation

Surface micro-notches inherent in the unmachined L-PBF specimens act as stress risers, which cause early fatigue crack initiation and significantly reduce the fatigue strength. Conventional roughness metrics, however, provide only an overall description of surface texture and often overlook the localized features that drive fatigue crack initiation. Therefore, understanding the most influential surface features affecting fatigue behavior is needed. To address this gap, Chapter 2 provided the methodology developed to capture and quantify the critical surface features affecting the fatigue performance of L-PBF Ti-6Al-4V. First, surface topographies of unmachined specimens were characterized using the XCT. A novel method was then developed to extract key geometrical attributes of individual micro-notches such as depth, width, opening angle, and radius of curvature. Moreover, fatigue life was modeled using a fatigue notch factor approach, wherein the most severe micro-notch, identified through the extracted geometrical attributes, was used as the representative crack initiation site.

Although L-PBF is widely used, its industrial adoption is constrained by low productivity and a lack of understanding of how process-induced surface variations, especially those resulting from local changes in thermal history of a part or within a build or parameter adjustments in non-critical regions, affect mechanical performance. Chapter 3 addressed this knowledge gap and examined how combination of variations in contour strategies and infill parameters influence surface texture and, in turn, tensile and fatigue behaviors. A wide range of surface conditions was generated by systematically modifying both the infill and contour parameters. In addition to the analyses of tensile and fatigue results, fatigue lives were also modeled using the approach described in Chapter 2.

There is uncertainty about how much material should be removed from AM part during post-processing to eliminate surface and near surface defects without compromising structural integrity of part or incurring excessive machining efforts. Chapter 4 explored various forms of surface material removal and resulting changes in the surface texture and mechanical performance. In addition to surface characterization and mechanical testing and analyses, a fatigue notch factor approach utilized in Chapter 2 was validated for specimens with prominent roughness.

Chapter 5 revisited the objectives and hypotheses from each study presented in Chapter 2,3, and 4 to highlight the overarching goal of this work: understanding the influence of surface integrity on the surface texture and mechanical behavior of L-PBF Ti-6Al-4V. The chapter provided the key findings in relation to the hypotheses presented in Chapter 1. In addition, it described potential future research directions and developments.

1.3 Broader Impact

The findings and approach developed in this research will help AM communities understand how mechanical performance can be influenced by the process and post-processing surface and near-surface condition. More importantly, by identifying the most critical surface features and their impact on fatigue strength, the need for costly and extensive mechanical testing campaigns across various processing and post-processing conditions can be significantly reduced when establishing design allowable. The XCT based NDE method of capturing geometrical features of micro-notch could potentially facilitate development of new surface texture metrics which are specifically more representative of the AM surface texture compared to traditional surface texture parameters. The results obtained in various material removal conditions will assist designers in deciding optimal depth of material removal for AM components. Additionally, the application of XCT based NDE framework provided in this work can be leveraged by AM communities to establish and improve the current industrial practices for qualification of AM parts. Finally, the dataset generated for L-PBF Ti-6Al-4V for a range of processing and post-processing conditions will be made publicly available to support further research and application development.

2 Determining critical surface features affecting fatigue behavior of additively manufactured Ti-6Al-4V [8]

2.1 Introduction

Additive manufacturing (AM) can fabricate complex geometries that are challenging to manufacture using traditional fabrication techniques [1,6]. The ability to produce near-net shape parts with minimal post-processing is also one of its key advantages. However, additively manufactured (AM) parts often exhibit high surface roughness in their as-fabricated state [20,32,33], which can adversely affect the mechanical performance of the parts, necessitating post-processing (i.e., machining or other surface treatments) to achieve the desired mechanical properties and reliability in service [16,34,35]. However, post-processing treatments are costly and increase lead times, negating AM's potential benefits.

The challenges are especially prominent when dealing with AM parts with complex geometries and/or with internal structures [36]. These intricate designs can severely limit access to machine tools, making conventional surface treatment methods (such as machining and grinding) extremely difficult, if not impossible [37,38]. Even more specialized methods that do not require a line-of-sight tool access (such as abrasive flow machining) can encounter challenges for thin channel features which restricts the transport of working media, resulting in inconsistent surface finish quality [39,40]. The extreme difficulty and uncertain outcome of surface treatments often do not justify their significant cost [16,32], and AM parts are sometimes used without additional surface treatments. Therefore, it is crucial to understand the effect of surface roughness, particularly that of the critical surface features, on the fatigue behavior of AM parts. This is especially needed for materials that exhibit elevated notch sensitivity, such as Ti-6Al-4V [1,31,41].

The surface micro-notches on the unmachined surfaces of AM parts create stress concentration zones that can accelerate fatigue crack initiation [9,42]. These micro-notches have consistently initiated fatigue cracks and been confirmed through both conventional fractography[1] and more advanced techniques such as the "Entire Fracture Surface Approach" by Macek et al. [43,44] and "Fracture Surface Topography Analysis (FRASTA)" by Kobayashi and Shockey [45,46]. Historically, surface roughness parameters have been used to describe the texture of surfaces and, among them, the maximum valley depth, R_v, and maximum areal valley depth, S_v, have the potential to capture the severity of the surface notches based on their definition as the maximum pit height relative to the mean line on the surface [47,48]. Nevertheless, while both R_v and S_v have been effective for estimating the fatigue behavior of conventionally manufactured specimens [17,49], they do not always correlate well with the fatigue life of AM parts [19]. In fact, significant discrepancy exists in the literature regarding the efficacy of these roughness parameters, with some studies on L-PBF Ti-6Al-4V [19] and Inconel 718 [50] showing an adequate inverse correlation between S_v and fatigue life, while others report poor correlation [20,21,51,52]. Moreover, a proper explanation or reconciliation of this discrepancy appears to be lacking.

On one hand, this may be because the stress concentration of the micro-notches cannot be described by their depth alone and can depend on other features, such as their sharpness. On the other hand, the use of standard surface roughness parameters extracted for limited surface areas to provide an overall estimation of surface state may fail to capture the most critical surface features for crack initiation. In this regard, while the identification of most critical surface notches for each part can be in principle possible by combining 3D finite element analysis and X-ray computed tomography (XCT) [22,28,53], the computational cost may be prohibitively expensive, limiting this practice to small scanned volume, making it impractical for batch analysis.

Recent studies have attempted to address the detrimental aspects of surface notches by incorporating some descriptors of their sharpness, such as the root radius, into consideration of relevant surface roughness parameters [54–57]. Pegues et al. [54] demonstrated that by combining surface roughness parameters with the radii of ten deepest micro-notches, the overall stress concentration of unmachined AM parts can be assessed and their fatigue lives can be estimated. This approach, however, relies on manual measurement of radii of surface valleys which may be susceptible to operator error. In the approach proposed by Lee et al., [20] the estimation of the notch root radius was simplified to an effective radius calculated from the layer thickness of the AM process. However, the adoption of the effective radius assumed a reasonably uniform surface notch shape throughout the part and overlooked the shapes and criticalities of individual valleys. In reality, the topography of AM surfaces is complex and surface notch geometry varies significantly depending on their formation mechanism, e.g., stair casing, spatters, partially melted powder particles, or overhang structures [33].

This study aimed to identify, using a fracture mechanics based approach, the surface features most critical to the fatigue behavior of laser powder bed fused (L-PBF) Ti-6Al-4V specimens in unmachined surface condition. In doing so, a novel approach for characterizing surface texture by capturing both surface and sub-surface features using XCT was introduced, and the identified critical surface features were shown to correlate with fatigue life. Ti-6Al-4V was selected not only because of the high notch sensitivity in its fatigue behavior, but also due to its popularity among the AM research community and industry practitioners. The surface topographies of the specimens, along with any hidden, sub-surface features, were captured with

XCT. Each surface valley or notch in the scanned volume was analyzed, and notch parameters such as width, w, depth, d, opening angle, α, and radius of curvature, ρ, were computed. These parameters were then combined using a classical stress concentration formula to assess the severity of each notch. By analyzing the stress concentration factor (K_t) associated with each notch, a classical fatigue notch factor approach was used to predict the fatigue life of stress-relieved L-PBF Ti-6Al-4V specimens.

This paper is structured as follows: after the introduction, Section 2 describes the experimental procedures; Section 3 provides results, including surface texture, defect analysis, and fatigue behavior; Section 4 presents the discussion of results; Section 5 discusses the approach to identify critical surface features; Section 6 attempts to estimate fatigue life of Ti-6Al-4V with the critical surface features; finally, conclusions are drawn in Section 7.

2.2 Experimental Procedures

2.2.1 Fabrication and Processing Conditions

In this study, the plasma atomized Ti-6Al-4V powder, supplied by AP&C, with its chemical composition detailed in **Table 1**, was used. The morphology of the powder particles captured using a scanning electron microscope (SEM) is presented in **Figure 1(a)**, showing they were predominantly spherical with an average particle size of 25 μm (see **Figure 1(b)**). These results were consistent with the nominal particle size range of 15-53 μm provided by the AP&C. All the fatigue specimens were manufactured via the laser powder bed fusion (L-PBF) process in an EOS M290 machine in argon shielding gas. The geometry and build layout of these specimens are shown in **Figure 1(c)** and **1(d)**, respectively. The build layout was provided to ensure repeatability and reproducibility of this article. Notice that the geometry slightly deviated from the ASTM E466 standard [58], i.e., the gage length of the specimens was reduced to 5 mm. This modification was made to permit the XCT of the entire gage section, while maintaining a reasonable resolution. During fabrication, the build plate density was kept below 25%, following the EOS recommendations, to prevent excessive spatter.

Note that several sets of unmachined specimens were fabricated, each with process parameters differing from the EOS-recommended settings. These infill and contour parameters covered a range of energy inputs from high to low, inducing varying volumetric pores and surface textures. This approach diversifies the morphology of surface micro-notches and ensures the robustness of the fatigue model predictions. Another set of near-net shape specimens, which were oversized by 2 mm with respect to the dimensions in **Figure 1(c),** was fabricated using EOS-recommended process parameters (see **Table 2**). These specimens were machined and polished to the dimensions shown in **Figure 1(c)** and tested to serve as the reference data for fatigue modeling purposes (see **Section 2.6**). Following fabrication, the specimens were stress relieved on the build plate at 704°C for 1 hr and then removed from it using a bandsaw.

Table 1 The chemical composition of the plasma atomized powder reported by AP&C.

Element	O	Al	V	Fe	C	N	H	Y	Ti
Min (Wt.%)	–	5.5	3.5	–	–	–	–	–	Balance
Max (Wt.%)	0.2	6.75	4.5	0.3	0.08	0.05	0.02	0.01	

Table 2 EOS M290 recommended process parameters for Ti-6Al-4V.

Laser power (W)	Laser speed (mm/s)	Hatch distance (mm)	Layer thickness (mm)	Scan Strategy	Scan rotation
280	1200	0.14	0.03	Stripe	67°

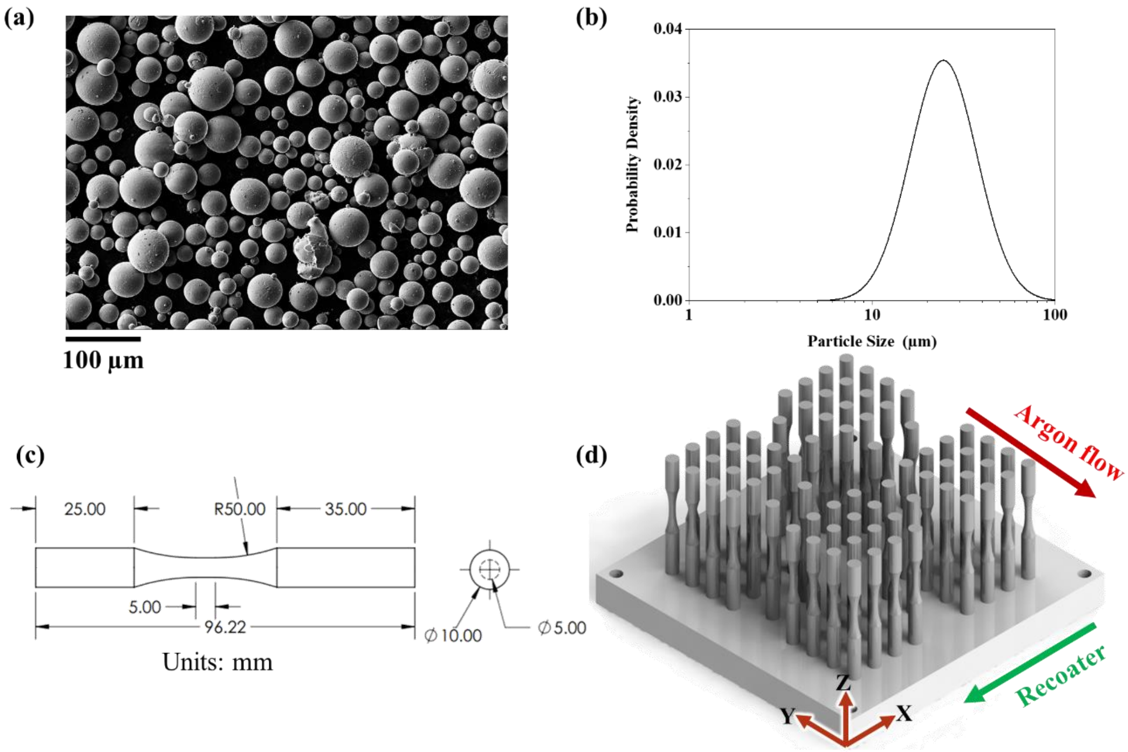

Figure 1 (a) The morphology of powder particles, (b) powder size distribution, (c) geometry of the fabricated specimens, and (d) build layout.

2.2.2 Surface Texture and Defect Analysis

The surface texture and the volumetric defect distribution of all the fabricated specimens were evaluated at their gage sections by employing a Zeiss Xradia 620 XCT system. The scans utilized an accelerating voltage of 140 kV and 0.4X objective lens, and had a voxel size of 5.3 µm. For each scan, the total scanned volume was ~108 mm^3. The Zeiss proprietary software was used for the reconstruction. Defect analysis was performed using the ImageJ software, while the defects were visualized in 3D using the Dragonfly software.

To analyze the surface texture, the reconstructed stacks of images, initially on the radial planes, were first resliced to create the images on a series of longitudinal planes revolving about the specimens' long axis using the ImageJ software. **Figure 2(a)** illustrates the process of obtaining 2D images via longitudinal reslicing. The longitudinal planes were spaced $\Delta\theta$ apart, calculated as the arc angle of 1voxel size at the specimen perimeter (i.e., $\Delta\theta \approx$ voxel size/radius of specimens), which was determined to be 0.0023 rad or 0.13° in this study. This spacing ensured that the fine surface features were not lost due to the reslicing process.

Subsequent operations (see **Figure 2(b)**) were performed using the in-house Python code. These began with applying Gaussian filtering to blur the images and reduce noise which was followed by binarizing the grayscale images using a minimum error thresholding algorithm [59]. This algorithm was able to effectively capture narrow valleys without introducing noise. Other thresholding algorithms, such as Otsu and Triangle [60,61], were tested but could not capture the valleys or introduced excessive noise (see **Section S1** in Suppl. Mat. for more details). Then, the binarized slices were visually inspected, and any noisy features with a size of 3 pixels or smaller and located away from the surface were removed. Line profiles from each longitudinally resliced image were then obtained by repeating one of the following two procedures at each voxel position along the specimen axis (see **Figure 2(c)**):

(1) Overhang (OH) approach: counting black pixels from the top of each image down to the first white pixel, marking a surface profile point;
(2) No overhang (N/OH) approach: counting white pixels from bottom till the first black pixel, marking a surface profile point.

Notice that OH approach is akin to traditional tactile profilometer and optical roughness measurement methods in that it measures surface texture "looking" from above. The line profiles were stacked to create the 3D areal maps of the scanned surfaces (see **Figure 2(d)**). These maps were then rolled back onto a cylindrical geometry by converting the surface height deviations from cartesian coordinates into radial deviations relative to the specimen's base radius (see **Figure 2(e)**).

Extreme value theory (EVT), which models extreme events and makes predictions based on the observed extremes, was employed to investigate the statistical distribution of the surface features. The block maxima (BM) methodology was used for the analysis with EVT, which divided the surfaces into two-dimensional blocks, allowing for the selection of the deepest point from each block to create a distribution of extreme values. The Gumbel distribution was selected to represent the statistics of the deepest surface valleys, expressed as [62]:

$$f(x) = \frac{1}{\sigma} exp\{-(x - \mu)\sigma - exp(-(x - \mu)\sigma\}, \qquad \text{Eq. (1)}$$

where μ indicates the mode of the distribution of the valleys, while σ represents the scale of the distribution of the valleys. Gumbel distribution is well-suited for this study due to its exponential decay in the tail, suggesting a virtual bound for the deepest valley, although this bound is not precisely known. For analysis, each scanned surface was subdivided into 1200 blocks, each with an equal size of 250 × 250 μm^2 (see **Figure 2(e)**). The Gumbel distribution was fitted to the maximum valley depth from each block, S_{vb}, values extracted from different blocks for each specimen using maximum likelihood estimation (MLE). The parameters of the Gumbel distribution, μ and σ, were estimated using the following relation [62]:

$$f(\hat{\mu}, \hat{\sigma})_{MLE} = \underset{(\mu, \sigma)}{\arg max} \prod_{i=1}^{n} \frac{1}{\sigma} \exp\left\{-\frac{x_i - \mu}{\sigma}\right\} \exp\left\{- \exp\left\{-\frac{x_i - \mu}{\sigma}\right\}\right\}, \qquad \text{Eq. (2)}$$

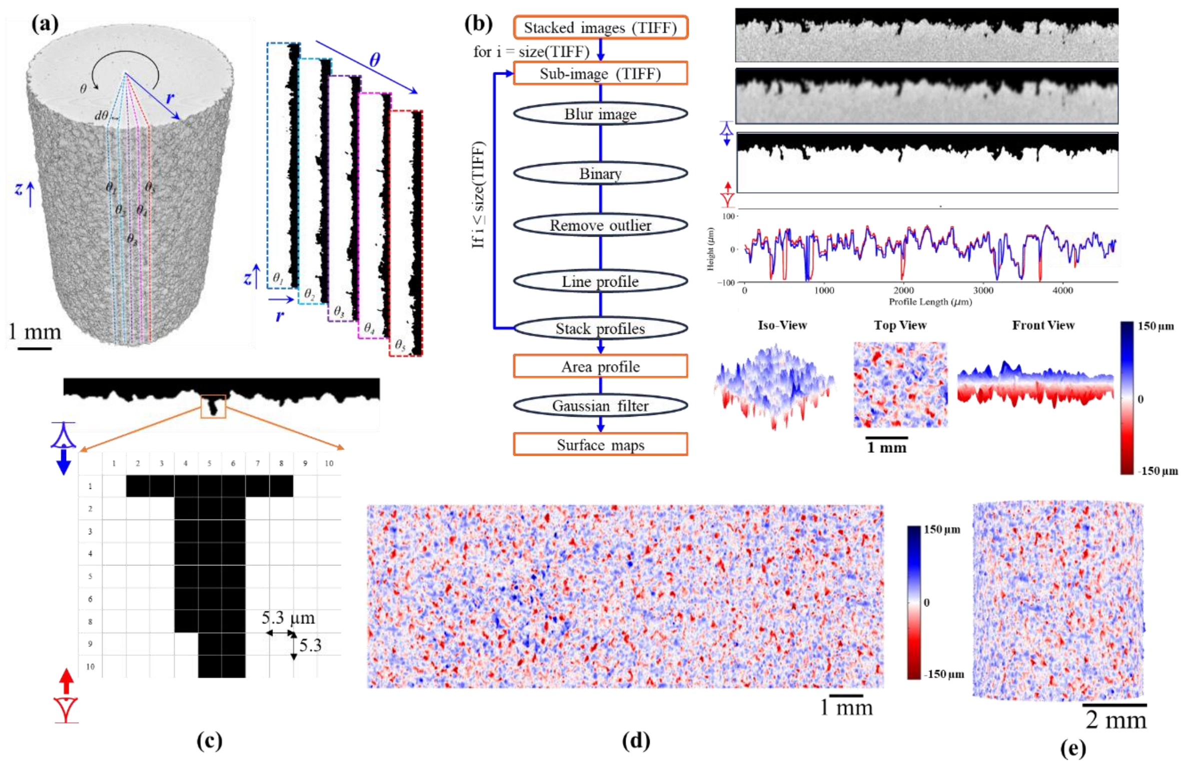

Figure 2 Overview of the approach used for surface texture analysis of specimens from XCT images: (a) schematic of longitudinal reslicing, (b) flowchart of the Python code, (c) a magnified resliced surface showing the top and bottom views, (d) unrolled surface subdivided into 1200 blocks, and (e) depiction of a rolled surface.

2.2.3 Capturing Micro-Notch Parameters

An in-house Python code was developed to obtain notch parameters such as w, d, α, and ρ from each surface micro-notch. Notch parameters were computed from the gage, covering approximately 30,000-35,000 valleys. The workflow of the algorithm is shown in **Figure 3**. First, line profile from Slice i (also called Profile i) was smoothed using a Gaussian filter with a kernel size of 1.5 to remove outliers. All peaks (i.e., the points above the mean line) were first eliminated to reduce the computational time in the subsequent steps. Valley j was then identified on Profile i and the depth, d, and the width, w, of the valley were stored. The maximum valley depth, S_v, was then determined by identifying the lowest value from the set of all recorded depths.

The radius of curvature, ρ, at the root of each Valley j, was calculated from the fitted ellipse, i.e., $\rho = a^2/b$, where b is the semi-major axis and a is the semi-minor axis. The fitting of the ellipse was only to the points in the vicinity of the valley's deepest point defined by the closest inflection point on the valley's profile (i.e., the point where the valley profile changed from convex to concave). Detailed procedures, including finding the inflection points via cubic spline, selection of points for fitting the ellipse, and the actual ellipse fitting, are provided in **Section S2** of the Suppl. Mat. The opening angle, α, of the Valley j was defined as the angle between two straight lines fitted to its two walls. Valley walls were between the valley's deepest point and the nearest local maxima. More details on the calculation of the opening angle, α, are also provided in **Section S2** of the Suppl. Mat.

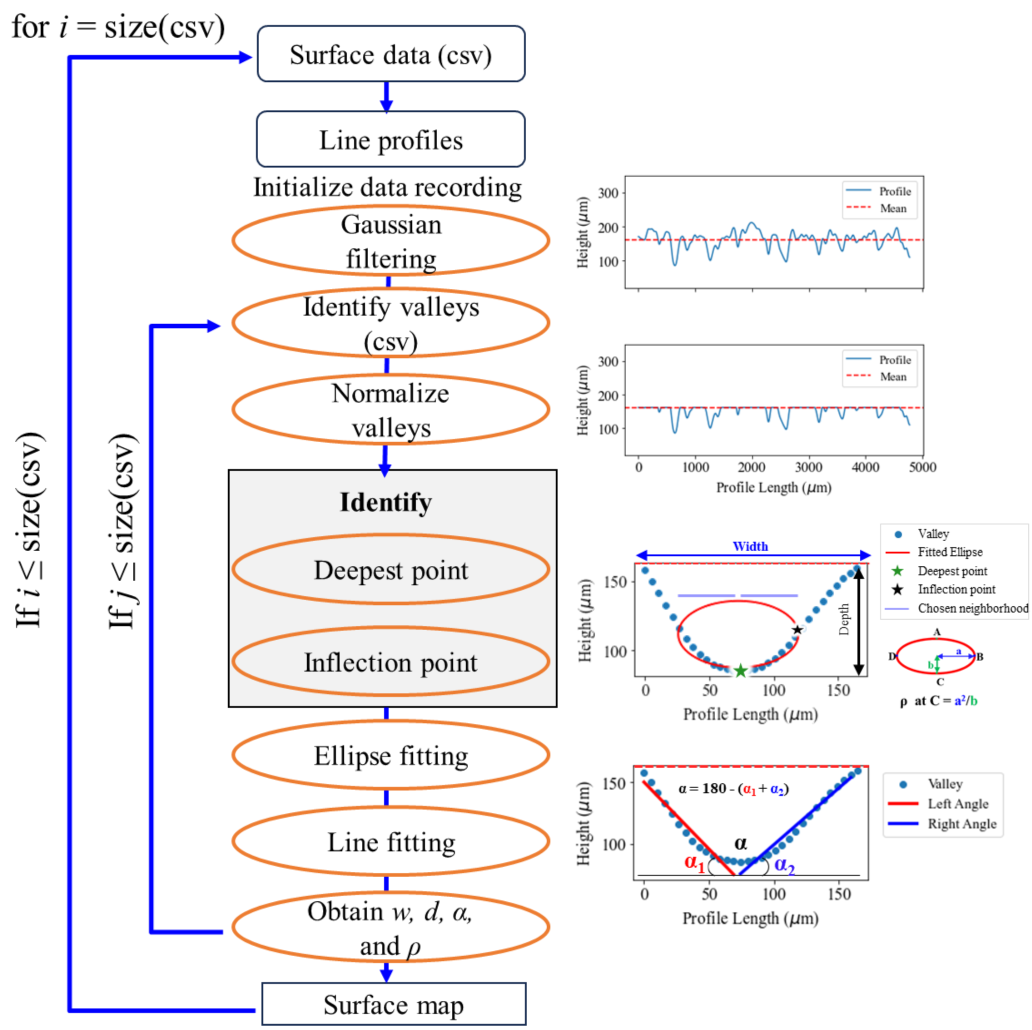

Figure 3 Workflow proposed to obtain surface micro-notch parameters.

2.2.4 Fatigue Testing and Fractography

The force-controlled fatigue testing was performed using MTS Landmark and MTS Bionix Tabletop loading frames, following the ASTM E466 standard [58], at the stress ratio (R_σ) of 0.1. The tests on unmachined specimens were conducted at the maximum applied stresses of 300, 250, and 225 MPa to investigate the fatigue behavior especially in high cycle fatigue regimes. On the other hand, specimens in machined & polished condition were tested at 850, 800, 700 and 600 MPa (see results in **Section S4** of the Suppl. Mat.). The loading was applied as sinusoidal waveforms until either fracture (i.e., complete specimen separation) or up to 10^7 reversals, in which case the test was considered a runout. The fractured specimens were inspected using a Zeiss Crossbeam 550 scanning electron microscope. Before scanning electron microscopy (SEM), the fracture surfaces were thoroughly cleansed to eliminate contaminants.

2.3 Experimental Results

2.3.1 XCT Analysis

XCT was performed on all fabricated specimens before testing and the results were analyzed. For brevity, **Figure 4** presents results for one specimen as an example, i.e., AB1 in **Table 3** of fatigue results. The volumetric defect analysis for specimen AB1 is visualized in **Figure 4(a)** and **4(b)**. As seen, many volumetric defects were detected in the sub-surface regions of the specimens, where they exhibited a range of morphologies from relatively smooth, spherical to more irregularly shaped, as observed in the enhanced images. When these defects are present near surface valleys, they may amplify the detrimental effects of surface texture, further reducing the mechanical performance of a part, particularly its fatigue resistance in the high cycle regime [28,63,64].

The surface texture of the same specimen obtained using the N/OH and OH methods is shown in **Figure 4(c)** and **4(d),** respectively. **Figure 4(e)** and **4(f)** exhibit the complete gage surface of the same specimen in the rolled state obtained from both N/OH and OH methods, respectively. In the figures, the surface topography is shown using color maps in both unrolled and rolled states, where blue and red indicate the peaks and valleys, respectively. As evidenced by the areal maps, the N/OH method resulted in a significantly higher S_v value of 145 μm compared to the OH method, which measured a value of 110 μm of the same specimen. This notable difference indicated the strong influence of overhang structures on the measured surface texture values. The

N/OH method could assess the surface texture from a specimen's interior toward the free surface, thus enabling the detection of deep valleys that might otherwise be hidden or obscured by overhang structures, while they are detrimental to the mechanical performance. For Ti-6Al-4V specimens examined in this study, these overhang structures were frequently partially melted powder particles, which created a superficial layer that could be interpreted by the OH method as the surface itself, leading to an underestimation of the actual valley depths. In this sense, the N/OH method appeared to be superior, and the larger S_v values it reported was regarded as being more reflective of the true surface characteristics of specimens. Moreover, deeper valleys detected by the N/OH method could be sites of severe stress concentration, potentially leading to crack initiation under cyclic loading.

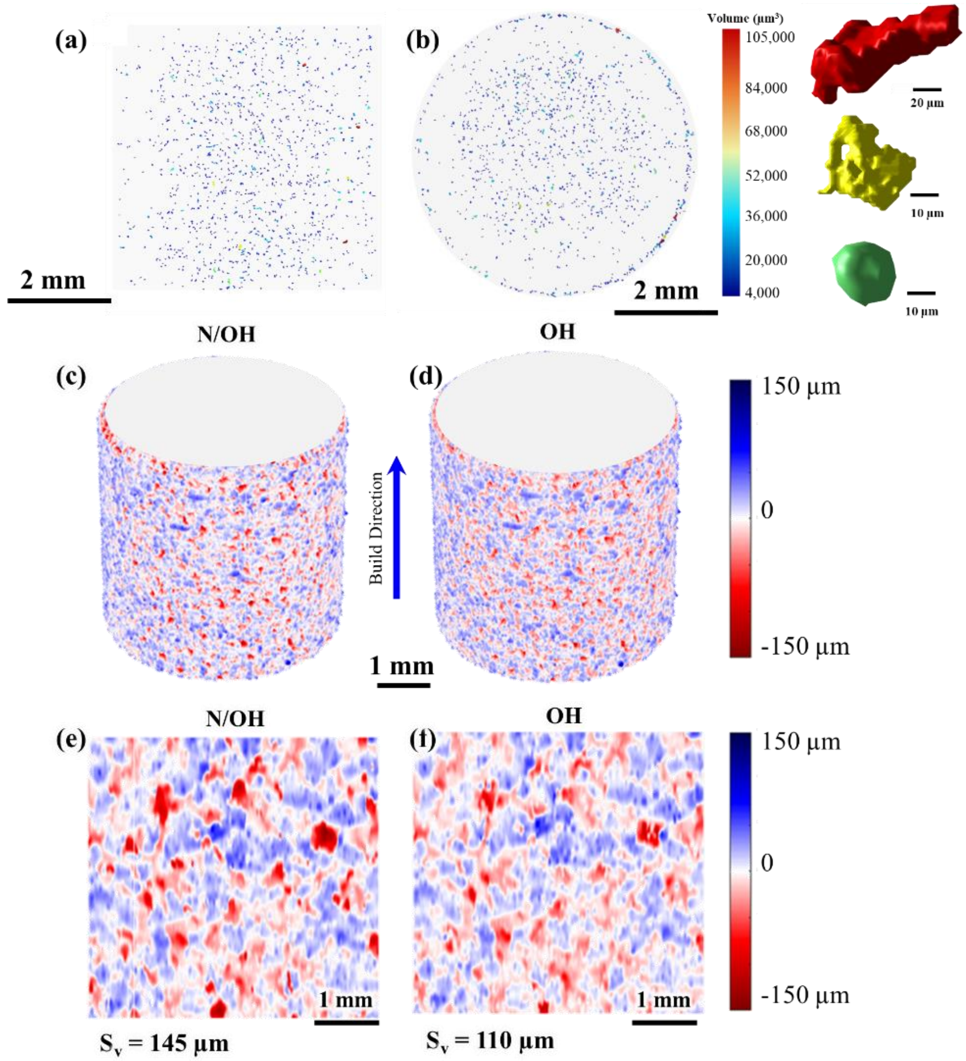

Figure 4 3D visualization of volumetric defects and surface texture obtained from XCT at the gage section of a fatigue specimen: (a) front view and (b) top view of the scanned volume exhibiting volumetric defects. The largest defects by volume are highlighted alongside 3D figures. (c) and (e) show the rolled and unrolled 3D surface maps using the N/OH method, while (d) and (f) show the rolled and unrolled surface textures obtained using the OH method, respectively.

2.3.2 Fatigue Results and Fractography

A summary of stress-life results at three different maximum applied stresses (σ_{max}) of 300, 250, and 225 MPa as well as corresponding S_v values from both OH and N/OH methods are reported in **Table 3**. Moreover, a visual representation of stress-life results is exhibited in **Figure 5**. The runout datapoints are indicated by black arrows. As shown, at the lower stress levels of 250 and 225 MPa, the fatigue lives of specimens exhibited considerable scatter, exceeding an order of magnitude. In contrast, the specimens tested at higher stress level of 300 MPa showed significantly less fatigue life variations. This difference in the scatter of fatigue lives across different stress levels was attributed to the different mechanisms of crack initiation and propagation that dominated at these varying levels of applied stress [65]. At 300 MPa, the material experienced more severe local cyclic plastic deformation at the roots of the numerous surface micro-notches, which accelerated the crack initiation stage. The remainder of the fatigue life was largely governed by crack growth. Crack growth rates typically depend on microstructure and are insensitive to surface micro-notches [32,54,66]. As a result, fatigue life of the specimens, which had consistent microstructures thanks to an identical stress relief heat treatment applied, tended to vary less.

On the other hand, at the lower stress levels of 250 and 225 MPa, the crack initiation stage was less accelerated and became a more significant portion of the overall fatigue life. The lower applied stress made the crack initiation more selective to occur from only the most detrimental surface micro-notches and other imperfections [63,67]. However, the presence and severity of these micro-notches varied with their size and geometry from specimen to specimen, leading to the observed scatter in fatigue lives. Notably, significant gaps in fatigue life of almost an order of magnitude existed between the fractured and runout specimens at these stress levels.

Table 3 Force-controlled (stress-life) fatigue testing results along with S_v values obtained using OH and N/OH methods, respectively.

Condition	**Spec. ID**	**σ_{max}**	**$2N_f$**	**S_v (OH)**	**S_v (N/OH)**
Unit		**MPa**		**μm**	**μm**
Unmachined	AB11	300	672896	65	89
	AB13	300	577454	105	182
	AB2	300	519264	78	141
	AB16	300	472310	62	92
	AB7	300	437906	73	140
	AB6	300	427210	114	135
	AB5	300	413498	72	146
	AB4	300	388874	121	117
	AB8	300	377664	77	82
	AB10	300	366854	162	174
	AB3	300	364304	126	135
	AB1	300	328404	121	138
	AB15	300	321124	164	171
	AB9	300	307268	164	169
	AB12	300	296370	157	178
	AB14	300	229336	155	198
	AB19	250	>10000000	88	98
	AB23	250	>10000000	96	103
	AB38	250	>10000000	81	98
	AB40	250	>10000000	69	74
	AB18	250	1396446	82	140
	AB24	250	1278890	136	158
	AB28	250	1185380	109	120
	AB41	250	1184866	73	124
	AB36	250	1109226	76	122

Condition	Spec. ID	σ_{max}	$2N_f$	S_v (OH)	S_v (N/OH)
Unit		MPa		µm	µm
	AB43	250	1100676	115	122
	AB21	250	1020808	131	194
	AB27	250	992064	120	124
	AB37	250	873160	132	127
	AB35	250	872516	111	121
	AB17	250	856310	110	122
	AB29	250	849420	72	169
	AB30	250	824008	126	173
	AB22	250	762258	113	158
	AB34	250	740878	126	133
	AB31	250	738448	85	117
	AB20	250	729046	75	128
	AB26	250	727304	124	129
	AB33	250	695216	112	171
	AB32	250	647850	88	111
	AB25	250	620206	122	123
	AB42	250	545066	148	134
	AB39	250	509538	110	121
	AB50	225	>10000000	79	67
	AB51	225	>10000000	84	56
	AB52	225	>10000000	86	73
	AB53	225	>10000000	89	69
	AB54	225	>10000000	73	73
	AB45	225	1625180	121	136
	AB47	225	1372066	113	191
	AB48	225	1046092	133	132

Condition	Spec. ID	σ_{max}	$2N_f$	S_v (OH)	S_v (N/OH)
Unit		**MPa**		**µm**	**µm**
	AB46	225	830074	127	122
	AB49	225	825062	129	150
	AB44	225	451328	70	123
Machined & Polished	M1	600	>10000000	1	1
	M2	600	>10000000	-	-
	M4	600	>10000000	-	-
	M7	700	>10000000	-	-
	M10	700	>10000000	-	-
	M11	700	5532068	-	-
	M6	800	2743912	0.8	0.8
	M3	850	1038632	-	-
	M5	800	2434226	-	-
	M8	850	2766772	-	-
	M9	850	2279460	-	-

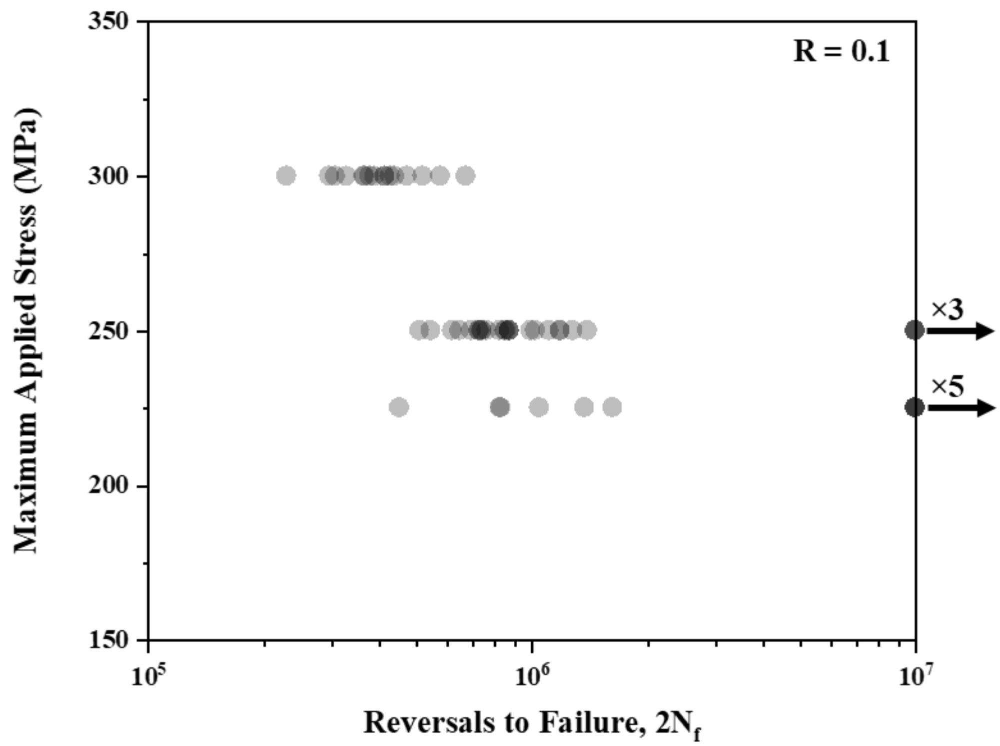

Figure 5 Stress-life results at R = 0.1. The arrows indicate runout specimens.

Selective fracture surfaces for specimens tested at maximum applied stresses of 300 and 250 MPa, along with an enhanced view of the crack initiation sites, are presented in **Figure 6**. The fractography revealed that, across all analyzed fracture surfaces, cracks consistently initiated from surface micro-notches, regardless of the σ_{max}, indicating that surface micro-notches were highly influential in the initiation of fatigue cracks. The figure further showed that multiple crack initiation sites were frequently present on the fracture surfaces. These initiation sites were predominantly associated with surface valleys. Some near-surface volumetric defects were also observed in the proximity of surface defects (see **Figure 6(j)**). These near-surface defects have been shown to facilitate fatigue crack initiation [63,64]. The presence of multiple initiation sites indicated that several cracks initiated simultaneously or in close succession at different sites on the surface and, as the cracks extended, they began to coalesce, or merge, with one another. Initiation site did not always reside on the same plane; therefore, when several cracks coalesced, step-like features (or rachet marks) formed, as evident in **Figure 6(c) and 6(f)**. Since each crack grew over a smaller area, the fatigue life was expected to be shortened by this multi-crack mechanism.

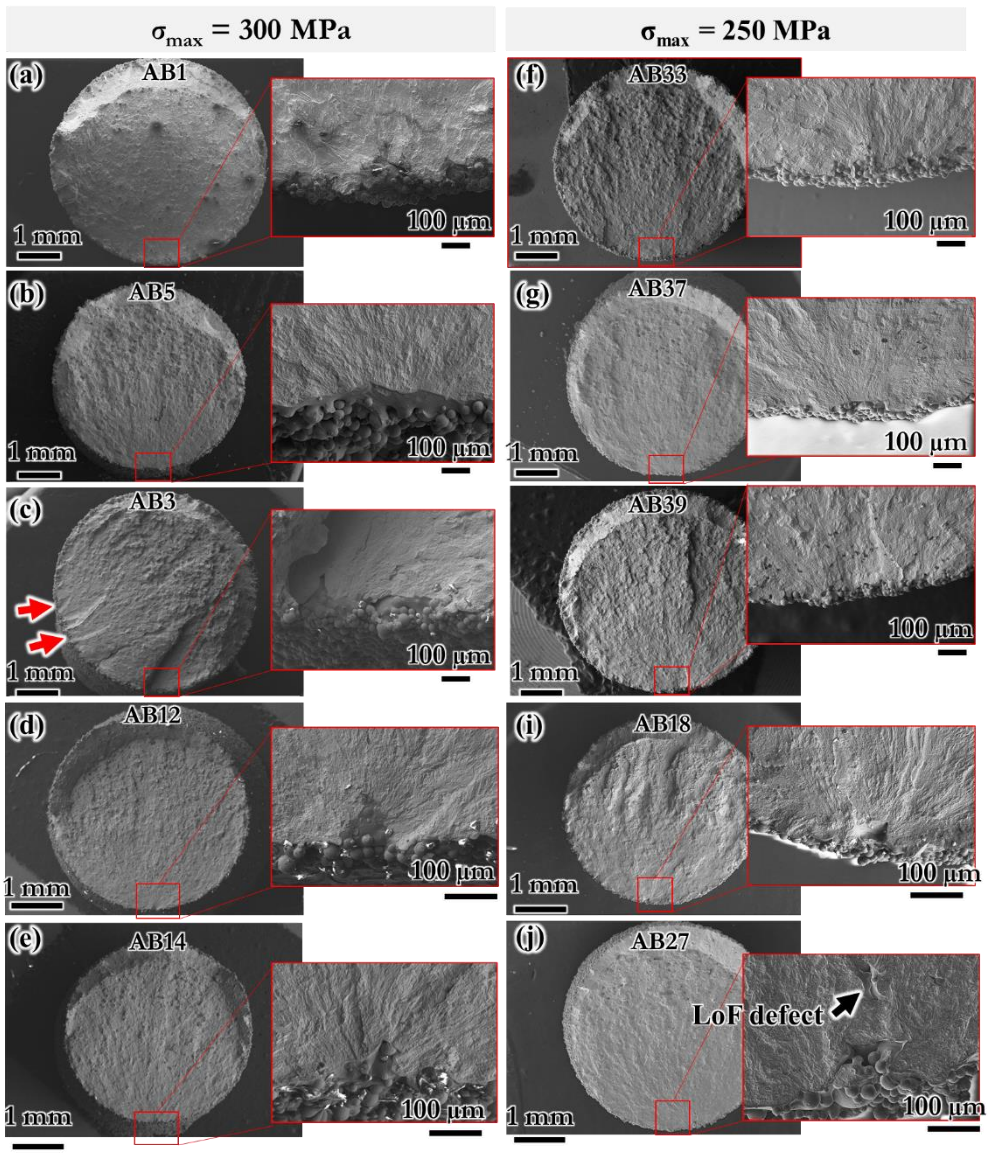

Figure 6 Fatigue fracture surfaces of some specimens fractured at (a)-(e) 300 MPa and (f)-(j) 250 MPa.

2.4 Discussion

2.4.1 Effectiveness of S_v as A Fatigue Resistance Indicator

The fatigue data presented earlier in **Figure 5** is replotted in **Figure 7** to examine any potential relationship between S_v and fatigue life. Note that the size of each bubble in **Figure 7(a)** and **7(b)** corresponds to the S_v of a specimen calculated via OH and N/OH methods from the XCT scan result, respectively. The S_v values obtained from the OH method did not show any clear correlation with fatigue lives (**Figure 7(a))**, including at the lower stress levels of 250 and 225 MPa, where more influence from surface condition was expected. Notably, among the fractured specimens tested at 225 MPa, higher S_v values paradoxically resulted in longer fatigue lives. Moreover, some specimens with similar S_v values as the fractured ones were runouts, further indicating that S_v does not correlate well with fatigue life. This is because the OH method functions similarly to optical systems and line profilometers, which may overlook hidden valleys, especially deeper ones obscured by overhang structures.

The S_v values obtained from the N/OH method showed a slightly better correlation with fatigue life (**Figure 7(b))**. Notably, it could effectively differentiate runout and fractured specimens tested at 250 and 225 MPa, i.e., the runout specimens consistently had S_v < 100 µm, while the fractured ones had S_v > 100 µm. This is further analyzed via EVT of the scanned surface (see following paragraphs). However, this surface texture parameter did not correlate well with fatigue life among the fractured specimens. This lack of correlation was more evident at the stress levels of 250 and 225 MPa. A more detailed evaluation of S_v's predictive accuracy will be presented in **Section 2.6**.

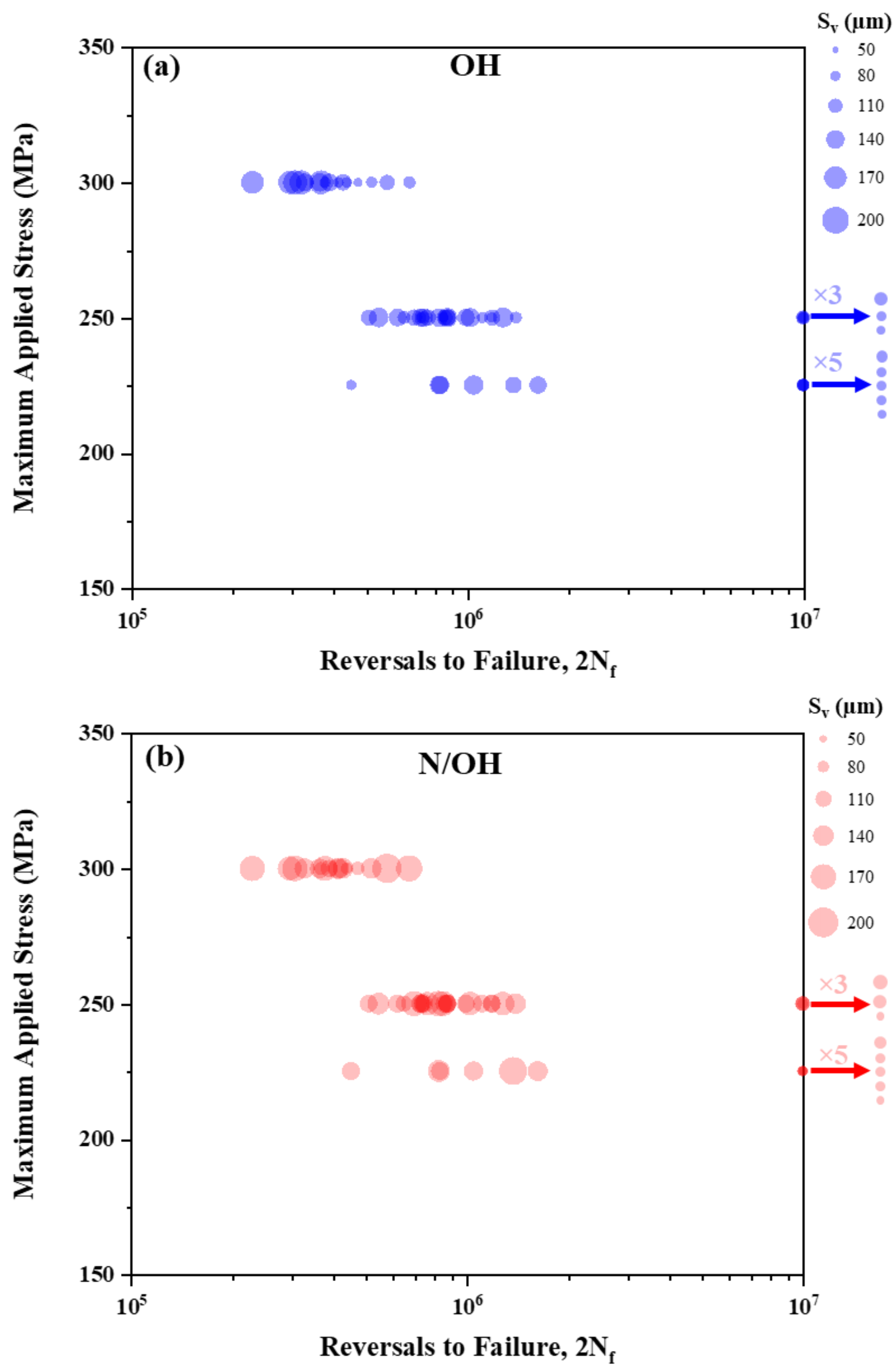

Figure 7 Bubble plots examining the correlation between S_v and fatigue life. The size of each bubble represents the S_v value, which was obtained from the XCT scans using the (a) OH and (b) N/OH methods.

The maximum valley depth from each block, S_{vb}, of selected specimens from the 250 MPa stress level (three runouts: Specimens AB19, AB38, and AB40, and three fractured: Specimens

AB33, AB35, and AB25) were further analyzed via the EVT with BM methodology to understand the differentiating surface characteristics of the runout specimens from the fractured ones, which were responsible for the clear gap in fatigue life. **Figure 8(a)** and **8(b)** present the probability density function (PDF) plots of S_{vb} of the specimens calculated from the XCT scans using the OH and N/OH, respectively. The PDFs were fitted according to Gumbel distribution using MLE, and the σ and μ parameters for each specimen are listed in **Table 4**.

Table 4 Gumbel distribution parameters σ and μ for selected fractured and runout specimens, obtained using both OH and N/OH methods.

Spec. ID	OH		N/OH	
	μ	σ	μ	σ
Runout #1 (AB19)	36.65	6.58	28.96	5.51
Runout #2 (AB38)	26.51	4.69	24.88	4.42
Runout #3 (AB40)	31.68	5.49	29.60	5.09
Fractured #1 (AB33)	52.65	14.97	58.70	17.46
Fractured #2 (AB25)	54.73	15.38	61.29	18
Fractured #3 (AB35)	39.53	12.13	46.32	17.67

The PDF plots from the OH method showed that some S_{vb} values overlapped in both the runouts and fractured specimens (see **Figure 8(a)**). In addition, the fractured specimens exhibited, in general, a larger σ compared to the runouts (see **Table 4**). Upon employing the N/OH method, the PDF curves of the fractured specimens shifted slightly towards greater S_{vb} values (see **Figure 8(b)**), and more distinction between runouts and fractured specimens could be noticed. This was due to the ability of the N/OH method to remove the overhang structures and capture the hidden valleys. According to the N/OH method, the fractured specimens had an even wider distribution, with larger σ and μ values (see **Table 4**), indicating a higher frequency of deeper valleys, with almost two-thirds of the S_{vb} values larger than 50 μm. Therefore, the likelihood of crack initiation from these valleys was higher than in runouts, where the vast majority of valleys were well below 50 μm.

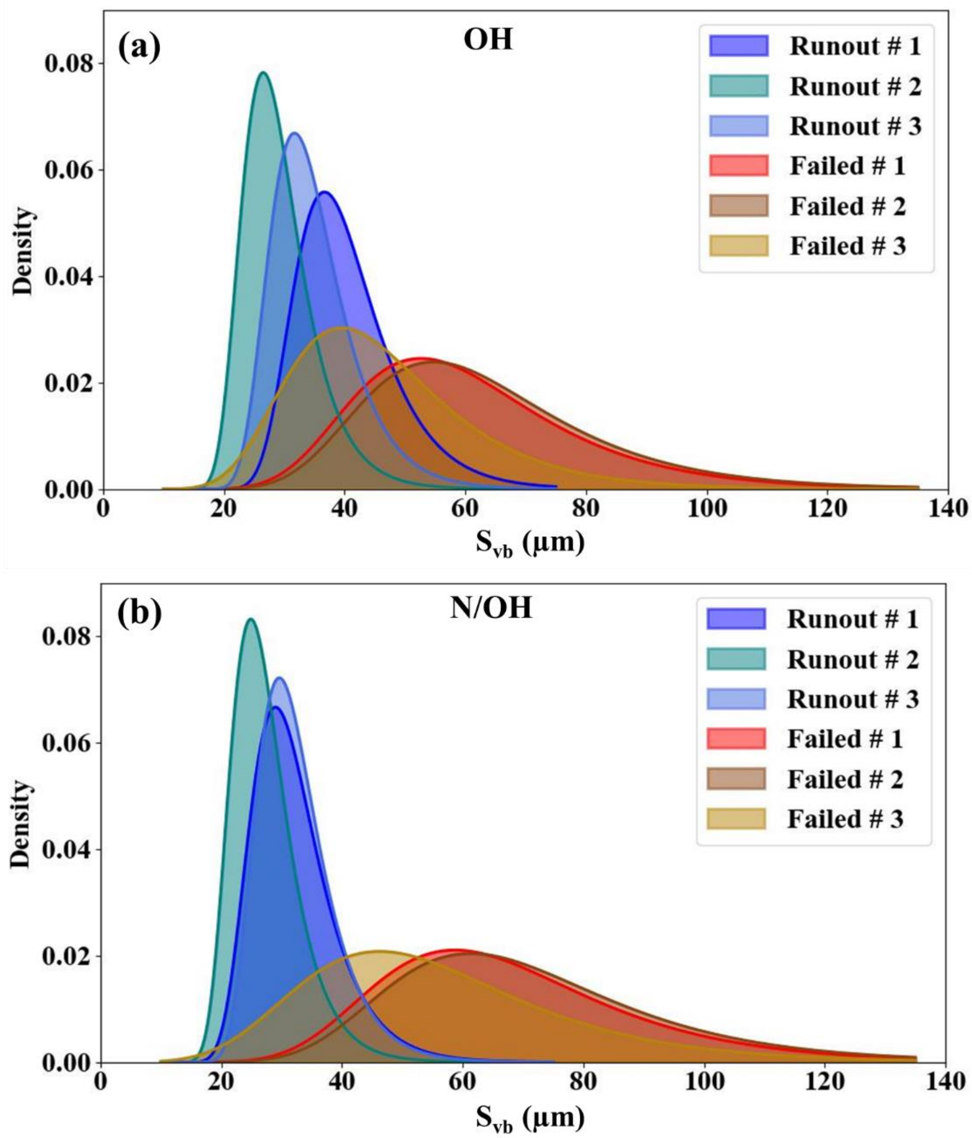

Figure 8 PDF curves of S_{vb} values for runouts and fractured specimens fatigued at 250 MPa: (a) S_v values obtained from the (a) OH and (b) N/OH methods.

Although the S_v values obtained from the N/OH method could somewhat differentiate between runouts and fractured specimens, this factor failed to explain the variations among the fractured specimens. To investigate the lack of correlation between S_v values and fatigue lives of the fractured specimens, post mortem analysis was performed on two specimens (AB16 and AB32) via both XCT and SEM to examine the crack initiating surface features (see **Figure 9**). The locations of these features have also been identified on the specimen surfaces reconstructed from

XCT scans performed before testing, whose topographies are visualized in **Figure 9(d)** and **9(j)** using the N/OH methodology and indicated using black rectangle and magnified views. The histograms of S_v derived from the BM analysis of the surface topographies according to EVT for the specimens are shown in **Figure 9(f)** and **9(l)**. Interestingly, the maximum S_v measured for the AB16 specimen tested at 300 MPa was 92 μm, while the fatigue crack initiated from the surface valley with a depth of 25 μm, which corresponded to the most populous S_v in the histogram (see **Figure 9(f)**). Similarly, AB32 specimen tested at 250 MPa exhibited a crack initiating valley depth of 86 μm, while its maximum S_v was 111 μm (see **Figure 9(l)**). This confirmed that fatigue cracks did not initiate at the location where maximum valley depth was encountered (i.e., where S_v corresponded to); instead, they often initiated from surface valleys whose depth situated between the most populous depths (i.e., the peaks of the histograms) and the maximum valley depth (i.e., the trailing edges of the histograms).

The analysis revealed that S_v, while appealing due to its simplicity and ease of measurement, has limitations that become evident in the context of AM parts, where surface topography can be irregular and complex. Relying solely on S_v might oversimplify the true nature of the surface features and their impact on mechanical performance.

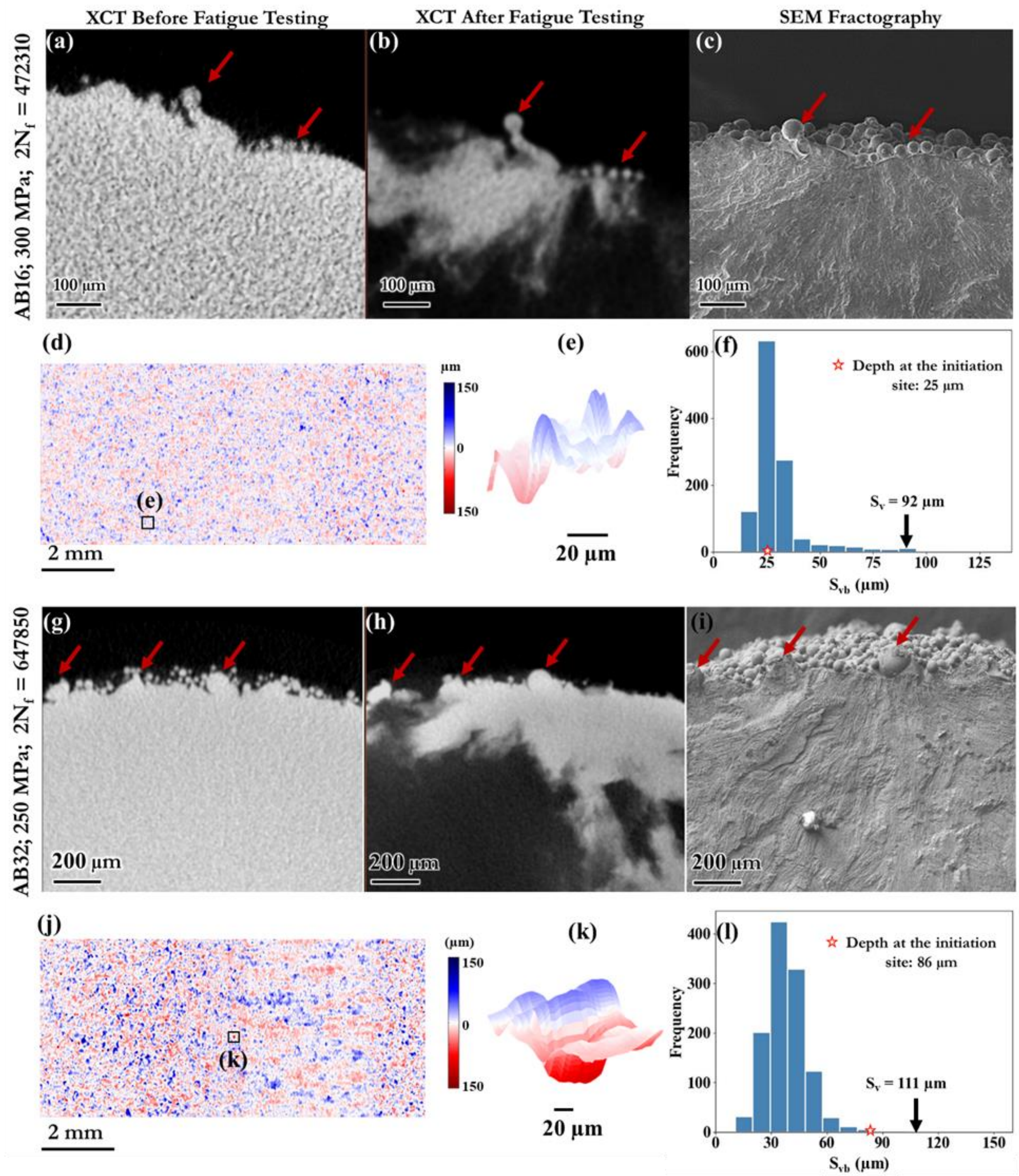

Figure 9 Analysis of surface micro-notch responsible for fatigue crack initiation: (a) & (g) XCT slice view of the crack initiation site before fatigue testing and (b) & (h) after fatigue testing, (c) & (i) crack initiation site from SEM fractography, (e) & (k) magnified views of crack initiating valleys, and (f) & (l) histograms of the entire surface. The red star on the histogram indicates the surface valley depth at the crack initiating location, while black arrow points at the S_v on the histogram.

2.5 Critical Surface Features

In essence, AM parts with rough surfaces can be considered analogous to notched geometries, where the most detrimental notches cause the most severe stress concentrations. Following Neuber's approach, the severity of notches can be effectively quantified by the fatigue stress concentration factor (or notch factor), K_f [66,68]:

$$K_f = 1 + \left[\frac{K_t - 1}{1 + \sqrt{\frac{\gamma}{\rho}}} \right], \qquad \text{Eq. (3)}$$

where K_t is the elastic stress concentration factor, ρ is the notch radius, and a_L is the material's characteristic length related to the microstructure and ductility. Treating notches as small elliptical holes in a plate and based on two dimensional, elastic stress solutions, different expressions of K_t have been proposed with different geometrical descriptors of the notches (see **Figure 10**).

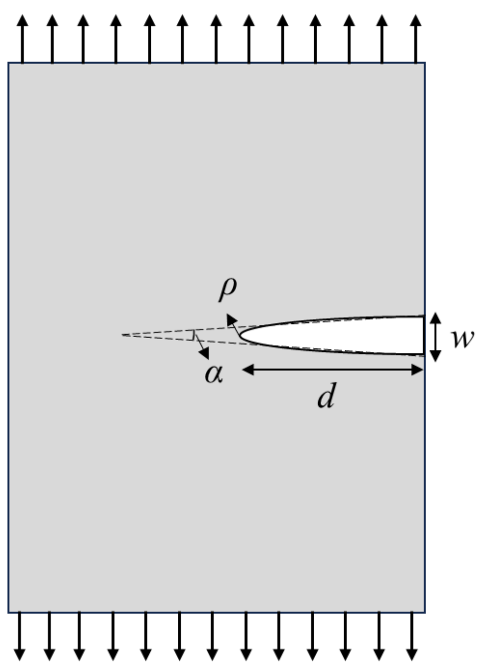

Figure 10 A schematic of semi-elliptical notch geometry.

Inglis's original two-parameter formula [57] expressed stress concentration, K_{t1}, as a function of valley depth, *d*, and width, *w*:

$$K_{t1} = 1 + \frac{2d}{0.5w}\,. \qquad \text{Eq. (4)}$$

The equation illustrates that the K_{t1} at the root of an elliptical notch increases significantly as it becomes flatter. A variation of Eq. (2) includes the notch root radius, ρ, instead of the notch width, *w* [69]:

$$K_{t2} = 1 + 2\sqrt{\frac{d}{\rho}}\,. \qquad \text{Eq. (5)}$$

Eqs. (2) and (3) were derived based on the elastic stress at the root surface of smooth notches. Nishitani and Tada evaluated the elastic stress concentration with the presence of short cracks. They calculated the stress intensity factors of cracks of varying lengths with and without the presence of the elliptical edge notches and computed the ratio between the two stress intensity factors. By taking crack length to the limit of zero, the ratio becomes K_t. An expression for the K_t that incorporates the dimensionless geometry factor as a function of notch width, *w*, and valley depth, *d*, was developed [70]. The adjusted stress concentration factor, K_{t3}, in terms of K_{t1} and the geometric factor can be expressed as:

$$K_{t3} = K_{t1}.\left[1 + 0\cdot 122\left(\frac{1}{1+\frac{0.5w}{d}}\right)^{\frac{5}{2}}\right]. \qquad \text{Eq. (6)}$$

Notice that the K_t so far assumed that the notches were semi-elliptical. In reality, the shape of micro-notches on the unmachined surfaces of AM parts may significantly deviate from this assumption. Such scenario has been illustrated in **Figure 10**, where opening angle, α, can significantly affect the stress concentration. Noda and Takase [71] stated that the effect of α was significant when $d/\rho > 1$, with K_t increasing as α decreased. This study, therefore, proposed a revised stress concentration factor, K_{t4}, in terms of d, ρ, and α as:

$$K_{t4} = \frac{K_{t1}}{\alpha^{\frac{1}{4}}}. \qquad \text{Eq. (7)}$$

Finally, to further illustrate the effectiveness and predictive capabilities of the four stress concentration factors (K_{t1}, K_{t2}, K_{t3}, and K_{t4}), a fifth factor based on S_v, referred here as K_{t5}, was introduced for comparison. K_{t5} was analogous to K_{t2}, except that the depth, d, was replaced with the S_v obtained from the entire surface topography using the N/OH method (see **Figure 7(b)** and **Table 3**), while the radius of curvature, ρ, was substituted with an effective radius of curvature, $\bar{\rho}$. The relation could be expressed as:

$$K_{t5} = 1 + 2\sqrt{\frac{S_v}{\bar{\rho}}}. \qquad \text{Eq. (8)}$$

Lee et al. [20] argued that topographical features tend to repeat across successive layers. Since the primary roughness was directly related to the layer thickness [6,72], the effective radius, $\bar{\rho}$, could be simplified to half of the layer thickness. Accordingly, $\bar{\rho}$ was set to 15 µm in K_{t5} formula in this study.

Next, using the notch parameters, w, d, ρ, and α, computed according to the algorithm in **Section 2.3**, K_t was calculated for each surface notch of all specimens according to the five aforementioned expressions (namely K_{t1}, K_{t2}, K_{t3}, K_{t4}, and K_{t5}) and the corresponding K_f (Eq. (1)) was used to assess the notch severity. Note that for evaluation of K_{f5} using Eq. (1), the ρ was substituted with $\bar{\rho}$. For Eq. 2, γ = 2.5 µm was chosen as the length scale of the microstructural unit (i.e., α lath thickness), which is typically reported to be in the range of 1 – 5 μm for stress-relieved L-PBF Ti-6Al-4V) [73]. This process is illustrated in **Figure 11** and **Figure 12**, using the AB1 specimen tested at 300 MPa as an example. **Figure 11(a)-(c)** illustrate the XCT slices before and after testing, as well as the corresponding fracture site from SEM fractography. In the first step, the K_f variants were computed for each line profile (see **Figure 11(f)-(i)**, where respective values of K_f for each expression are shown in scatter plots along with the height profiles themselves). It is anticipated that the critical valleys with higher fatigue stress concentration factor values (reddish points) are likely to be fatigue critical. Indeed, **Figure 11** shows that all four expressions of K_t have resulted in K_f values that correctly identified the fatigue critical notch for this specimen, as indicated by the red arrows. This trend was consistently observed in all specimens where crack initiation location was identified via XCT and SEM (more details provided in latter paragraphs). Note that K_{f5} was not included in this analysis, as it represents a single value derived from the overall surface texture information and does not reflect the criticality of individual notches.

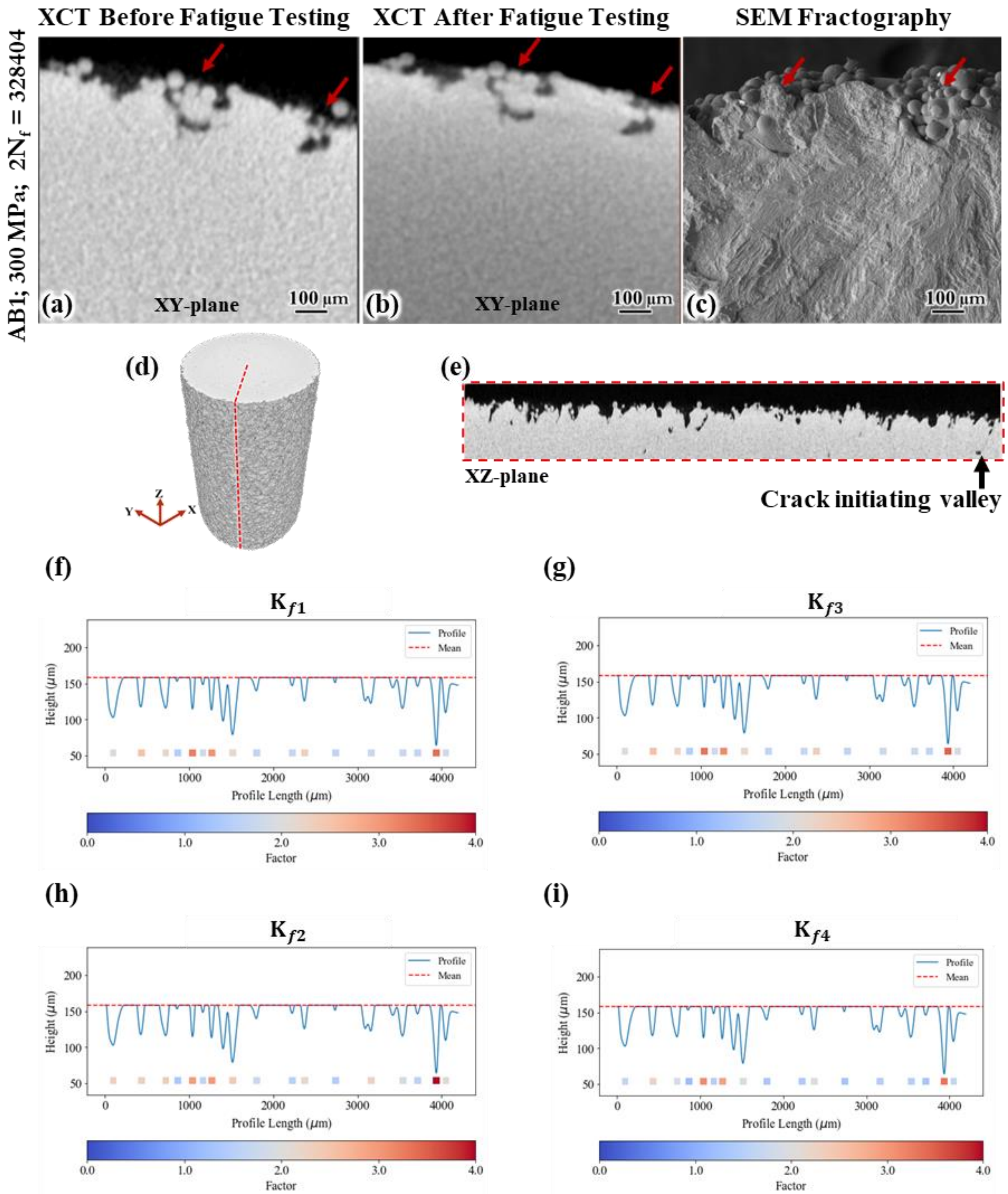

Figure 11 (a)-(b) XCT slice views of the crack initiation site before and after specimen failure. (c) SEM fractograph. (d) Radial reslicing of the fracture surface to obtain the longitudinal view (XZ plane) of the crack initiation site. (f)-(i) Scatter plots showing the K_f of each micro-notch along the longitudinal direction (or profile length) of the slice in (e), calculated using various K_f expressions.

In the second step, the procedure outlined in **Figure 11** is repeated for each profile across the entire surface topography of the specimen. The K_f resulting from each variant of K_t was computed and presented in a scatter plot, with colors corresponding to the K_f values (see **Figure 12**). Again, red datapoints indicate regions with the highest stress concentrations, which are potential crack initiation sites or represent critical surface features. To confirm this, the micro-notches with the top 1% K_f values for each expression were extracted and plotted separately. As shown in **Figure 12**, all the considered K_t expressions yielded K_f that correctly captured the fatigue crack initiation site (indicated by red circles) within top 1% notches with the highest values. The methodology was further validated for four additional specimens (AB16, AB27, AB31, and AB32), for which the results are presented in **Section S3** of Supplemental Material. Identifying the locations of the crack initiation features in the specimen via both XCT and SEM was a challenging and time-consuming process due to the complex topographical features and their subtle nuances. As a result, the validation of the methodology was limited to a small number of specimens. Nonetheless, the approach was applied to all tested specimens for fatigue modelling purposes.

In some cases, however, the surface notch with the highest K_f did not always correspond to the crack initiation site although the crack initiating datapoint was always within the top 1% of the K_f values (see **Figure S4** in Suppl. Mat.). This discrepancy was mainly due to the fact that the scan resolution was not always sufficient to capture the sharpest valleys and their radius of curvatures that led to crack initiation. Nevertheless, multiple crack initiation sites were often observed not only within the examined fracture surfaces (see **Figure 6**), but also elsewhere on the specimen gages, and the notches calculated with highest K_f values always corresponded to the initiation of a minor crack. Keeping these points in view, the surface valleys with the highest values of the K_f were still used for fatigue modelling purposes, despite the occasional discrepancies observed.

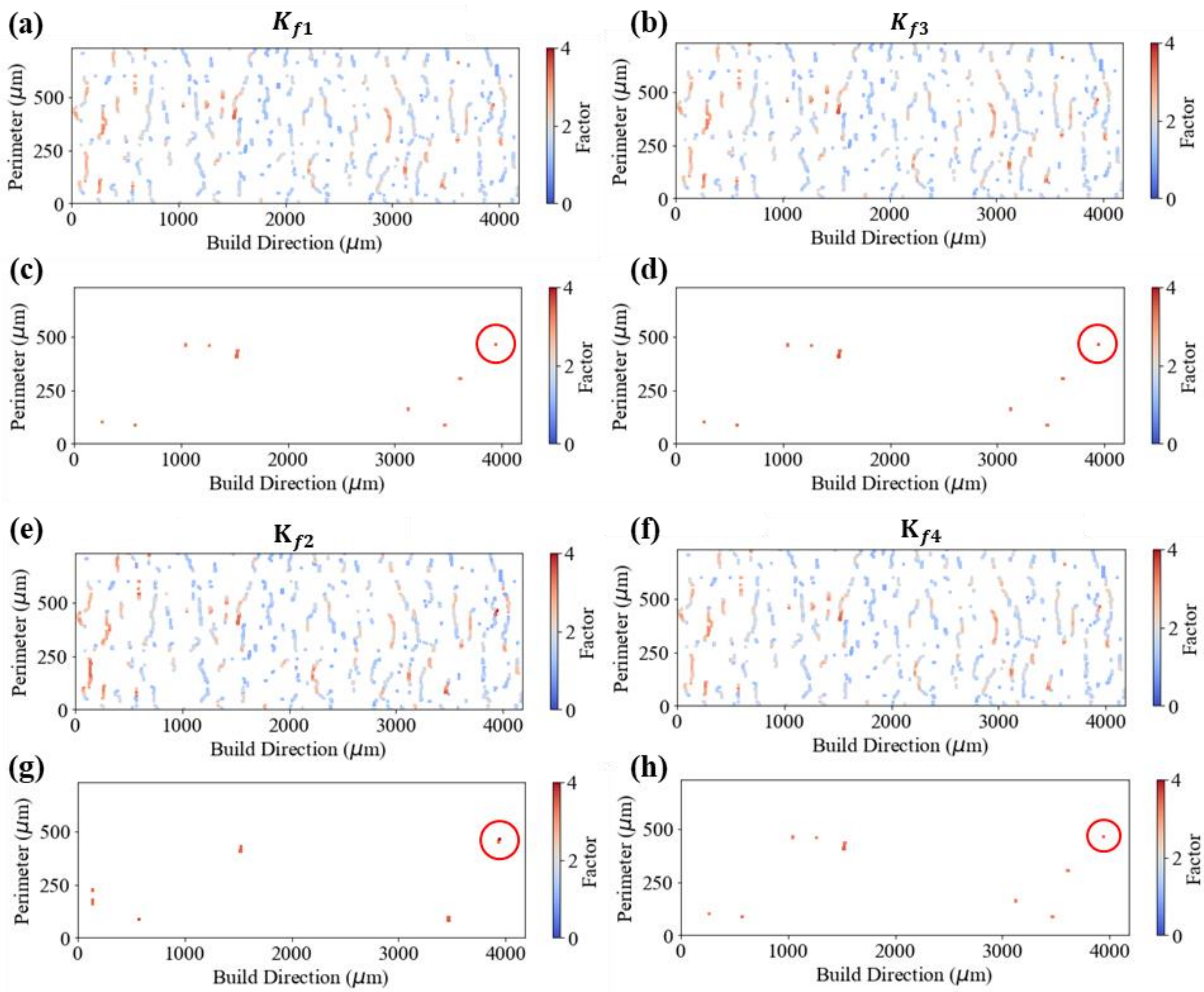

Figure 12 Evaluation of severity of surface features using various K_f expressions shown in (a), (b), (e), and (f). The top 1% K_f values for each expression are highlighted in (c), (d), (g), and (h). Red circles on each scatter plot indicate the locations of crack initiation.

2.6 Fatigue Modeling Based on Surface Texture

A tri-slope, fatigue notch factor approach [66] was used for fatigue life estimation of all the tested specimens. This method assumes that the stress-life data, when presented on a log-log plot, is piece-wise linear and can be divided into three regions: (1) from 1 to 2×10^3 reversals, (2) between 2×10^3 and either 2×10^6 or 2×10^8 reversals, and (3) beyond 2×10^6 or 2×10^8 reversals. In Region 1, the effect of surface notches is not significant due to profuse plastic deformation in the specimen, the resulting notch blunting effect, and the dominance of fatigue crack growth in fatigue life [66]. Indeed, a clear separation between unmachined and machined & polished specimens was often observed above 2×10^3 reversals for L-PBF Ti-6Al-4V [41,54]. The influence of surface notches is more pronounced in the Regions 2 and 3, corresponding to the high cycle and very high cycle fatigue regimes. Consequently, the fatigue notch factor approach adopted in this study used stress-life data of machined & polished specimens as a reference and, to predict the stress-life behavior of a notched specimens (in the context of this study, they are for the unmachined specimens, σ_e^{um}), applied the fatigue notch factor, K_f, to the endurance limit of the reference data, σ_e, i.e., $\sigma_e^{um}=\sigma_e/K_f$. The experimental stress-life data at R = 0.1 which exhibits the endurance limit of 600 MPa at 10^7 reversals for machined & polished L-PBF Ti-6Al-4V is shown in **Figure S5** of the Suppl. Mat. The stress-life behavior of unmachined specimens in the Region 2 was the intermediate of their Regions 1 and 3 and was constructed by interpolation between the fatigue strengths at 2×10^3 reversals ($\sigma_{f,2\times10^3}$) and σ_e^{um}. The fatigue life of an unmachined specimen in the Region 2 at a given stress could then be estimated if the K_f was known. Note that $\sigma_{f,2\times10^3}$ = 1010 MPa was obtained using an ultimate tensile strength of L-PBF Ti-6Al-4V [11] and corresponding fatigue strength factor of f = 0.85 [74].

Excluding runouts, the analysis showed that, for K_{f1}, 91% of the predictions were within the scatter band of 2, and 100% of the data fell within the scatter band of 3 (see **Figure 13(a)**). For K_{f2}, 89% of predictions were contained within the scatter band of 2, with all predictions (100%) falling within the scatter band of 3 (see **Figure 13(b)**). In the case of K_{f3}, 86% of the predictions were within the scatter band of 2, and 92% fell within the scatter band of 3 (see **Figure 13(c)**).

Notably, for K_{f3}, the predicted fatigue lives were typically shorter than the experimentally observed fatigue lives, resulting in conservative fatigue predictions, which was desirable for design purposes. Lastly, for K_{f4}, 89% of the data were within the scatter band of 2, and 97% were within the scatter band of 3 (see **Figure 13(d)**). The high percentage of predictions lying within the scatter band of 3 across all cases of K_f highlighted the effectiveness of the proposed method in predicting the stress-life behavior of unmachined specimens. K_{f5}, on the other hand, yielded more conservative and less accurate fatigue predictions, with only 72% of predictions falling within a scatter band of 2 and 92% within a scatter band of 3 (see **Figure 13(e)**). The lower accurate fatigue lives predicted using K_{f5} is because this parameter is solely based on S_v which represents the overall surface texture, not the most critical surface notch. In contrast, other models that incorporated localized surface texture information were more accurate, as they captured the localized nature of fatigue damage. Nonetheless, conservative predictions of K_{f5} are not necessarily a drawback in designing fatigue critical parts, given that S_v is much easier to measure than identifying and characterizing the critical surface notch and its parameters.

Notably, the runout predictions in all the cases fell outside the scatter bands of factors 2 and 3, and the proposed approaches predominantly predicted failure for these specimens. While conservative predictions are often preferred in the design of fatigue-critical components to ensure safety, it is also important to balance safety margins with the costs associated with overdesigning. For example, K_{f5} resulted in more conservative predictions, which may not be an optimal approach to component design when light weighting is desired.

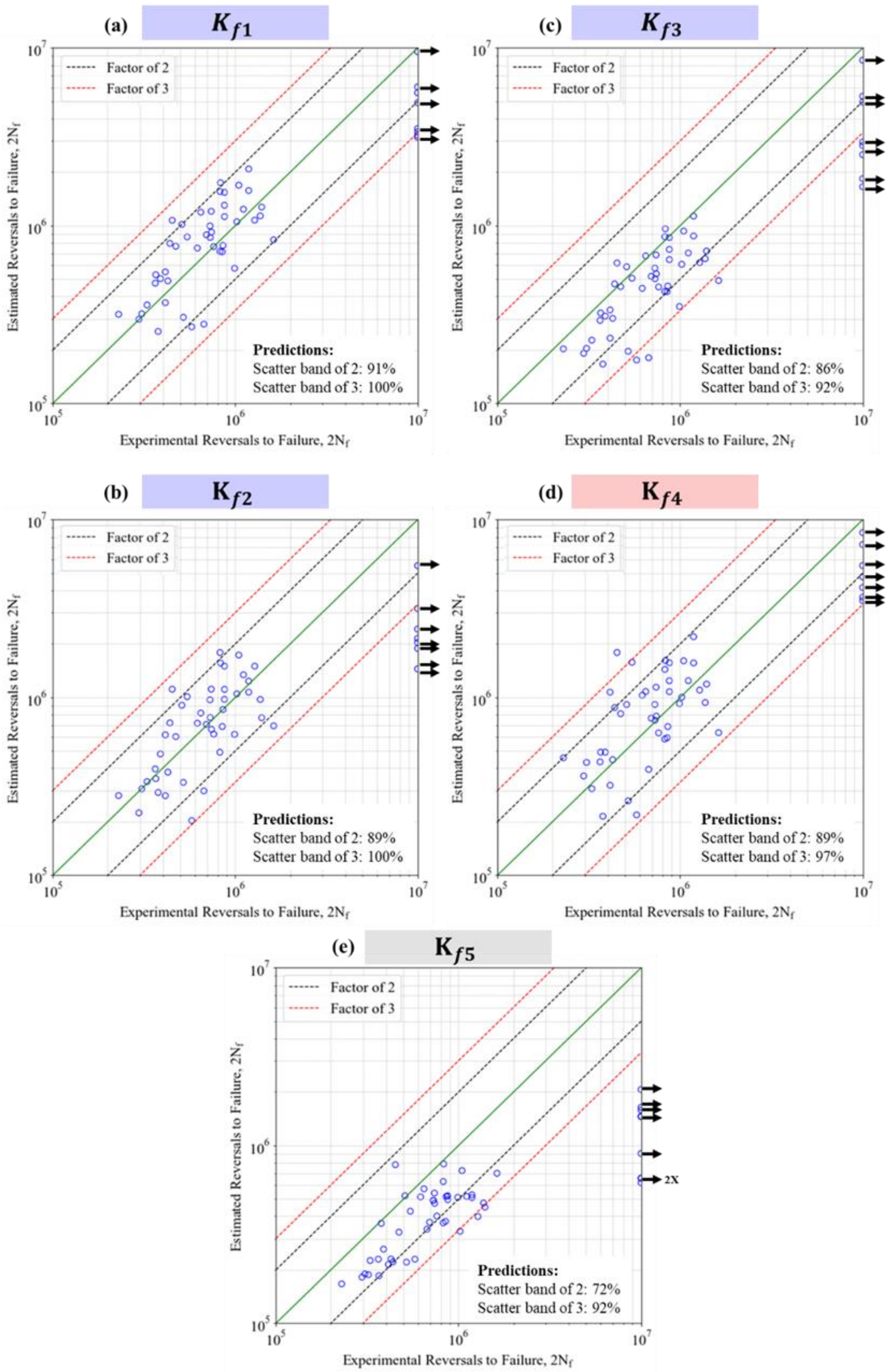

Figure 13 Estimated fatigue lives compared to experimental fatigue lives with the scatter bands of two and three. Black arrows represent runouts.

2.7 Conclusions

This study examined the critical surface features influencing the fatigue behavior of unmachined laser powder bed fused (L-PBF) Ti-6Al-4V parts. X-ray computed tomography (XCT) was used to capture the parts' surface texture, including the hidden valleys. The shapes of individual surface valleys were quantified and the elastic as well as fatigue stress concentration factors were calculated. The fatigue stress concentration was shown to be effective in identifying the critical surface micro-notch and predicting fatigue life. The following conclusions were drawn from the results:

1. The maximum valley depth, S_v, in unmachined surface captured by XCT with overhang structures showed poor correlation with the fatigue life. After removing the overhang structures, S_v showed better correlation and somewhat distinguished between runout and fractured specimens. Specifically, S_v values for runout specimens consistently remained below 100 μm, whereas those for fractured specimens were higher than 100 μm.
2. The fatigue criticality of surface micro-notches could be adequately represented by their fatigue stress concentration factors calculated from a combination of geometrical features (notch width, depth, opening angle, and radius of curvature) using classical elastic stress concentration formulae. Specifically, the experimentally observed fatigue-critical surface notch(es) for any given specimen was demonstrated to always lie within the top 1% of all notches in the said specimen in terms of the calculated fatigue stress concentration values.
3. A fatigue notch factor based modelling framework, utilizing the calculated fatigue stress concentration factors, was shown to estimate the fatigue lives of unmachined

L-PBF Ti-6Al-4V specimens with reasonable accuracy. All predictions fell within a scatter band of 3 with respect to the experimentally measured fatigue lives. In comparison, S_v based fatigue notch factor model showed that 92% of predictions fell within the scatter band of 3.

Further studies are necessary to validate the robustness of these findings across various materials, stress ratios, environmental conditions as well as manufacturing conditions. The approach is expected to be also applicable to partially treated surfaces, such as those subjected to polishing or shallow machining, as long as the surface treatment does not significantly alter the material's microstructure or introduce substantial residual stresses. Expanding this framework to more diverse material systems and surface conditions can potentially help with predicting fatigue behavior and designing more fatigue-resistant components for a wide range of applications. In addition, future studies can include advanced statistical analyses (e.g., Bayesian inference, regression analysis) or machine learning algorithms (e.g., support vector machines, neural networks) to better capture the complex interactions of notch parameters.

3 Surface integrity of additively manufactured Ti-6Al-4V: Influence of process variables on tensile and fatigue behaviors

3.1 Introduction

Additive manufacturing (AM), specifically laser powder bed fusion (L-PBF), enables the on-demand fabrication of customized and intricate geometries, which would otherwise be challenging to achieve using conventional manufacturing techniques [6,32,36]. A key advantage of L-PBF lies in its design flexibility: new designs can be conceived and realized prioritizing functionality, with minimal concern for tooling and fixturing constraints [75]. Moreover, by the consolidation of multiple components into one monolithic part, L-PBF can potentially reduce overall production and assembly costs [13,76]. As a result, L-PBF appeals to aerospace and automotive industries [77,78].

Laser powder bed fused (L-PBF) parts in their as-fabricated state typically exhibit pronounced surface roughness [33,53] and often contain volumetric defects such as lack-of-fusions (LoFs), keyholes (KHs), and gas entrapped pores [8,41]. As a result, their mechanical performance is often inferior compared to wrought counterparts [1]. While post-processing steps including hot isostatic pressing (HIP) and machining could be adopted to remove these defects, they have been reported to be not always effective [33,53]. For example, machining may not be feasible on parts with complex geometries, and HIP has been shown to be ineffective at closing large surface and near-surface defects [10,35,79]. Moreover, these post-processing steps increase the overall production cost and lead time, which undermine key advantages offered by L-PBF [2,13]. In such scenarios, deploying L-PBF parts without heavy post-processing treatments in the service could be a practical alternative.

The surface roughness and near surface volumetric defects in L-PBF parts exhibit great variability since they depend on thermal history, which can change within a part and between parts across different locations of the same build [15,80]. Specifically, thermal history of a material point is partially governed by the thermal dissipation pathways available to it during fabrication; and accordingly, even with the manufacturer's recommended process settings, factors such as the local size, overall geometry, and build orientation can make a part's thermal history highly heterogeneous. In addition, the process parameters optimized for witness coupons may not necessarily be scalable to larger and geometrically more complex parts or components. For instance, Shrestha et al. [81] reported L-PBF 17-4 PH SS fatigue specimens excised from the large block showed longer fatigue lives compared to net-shaped specimens, which was ascribed to higher cooling rates in net shaped specimens that promoted increased porosity [25]. Similarly, Klingaa et al. [82] showed small cooling channels of L-PBF AlSi10Mg specimens possessed higher surface roughness compared to larger ones due to the higher cooling rates. Nevertheless, the common practices typically employ recommended process settings uniformly across the entire part, without accounting for variations in local thermal histories and resulting effects on the surface texture. This can be problematic for complex geometries, which often have cross-sections with varying thicknesses and thus different thermal history, affecting surface texture and mechanical performance [83,84].

As L-PBF enters into mainstream manufacturing, the operational issues such as low build rate and productivity quickly become the bottleneck for its widespread adoption in high-volume production. Instead of opting for prohibitively expensive hardware changes (e.g., use of multi-laser or rotary powder beds), one practical solution is to accelerate the build rates in the non-critical regions by adjusting the process parameters, e.g., increasing the layer thickness, laser speed, and hatch spacing, or by either reducing or avoiding contour passes altogether [26,85,86]. For instance, although the application of more than one contour pass, which is often recommended by L-PBF machine manufacturers, may improve surface quality, it did not always offer the best trade-off and was shown to increase tensile residual stresses and prolong build times [87,88]. In some cases, using a single-contour pass may offer an optimal balance between surface quality and build time. Buchenau et al. [89] examining L-PBF AlSi7Mg0.6 and Mu et al. [90] studying L-PBF 316L stainless steel specimens reported that specimens printed with just one contour pass achieved arithmetical mean height, S_a, values somewhat similar to those produced with multiple contour passes. While these studies have shown promise for improving build rates without a significant loss in surface quality, the resulting changes in the tensile and fatigue behaviors remain to be explored.

This work investigates the influence of process variations, specifically the effects of infill and contour strategies, on the surface texture and, in turn, tensile and fatigue behaviors. In addition to mimicking the aforementioned process adjustments during mass production, the alterations in process parameters also aim to induce the thermal history changes to emulate the ones inadvertently encountered within a part and/or among parts. The process variables including laser power, scan speed, and contour strategies were systematically varied to produce a wide range of surface and near-surface conditions. X-ray computed tomography (XCT) was used to analyze the surface textures of these specimens, and tensile and fatigue testing was performed to evaluate mechanical behaviors.

3.2 Experimental Procedures

3.2.1 Fabrication and processing conditions

All the specimens, in their net shapes, were fabricated vertically (i.e., perpendicular to the build plate) using an EOS M290 L-PBF machine with one-time used plasma atomized Ti-6Al-4V powder supplied by AP&C, a Colibrium Additive company. Before fabrication, the powder was sieved using a 63 µm mesh to remove large particles and agglomerates from the powder. The particle size distribution of the powder ranged from 15 to 65 µm in the virgin state, with a mean value of 25 µm. The nominal chemical composition of the feedstock powder is presented in **Table 5**. The building process was kept under an argon atmosphere with a positive differential pressure of 0.6 mbar and a build plate temperature of 40°C. Both the tensile and the fatigue specimens were designed according to ASTM E08 [91] and ASTM E466 [58], respectively. The dimensions of both tensile and fatigue geometries are shown in **Figure 14(a) and (b)**, respectively. Note that the gage length of fatigue specimen was adjusted to 5 mm to allow the XCT scan of entire gage section.

Using specimens fabricated with EOS-recommended process parameters (designated as Default hereon) as a baseline, seven additional sets were manufactured, which involved different combinations of infill (i.e., laser power and laser speed) and contour settings (i.e., no-contour, single-contour, beam-offset). These process variations were designed to generate a wide range of surface and near-surface conditions. Compared to Default, higher energy input (i.e., achieved via reducing laser speed and increasing power) was expected to generate more KHs in specimens, while lower energy input (i.e., via reducing power and increasing laser speed) was anticipated to induce more LoFs. Three distinct infill conditions (LoF, KH, and Default) were then combined with either the default-contour strategy (i.e., 2 contour passes) or no-contour, yielding a total of six unique fabrication conditions. Moreover, two additional conditions were explored while keeping the EOS-recommended infill parameters: one with modified beam-offset, where the distance between the contour and infill scans was doubled from the default 20 µm to 40 µm, and another with reducing the number of contours to a single-contour pass. The schematic representations of different process conditions are illustrated in **Figure 15**. A total of 124 fatigue specimens were fabricated, including backups for each process condition. The details of different process parameters are listed in **Table 6**, where the eight process conditions have been labeled from C1 to C8. In all the specimen sets, the layer thickness and hatch spacing were kept at 30 µm and 14 µm, respectively, while the laser power and laser speed of default-contour process parameters were 150 W and 1250 mm/s, respectively. Post-fabrication, the specimens underwent stress-relieving treatment at 704 °C for 1 h in an argon-filled box furnace, followed by air cooling to room temperature at an approximate rate of 2 °C/min. Then, specimens were removed from the substrate using a bandsaw.

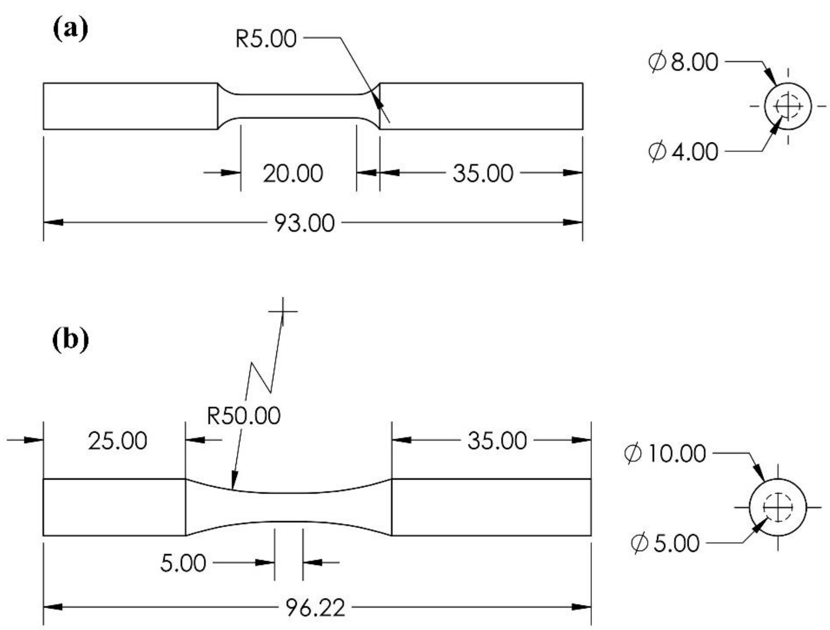

Figure 14 Geometry and dimensions (in mm) of the fabricated specimens; (a) tensile specimen and (b) fatigue specimen.

Table 5 The chemical composition of the AP&C plasma atomized powder reported by the manufacturer (wt.%).

O	Al	V	Fe	C	N	H	Y	Ti
0.2	6.75	4.5	0.3	0.08	0.05	0.02	0.01	Bal.

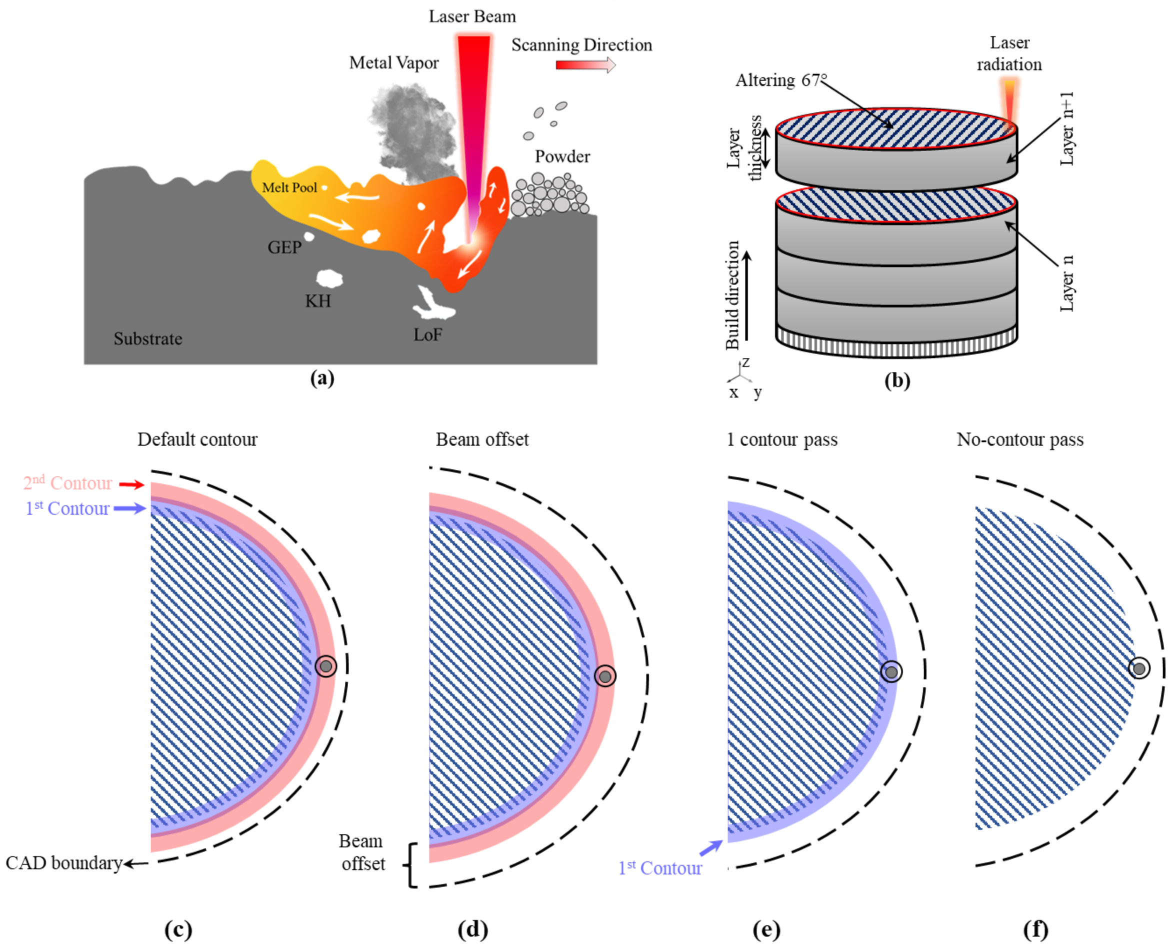

Figure 15 Schematics illustrating: (a) the laser melting process, (b) the build strategy exhibiting alternating hatch lines and contour regions; as well as different contouring approaches of (d) default-contour, (e) increased beam-offset, (f) single-contour, and (g) no-contour.

Table 6 Process parameters and settings used for fabricating the specimens.

Conditions	C1	C2	C3	C4	C5	C6	C7	C8
Contour strategy	No-contour	No-contour	No-contour	Default-contour	Default-contour	Default-contour	Single-contour	Offset
Infill setting	Default	KH	LoF	Default	KH	LoF	Default	Default
Laser power (W)	280	365	250	280	365	250	280	280
Laser speed (mm/s)	1200	960	1200	1200	960	1200	1200	1200

3.2.2 Surface texture and volumetric defect analysis

Before mechanical testing, one-third of the specimens from each set were scanned in a Zeiss Xradia 620 XCT system. The scans utilized an accelerating voltage of 140 V, a power of 21 W, a 0.4X objective lens, and an exposure time of 2 seconds. For each scan, a pixel size of 5.3 µm was employed, which covered a total scanned volume of 108 mm^3. The reconstruction was performed using the Zeiss proprietary software. Surface texture analysis was performed following the methodology outlined in the authors' previous work [8]. The procedure began with reslicing the reconstructed image stack along the longitudinal plane, aligned with the specimen's long axis (see **Figure 16(a)**). This generated a series of longitudinal slices, each taken at an angle of 0.13° around the specimen's circumference. Subsequent steps were performed using a Python script, which included binarization of greyscale image and then construction of line profiles by identifying and then tracing the transition between black and white pixels. All surface texture data and analyses presented in this work were based on the no overhang (N/OH) approach described in the authors' previous work [8]. Overall, six specimens from each condition were scanned via XCT and analyzed using N/OH approach.

In addition to examining the surface texture of the entire gage section, S_a and S_v values from different sides of each specimen's gage were also analyzed. For this purpose, the specimen's gage section was subdivided into four regions, namely North, East, South, and West (see the schematic illustration in **Figure 16(b)**). These designations were assigned based on the specimen's orientation with respect to the argon gas flow and powder recoating direction during fabrication, where the side facing argon flow during fabrication was named as North, while the side that first encountered the recoater blade was labeled as East. During XCT scanning, the specimen's orientation was aligned with reference to the engraved label located in the grip section on the north-facing side (see **Figure 16(b)**). Using MATLAB, the longitudinally resliced images, totaling 2719 slices, were divided into four nearly equal angular regions (692 slices per region). Each region was then separately analyzed, and the roughness parameters, including S_a and S_v, were calculated. For each condition, the calculation of S_a and S_v was repeated for each of the four sides of six specimens.

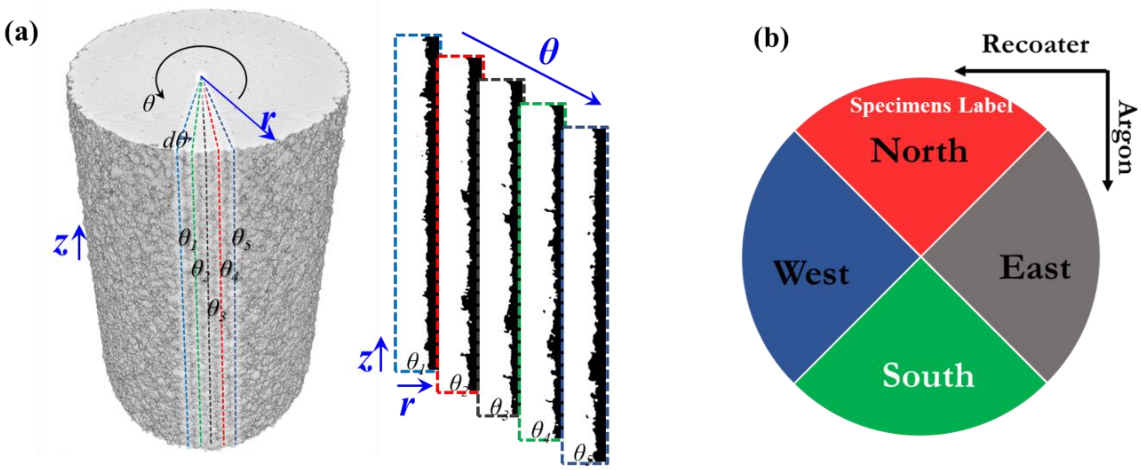

Figure 16 (a) Schematics of the longitudinal reslicing and (b) orientation of the specimen's gage section sides (North, East, South, and West) relative to the recoating and argon gas flow directions.

3.2.3 Mechanical testing and fractography

Tensile tests were conducted using an MTS Landmark load frame following the ASTM E08 standard [39]. Strain at the gage section was measured using an MTS mechanical extensometer. Initially, the tests were performed in strain-controlled mode up to a strain value of 0.035 mm/mm, after which the test was switched to displacement-controlled mode until fracture to prevent damage to the extensometer. For each process condition, three specimens were tested, and the average and standard deviation values were reported. In addition, force-controlled fatigue tests were conducted at a stress ratio, R_σ, of 0.1 using sinusoidal loading on an MTS Bionix Tabletop load frame in accordance with ASTM E466 standards [40]. The tests continued until the specimen either fractured or persisted for 10^7 reversals, at which point the specimens were designated as runouts.

Before conducting fractography on the representative tensile and fatigue specimens, the fracture surfaces were first cut using a precision cutter, followed by sonication in distilled water and isopropanol, and then rinsing with acetone to remove any remaining moisture and dirt. Fracture surfaces were then examined using a Zeiss Crossbeam 550 scanning electron microscope (SEM) to evaluate the tensile fracture mechanisms and to identify fatigue crack initiation sites. In addition to fractography, the angular locations of crack initiation with respect to North from all the fatigue-fractured specimens were tracked and their respective orientations with respect to the recoating and gas flow directions were measured. Then, the Gaussian kernel density estimation (KDE) was applied to the measured datapoints using Python's SciPy package [92].

3.3 Results and Discussion

3.3.1 Characterization of surface and near-surface defects

The 3D visualizations of defects in representative specimens with different process conditions are shown in **Figure 17**. The largest defect observed in the scanned volume is also shown beside each corresponding condition. As seen, the morphology of the largest defects varied from irregular (see conditions C1, C2, C3, and C7) to a more spherical shape (see conditions C4 and C8). In terms of the influence of contour settings, the no-contour specimens, such as C1, C2, and C3 exhibited notably more defects near-surface compared to their counterparts with default-contour passes including C4, C5, and C6, as seen in **Figure 18** (i.e., compare C1 vs. C4, C2 vs. C5, and C3 vs. C6). Driven by the differences in the near-surface defects, the relative densities calculated for the no-contour sets were lower (see **Table 7**). Moreover, both the maximum equivalent diameter of defects as well as the 90th percentile defect sizes were larger in the no-contour sets. In the absence of contour passes, a higher density of near-surface defects could be ascribed to the gaps between either partially melted powder particles or the terminations of adjacent laser scan tracks. These defects may be sub-surface or surface-connected but can nevertheless appear in the XCT scans, limited by their resolution, as near-surface defects (see the XCT slices for C1, C2, C3, and C5 in **Figure 19**).

With one contour pass (i.e., C7), the near-surface defect density significantly reduced, yet it was still greater than that in Default condition (i.e.,C4). In addition, increasing beam-offset (i.e., C8) did not appear to significantly increase the defect density compared to the Default. As for the influence of infill parameters, the KH condition (i.e., C5) showed a significantly higher population of interior defects than C4 and C6 specimens; accordingly, the relative density was slightly decreased (see **Table 7**).

Irrespective of the process condition, volumetric defects, with morphologies ranging from irregular to nearly spherical, were always observed near the perimeter of specimens. Notably, the population of the defects in C2 and C5, particularly at the edge of specimens, appeared to be greater than other conditions. This could be attributed to increased infill energy densities combined with laser slowdown at the periphery of the specimen, both of which contributed to keyhole instabilities and pore formation [93–95].

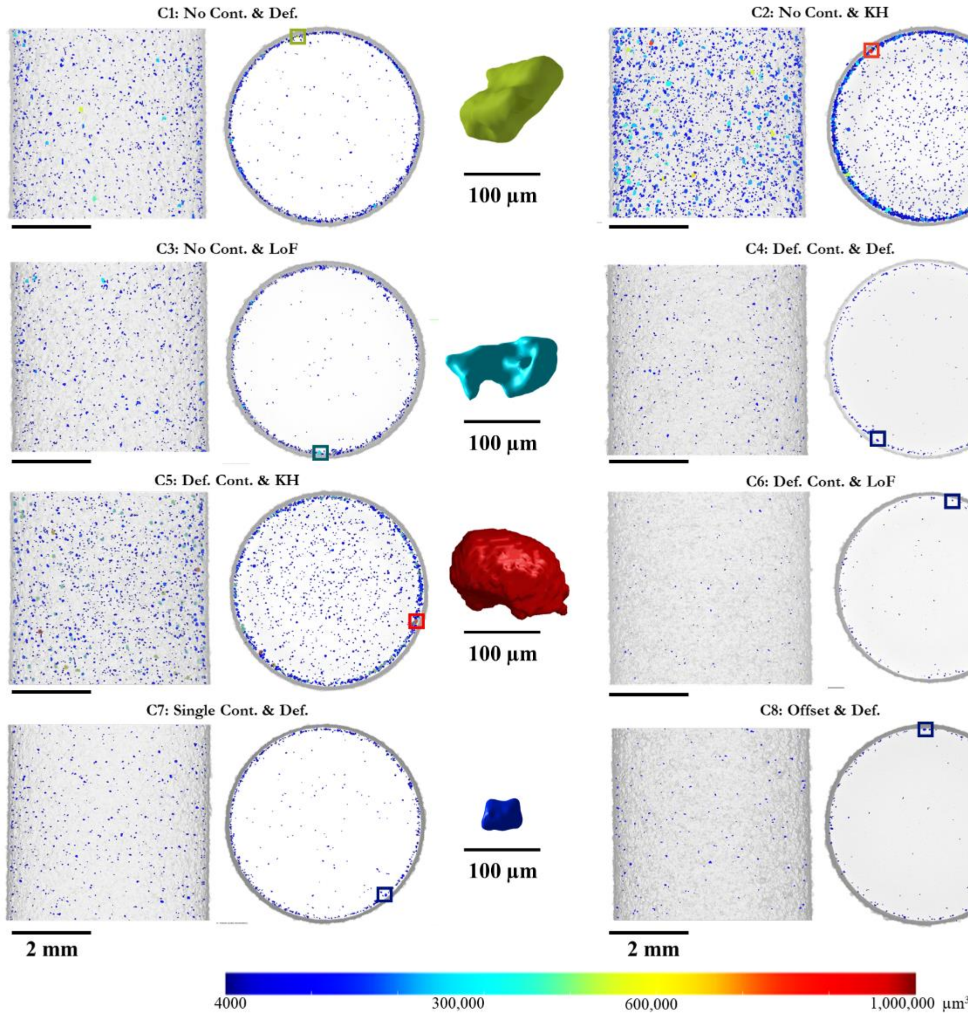

Figure 17 3D visualization of volumetric defects obtained from the XCT at the gage section of fatigue specimens. The largest defect identified for each condition is shown alongside the corresponding top view.

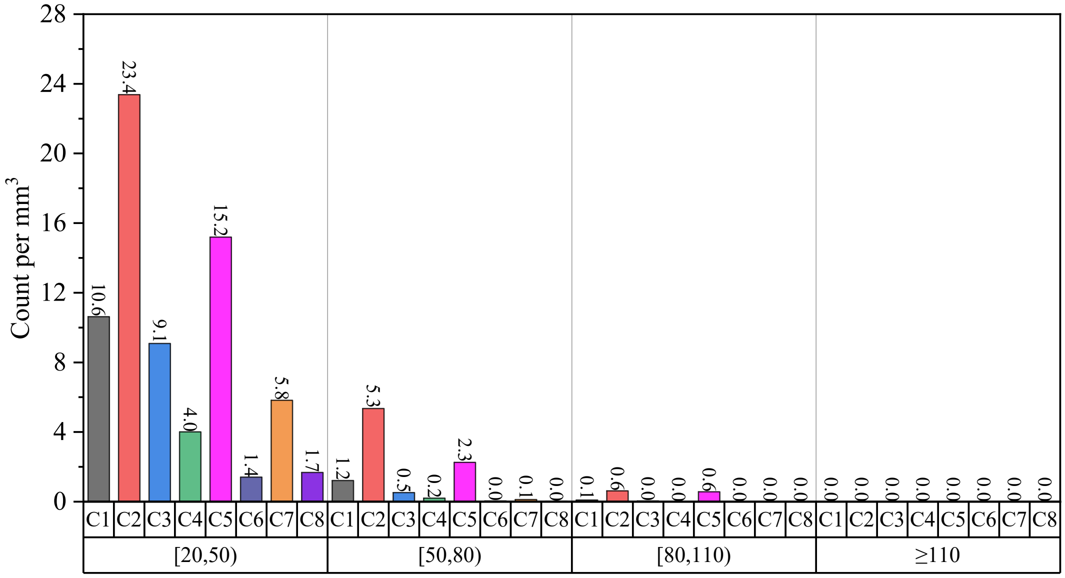

Figure 18 The size distribution of volumetric defects for various process conditions.

Table 7 The quantified information of defect size distribution for each process condition.

Conditions	C1	C2	C3	C4	C5	C6	C7	C8
	No Cont. & Def.	No Cont. & KH	No Cont. & LoF	No Cont. & Def.	Def. Cont. & KH	Def. Cont. & LoF	Sin. Cont. & Def.	Offset & Def.
Relative Density	99.9701	99.8861	99.9811	99.9930	99.9355	99.9982	99.9913	99.9999
90^{th} Percentile (µm)	52	62	46	44	59	40	41	41
Maximum Equiv. Diameter (µm)	104	117	87	70	122	56	69	59
# Defects	1117	2735	907	394	1697	136	566	162

The influence of process conditions on the surface and near-surface conditions was further analyzed via the grayscale XCT slices and corresponding surface line profiles (see **Figure 19**). In the no-contour conditions, i.e., C1, C2, and C3, the specimens exhibited very rough surface texture characterized by a higher arithmetic average profile roughness, R_a, and maximum profile valley depth, R_v, compared to their counterparts with default-contour, i.e., C4, C5, and C6. Moreover, in the absence of contour passes, many of the volumetric defects appeared to be exposed directly to the surface, while with contour passes (C4-C8 conditions), these defects were either closed due to subsequent remelting (such as in C4 and C7 conditions) or, in some cases, remained in the near-surface regions (C6 and C8 conditions). The N/OH approach treated these near-surface volumetric defects as valleys, as it identifies surface features from an internal perspective looking outward toward the material's free surface. Additionally, C7 and C8 conditions showed relatively similar R_a and R_v values to the Default condition (i.e., C4). Note that these observations are based on 2D slice views and may not fully capture true surface connectivity.

In terms of the effect of infill parameters, KH condition (i.e., C5) specimens exhibited the highest R_a and R_v values. This could be ascribed to the presence of higher density of near-surface volumetric defects compared to C4 and C6 conditions. These near-surface features were treated by the N/OH method as surface valleys, which increased the overall height deviations. This approach was shown to offer effective and slightly conservative fatigue estimations in the authors' prior work [8]. The LoF condition (i.e., C6), on the other hand, did not significantly introduce subsurface defects; therefore, R_a and R_v values were nearly similar to the Default condition (i.e., C4).

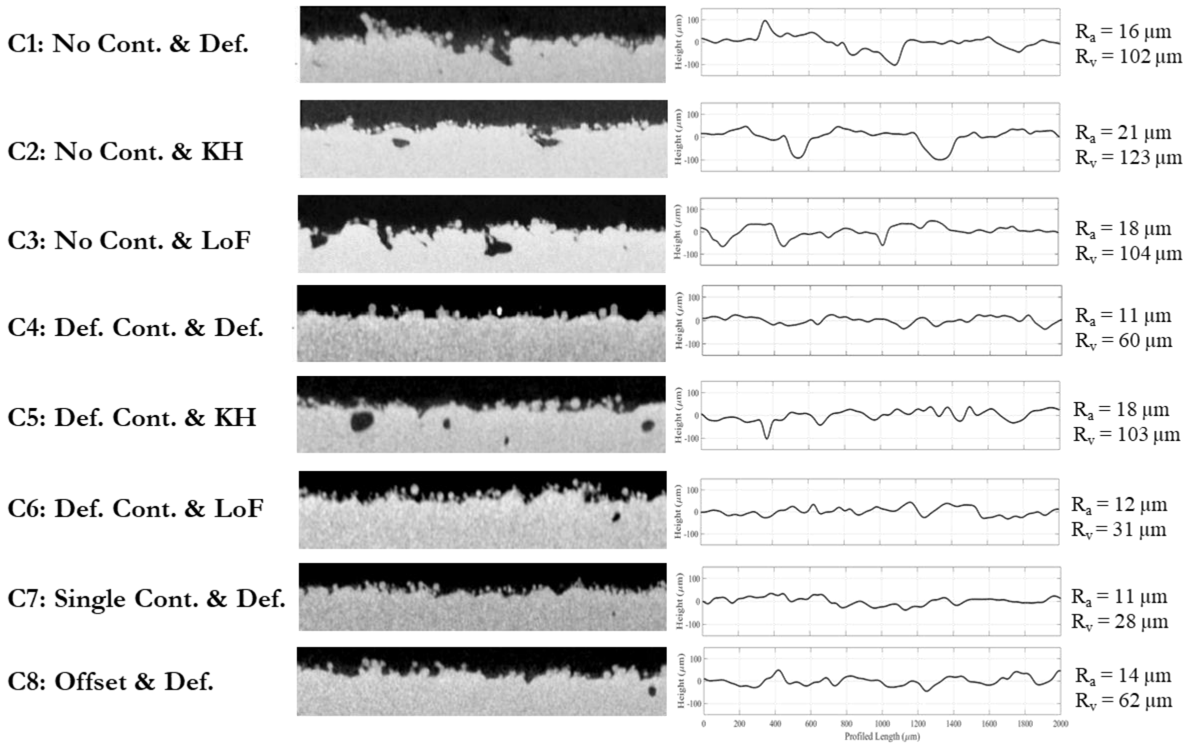

Figure 19 XCT sliced views in all process conditions and the corresponding line profiles.

A representative surface topography map for each processing condition, over a 3 mm × 3 mm area, and the corresponding areal roughness parameters including areal arithmetic mean height, S_a, and areal maximum valley depth, S_v, obtained from the XCT are exhibited in **Figure 20**. Note that the red and blue colors in the areal maps (see **Figure 20(a)**) indicate the valleys and peaks, respectively. Each S_a and S_v datapoint shown in the box-and-whisker plots (six in total for each condition) corresponds to a measurement taken from all sides of an individual specimen. Similar to the profile roughness trends, specimens in the no-contour parameters (i.e., C1, C2, and C3 conditions) also showed significantly higher S_a and S_v values compared to their counterparts in default-contour (i.e., C4, C5, and C6) conditions. In contrast, the conditions C7 and C8 exhibited slightly higher roughness values compared to C4 specimens. As for the effect of infill parameters, C5 showed a higher S_a and S_v values and a greater variation in surface roughness values than C4 and C6 conditions (see **Figure 20(b) and (c)**).

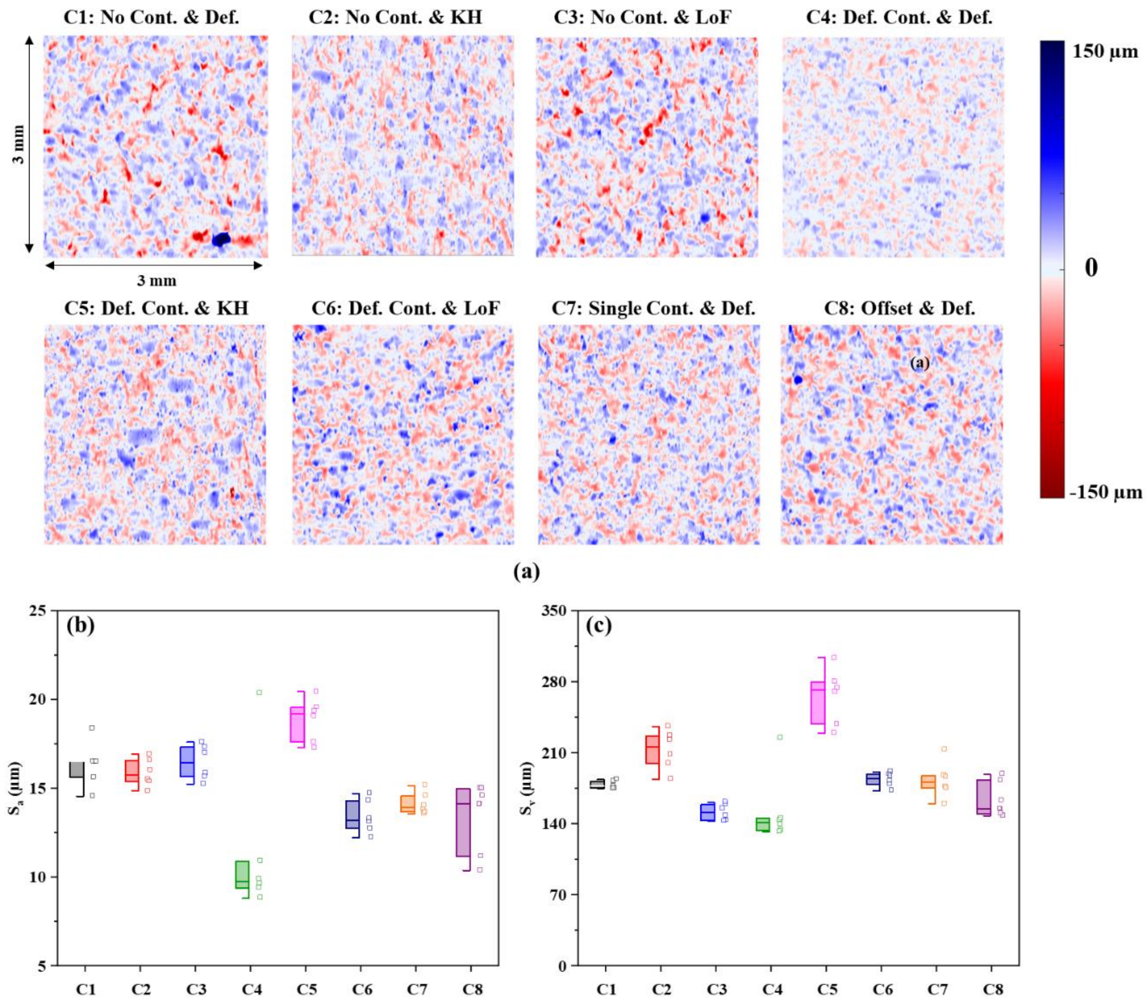

Figure 20 Surface texture analysis in eight different process conditions: (a) representative surface topography maps and areal surface roughness parameters in terms of (b) S_a and (c) S_v.

3.3.2 Directionality in surface roughness

In addition to evaluating the surface roughness parameters across the entire scanned surface, S_a and S_v values were also evaluated from four specific sides of the gage section (i.e., North, East, South, and West) with respect to the recoating and gas flow directions. As an example, the extracted areal maps and the corresponding S_a and S_v values for each side in a representative specimen from C4 condition are exhibited in **Figure 21(a)**. Next, this procedure was repeated for all the sides of each specimen across eight process conditions, and the results were plotted in the box-and-whisker plots (see **Figure 21(b) and (c)**). Each datapoint in these two panels corresponds to S_a and S_v values measured from a specific side (West, North, East, and South) of one specimen.

As seen, the South side predominantly exhibited higher S_a and S_v values across different process conditions. This trend was more noticeable in the presence of contours, specifically in conditions such as C4, C5, C6, C7, and C8. To explain this directionality and some inter-specimen variations in roughness, the orientations of specimens with respect to the directions of recoating and gas flow were examined with attention to their spatial locations on the build plate during fabrication.

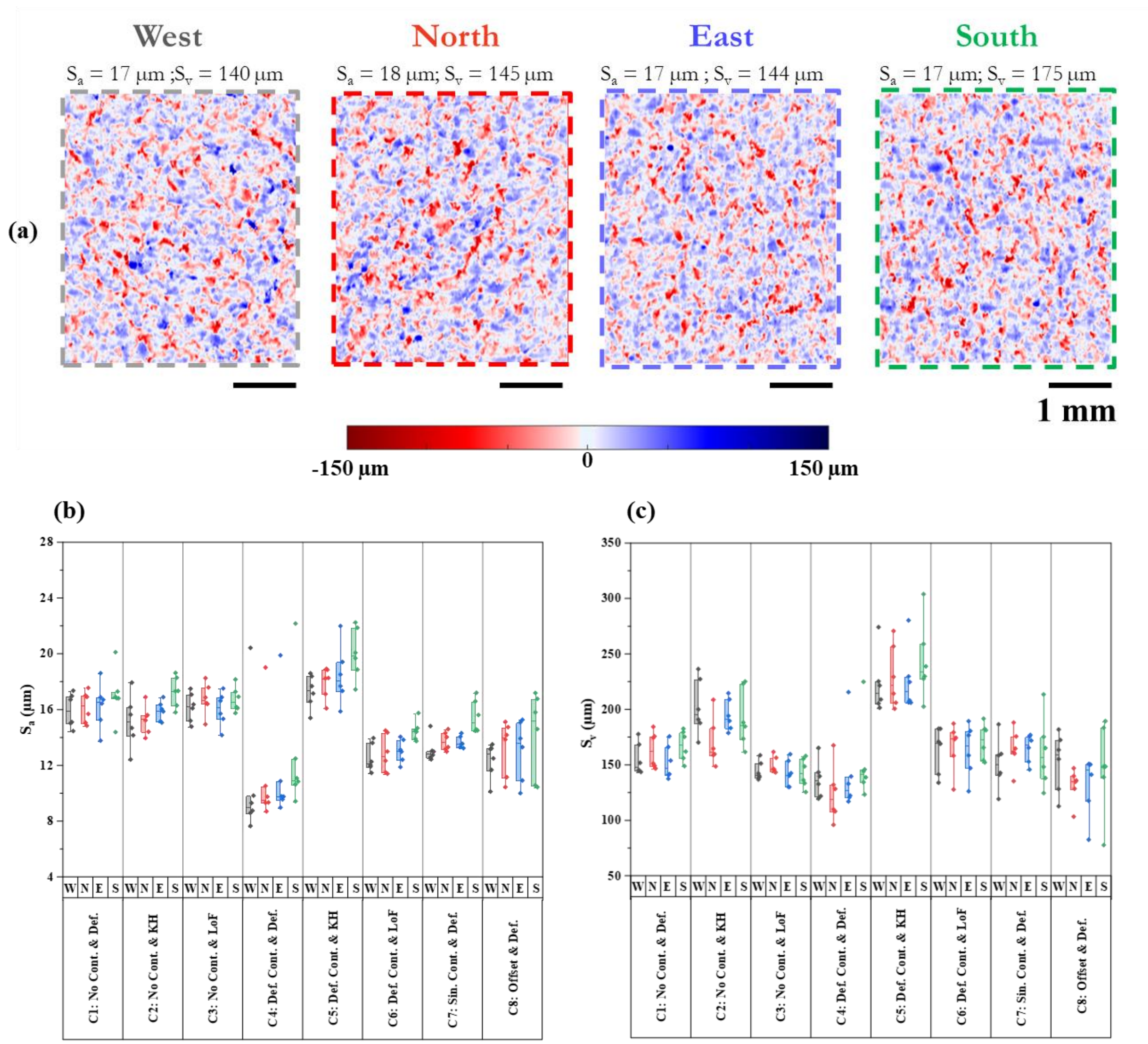

Figure 21 Surface texture analysis from four sides of specimens: (a) areal height map illustrating how the specimens' side were subdivided into four regions; evaluated surface topography parameters from the extracted regions: (b) S_a and (c) S_v across all process conditions.

As an example, the spatial locations of specimens in C4 and C5 conditions on the build plate as well as the corresponding S_v values across the four sides (i.e., North, East, West, and South) are visualized in **Figure 22**. Note that the specimens' sides are colored according to the S_v value captured in the respective side, with red color indicating the higher value, while blue represents lower values. The direction of argon gas, from the back of the machine (gas-inlet) toward the front (gas-outlet) as well as the movement of the recoater arm, from left (dispenser) towards right (overflow bin), in an EOS M290 L-PBF system are also indicated.

The South faces of both C4 and C5 conditions were predominantly rougher compared to other sides except for specimen 08-5 (see **Figure 22(a) and (b)**). This directionality could be ascribed to the interaction between gas flow and spatter particle dynamics during fabrication. As argon gas flows from the inlet toward the outlet, it entrains and transports spatter particles [96–98]. While the lighter particles are easily carried away towards the gas-outlet, the heavier ones tend to settle near South face of the specimen because of gravitational effect [99]. This preferential deposition of the spatter particles led to higher roughness in the South side of the specimens. The surface appearance of the North and South faces captured using the optical microscope (see **Figure 22(c) and (e)**) supported this explanation: the North face exhibited near-absence of abnormally large particles (which tended to be spatter), while the South face showed a substantial accumulation. Moreover, XCT slices extracted from the North and South faces (see **Figure 22(d) and (f)**) further supported this observation, where several adhered spatter particles were visible on the South face of the specimen, while the North face had nearly no spatter particles attached.

Overall, the specimens located near the gas-outlet noticeably exhibited higher S_v values on nearly all sides compared to specimens located close to the gas-inlet. To explain this, two representative specimens with identical process conditions but different build locations were chosen: specimen 68-4 (near gas-inlet), and specimen 01-4 (near gas-outlet). Then, their optical images as well as XCT slices were compared in **Figure 22(g)-(j)**. In the 01-4 specimen (**Figure 22(g)-(h)**), both the optical images and XCT slices showed the presence of several spatter particles on the surface. Additionally, XCT slices showed LoF defects, features that were largely absent in specimen 68-4 located near the gas-inlet (compare **Figure 22(h) and (j)**).

The increased surface roughness in 01-4 specimen could be ascribed to the combined effect of (1) reduced gas velocities in regions near the gas-outlet of the EOS M290 system, as reported in Ref. [100], and (2) the tendency of spatter particles to follow the direction of gas flow and accumulate in regions near the gas-outlet [101]. Reduced gas velocities not only hinder efficient transport of spatter toward the outlet but also lead to insufficient removal of spatters from the laser path which can , in turn, cause increased beam attenuation and scattering [102]. These effects have been reported to yield shallower molten pools and thus rougher part surfaces, along with a higher frequency of near-surface volumetric defects, especially LoF [103,104] for specimens located close to gas-outlet.

The one observed anomaly of Specimen 08-5, where the East side was rougher, could be attributed to this recoater-induced particle redistribution. Near the gas-outlet, where spatter particles tended to accumulate, the recoating action may impose a powder sorting effect [11]: while smaller particles (<10 μm) tend to settle near the dispenser bin, larger particles tend to be pushed towards the overflow bin. This effect may have introduced significant non-uniformity in the surface roughness of Specimen 08-5 without well-defined directionality.

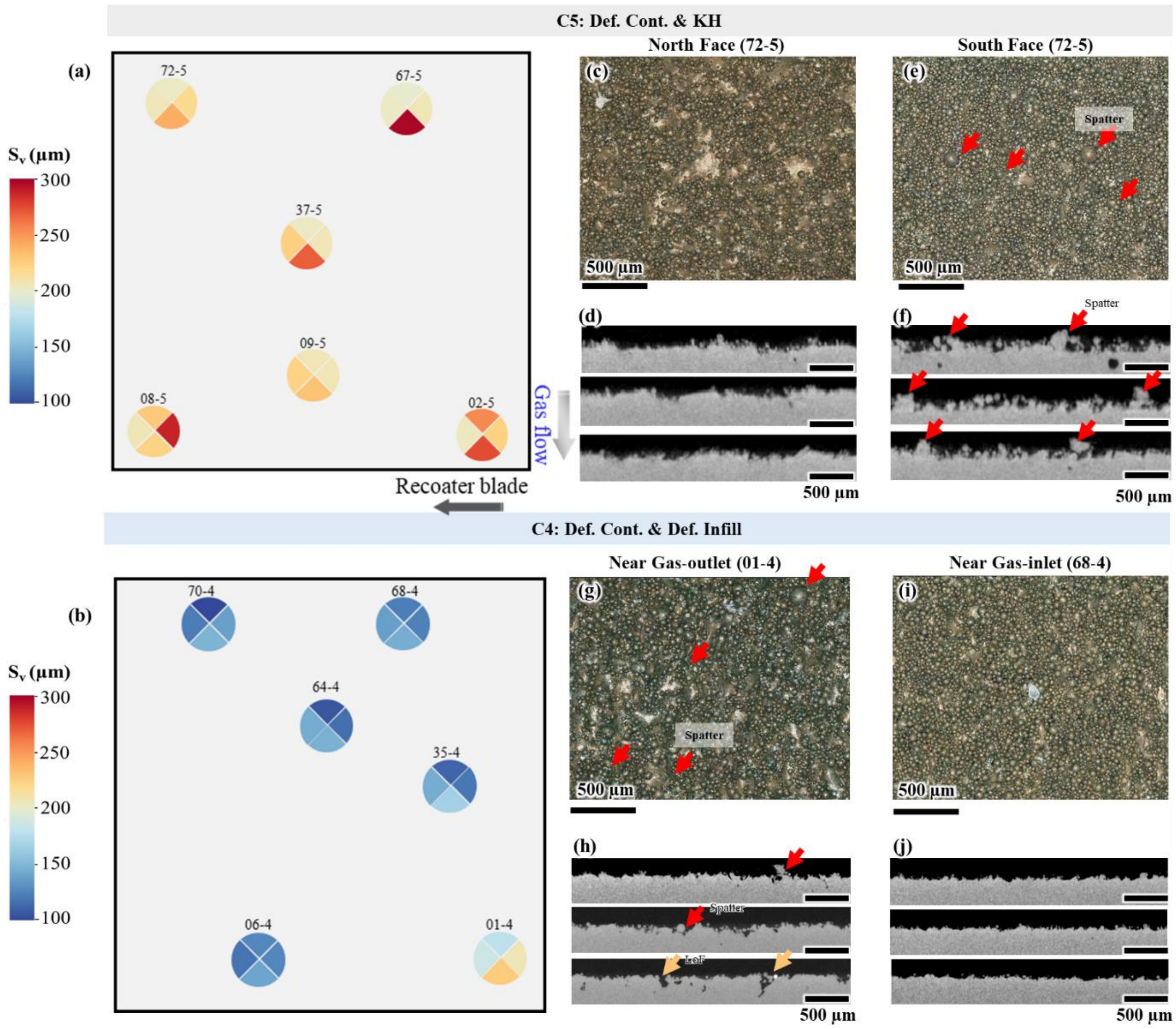

Figure 22 (a)-(b) Spatial location of specimens on the build plate for C4 and C5 conditions. (c)-(f) Representative optical images and XCT slices of the North and South faces of Specimen 72-5. (g)-(j) Optical images and XCT slices extracted from specimens in C4 condition located near gas-inlet and gas-outlet. Red and orange arrows indicate spatter particles and LoF, respectively.

3.3.3 Tensile behavior

The engineering stress-strain curves as well as quasi-static tensile properties, including yield strength (YS), ultimate tensile strength (UTS), and elongation to failure (EL), obtained from specimens tested in various process conditions are exhibited in **Figure 23**. Overall, the influence of contour strategies (compare C1, C2, C3, C7, and C8 conditions) as well as the infill conditions (compare C4, C5, and C6 conditions) on the YS and UTS was observed to be minimal. The minor differences (<5%) in YS and UTS across different conditions could be due to measurement errors of load-bearing area (from vernier caliper) because of adhered powder particles, which resulted in minor variations in calculated stresses. However, EL showed significant variations across different process conditions: no-contour conditions (i.e., C1, C2, and C3) exhibited lower EL than their counterparts with default-contour (i.e., C4, C5, and C6), while C7 and C8 specimens showed similar EL to the Default condition (i.e., C4). As for the effect of infill parameters, KH (i.e., C5) showed a slightly lower EL than Default (i.e., C4) and LoF (i.e., C6) conditions. These variations in EL could be ascribed to differences in surface texture and near-surface volumetric defects.

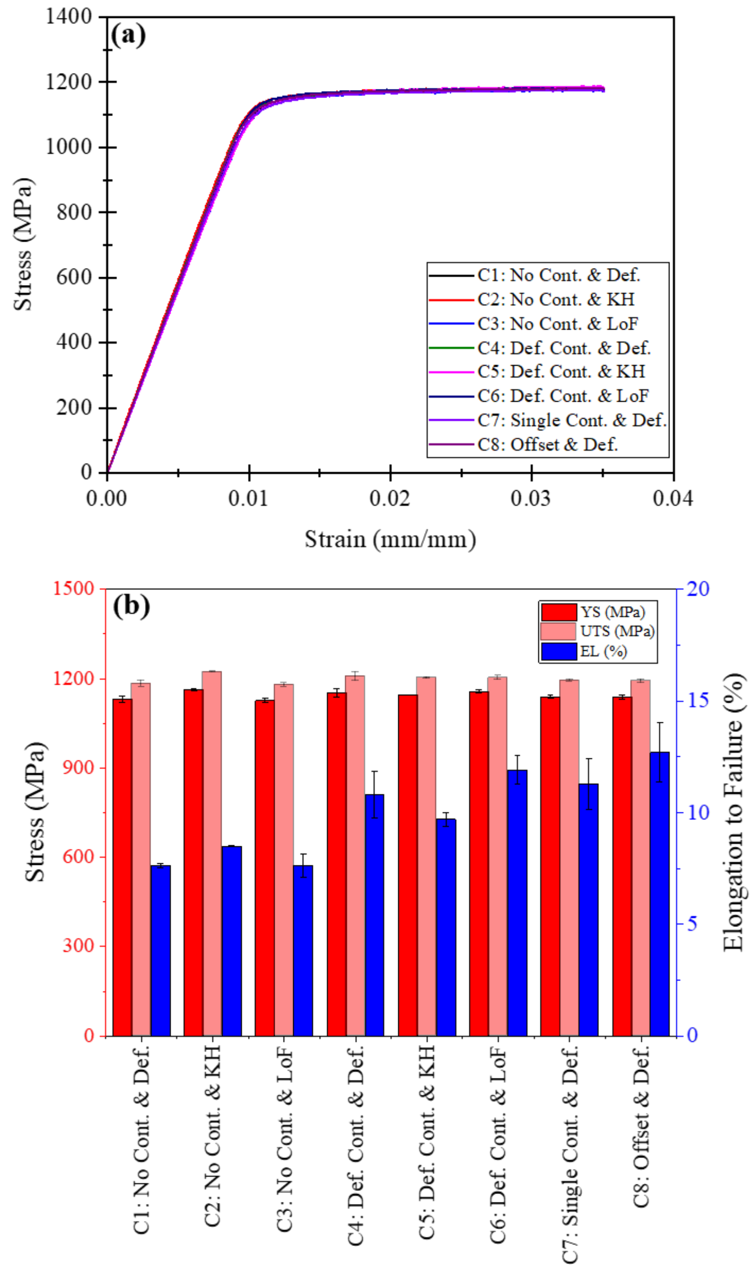

Figure 23 Quasi-static tensile behavior of L-PBF Ti-6Al-4V for various process conditions: (a) engineering stress-strain curves up to extensometer removal; (b) tensile properties, including YS, UTS, and EL.

To explain the variations in EL, the fractographs from SEM in all process conditions are compared in **Figure 24**. Unlike a well-known cup-and-cone fracture [105–107], where the fracture is marked by a central region and encircled by the shear lips, the fracture surfaces in all process conditions featured an elongated flattened region (indicated using yellow dashed ellipse) enclosed by shear lips at 45° to the loading direction and an opening of the flat region to the specimen surface. The magnified images at the opening showed fibrous structure, which is indicative of void nucleation, growth, and coalescence. Such asymmetric fracture could be ascribed to the presence of rough surfaces, where micro-notches act as stress risers and promote void nucleation [108]. In the cases of C1, C2, C3, and C5, several large voids could also be noticed in the near-surface regions of fracture surfaces (see **Figure 24(a)**, **(b)**, **(c), and (e)**). The slight reduction of EL in C1, C2, C3, and C5 specimens could be attributed to their higher roughness values as well as presence of these near-surface defects, both of which were effectively captured by the N/OH approach. These characteristics likely promoted void nucleation even further, therefore leading to premature failure and reduced EL.

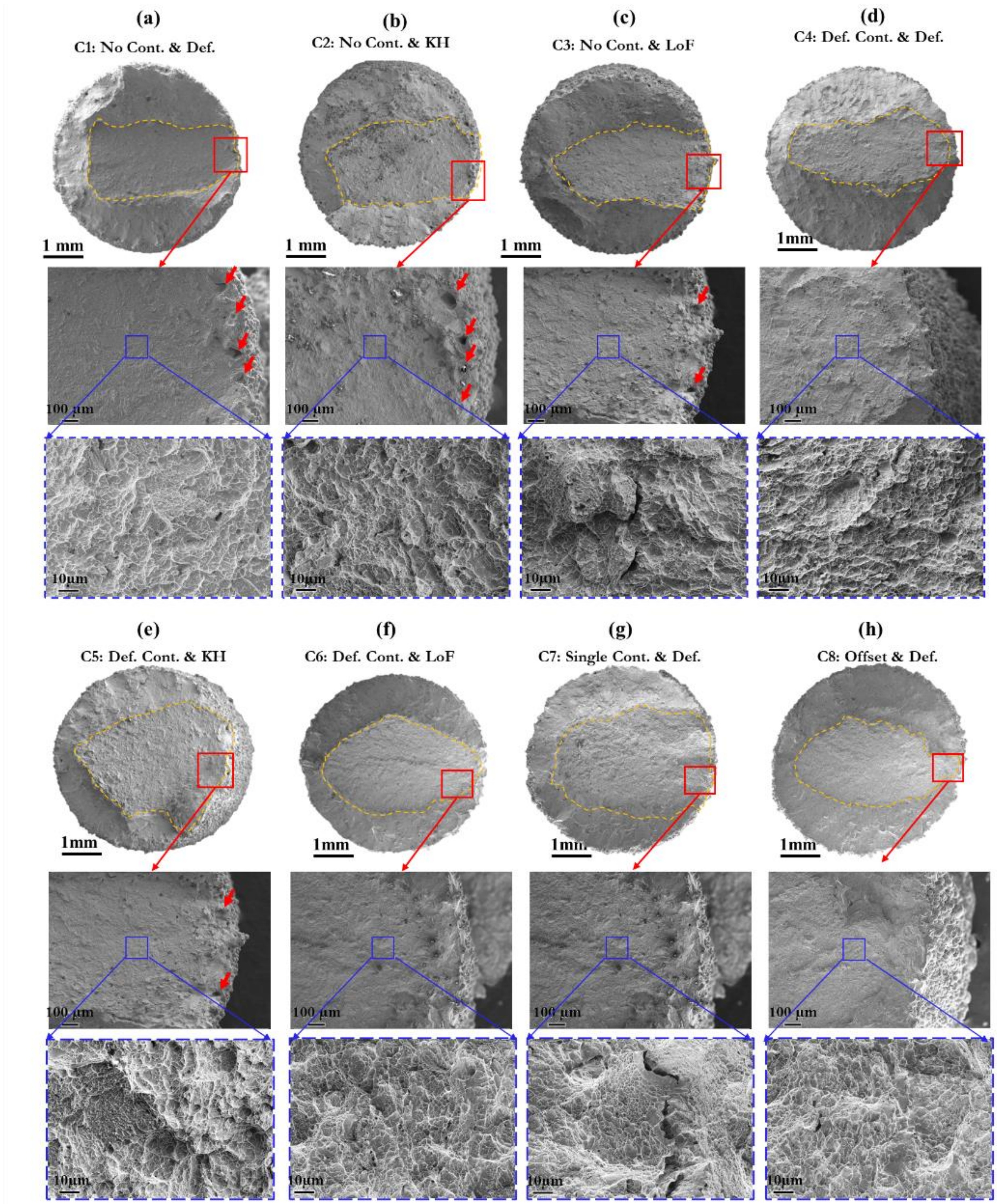

Figure 24 Tensile fracture surfaces of specimens for all the process conditions. Red arrows point at the near-surface volumetric defects.

3.3.4 *Fatigue behavior*

A summary of stress-life results is listed in **Table 8**. Moreover, these fatigue results are visualized in **Figure 25**, with maximum applied stress, σ_{max}, on the vertical axis and reversals to failure, $2N_f$, on the horizontal axis. At higher maximum applied stresses of 400 and 500 MPa, the influence of process variation (including different contour strategies and infill conditions) on fatigue lives was minimal, and only minor variations in fatigue lives were observed. At lower stress levels of 300 and 250 MPa, however, the scatter in fatigue lives across various conditions was more pronounced.

Table 8 Stress-life fatigue results for various process conditions.

Condition	Spec. ID	σ_{max}	$2N_f$
C1: No Cont & Def.	02-1	250	1401448
	51-1	250	>10000000
	59-1	250	672840
	13-1	300	514698
	21-1	300	561366
	32-1	300	574878
	08-1	400	130128
	23-1	400	135156
	72-1	400	117886
	48-1	500	60782
	67-1	500	57074
C2: No Cont & KH	07-2	250	1805084
	50-2	250	1054292
	71-2	250	898126
	12-2	300	460270
	24-2	300	961394
	52-2	300	525208
	04-2	400	154844
	58-2	400	128556
	65-2	400	166280
	14-2	500	85278

Condition	Spec. ID	σ_{max}	$2N_f$
	43-2	500	68346
C3: No Cont & LoF	03-3	250	1154146
	55-3	250	1668872
	66-3	250	656298
	15-3	300	567616
	54-3	300	468454
	56-3	300	385676
	26-3	400	120962
	42-3	400	150414
	44-3	400	146730
	10-3	500	65130
	20-3	500	48526
	30-3	500	59632
C4: Def. Cont & Def.	22-4	250	>10000000
	31-4	250	>10000000
	35-4	250	>10000000
	11-4	300	>10000000
	17-4	300	>10000000
	64-4	300	732044
	46-4	400	142076
	53-4	400	135750
	57-4	400	142344
	06-4	500	77366
	41-4	500	84146
	68-4	500	72284
C5: Def. Cont & KH	08-5	250	714392
	32-5	250	1562174
	45-5	250	1091756
	59-5 B	250	830932
	21-5	300	567244
	37-5	300	383388
	48-5	300	573984
	02-5	400	144380
	23-5	400	158978
	61-5	400	128270
	09-5	500	64934
	51-5	500	74792
	72-5	500	51668

Condition	Spec. ID	σ_{max}	$2N_f$
C6: Def. Cont & LoF	12-6	250	>10000000
	34-6	250	>10000000
	65-6	250	1054758
	04-6	300	305682
	43-6	300	395912
	52-6	300	443330
	07-6	400	152708
	58-6	400	126222
	63-6	400	115142
	18-6	500	65262
	50-6	500	80194
	71-6	500	73056
C7: Single Cont. & Def.	49-7	250	1068180
	54-7	250	721580
	69-7	250	1331848
	05-7	300	443384
	26-7	300	398036
	55-7	300	334580
	03-7	400	165098
	15-7	400	162034
	62-7	400	155282
	38-7	500	70274
	42-7	500	77084
	44-7	500	61828
C8: Offset & Def.	41-8	250	716426
	60-8	250	973346
	70-8	250	1023564
	01-8	300	407930
	11-8	300	386488
	45-8	300	234376
	06-8	400	129098
	22-8	400	143646
	68-8	400	136050
	35-8	500	61750
	47-8	500	66046
	64-8	500	67358

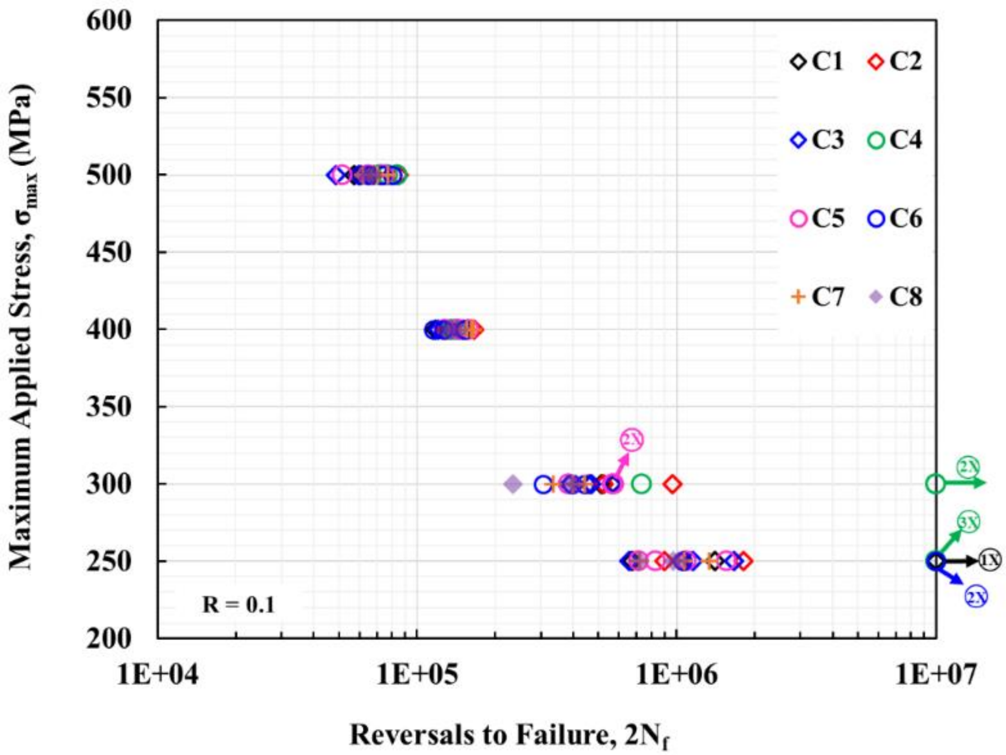

Figure 25 Stress-life results of specimens in different process conditions. The arrows indicate runouts.

Re-plots of the stress-life results illustrating the effects of contour settings on fatigue behavior are exhibited in **Figure 26(a)-(b)** and **Figure 28(a)-(b)**. Note that each of these sub-plots compared specimens fabricated with the same infill parameters, with only the variation being the contour scan parameters (i.e., no-contour, single-contour pass, default-contour passes, or modified beam-offset). For the Default infill condition, the specimens of default-contour (i.e., C4) showed longer fatigue lives compared to those of no-contour (i.e., C1), single-contour (i.e., C7) and modified beam-offset (i.e., C8) at 300 and 250 MPa (see **Figure 26(a) and (b)**). However, for the KH infill conditions (see **Figure 28(a)**), the beneficial effect of contour passes was greatly suppressed, as both C2 and C5 conditions showed similar fatigue lives. In the case of LoF infill conditions, the contour scanning had limited influence, with C6 showing longer fatigue lives only at 250 MPa, where two specimens reached runout (see **Figure 28(b)**).

To explain variations in fatigue lives due to changes in the process parameters, representative fracture surfaces of specimens for different process conditions at the maximum applied stresses of 400, 300, and 250 MPa are presented in **Figure 26(c)-(n)** and **Figure 27(c)-(k)**. At stress levels of 400 MPa, similar fatigue lives of specimens across all the process conditions could be ascribed to the high stress promoting rapid crack initiation. Fractography (see **Figure 26(c)-(f)** and **Figure 27(c)-(f)**) revealed that cracks often initiated from multiple locations, limiting the room for growth of each crack. As these cracks propagated and grew independently, they eventually coalesced and formed a larger crack, leaving behind ratchet marks (see white arrows in **Figure 26(c)-(f)** and **Figure 27(c)-(f)**) [66]. The similarity in fatigue lives at these stress levels could therefore be ascribed to significantly accelerated crack initiation and the dominance of crack growth phase, which was reported to be not as affected by the surface condition [32,66].

At lower stress levels of 300 and 250 MPa, the fracture surface of specimens of different process conditions are shown in **Figure 26(g)-(n)** and **Figure 27(g)-(j)**. For Default infill condition, default-contour specimens (i.e., the C4 ones) exhibited significantly longer fatigue lives than their counterparts with altered contour strategies (i.e., the C1, C7, and C8 specimens), except for the C4 Specimen 64-4 at 300 MPa and the C1 Specimen 51-1 at 250 MPa. This was reflected by the difference in crack initiating features between the C4 runout specimens and the fractured specimens of other conditions (e.g., compare **Figure 26(h) and (m)** with **Figure 26(g), (j), (l), and (n)**), with the C4 ones being much shallower. Note that the runouts from the C4 condition were retested at 400 MPa to induce failure. These specimens (**Figure 26(h) and (m)**) showed multiple crack initiation sites with limited crack growth regions, much like the fracture mechanism of C4 specimens directly tested at 400 MPa. This suggested that, during the initial testing at 300 and 250 MPa up to 10^7 reversals, no major cracks were developed due to the relatively smooth surfaces of these specimens; and upon retesting at 400 MPa, the multiple cracks simultaneously initiated and propagated. In contrast, all but one specimen from C1, C7, and C8 conditions (see **Figure 26(g), (j), (l), and (n)**) fractured at both 300 and 250 MPa and showed crack initiation from relatively deep micro-notches and rougher surfaces. In some cases, volumetric defects were observed to connect with free surface, sometimes at locations of surface valleys (see magnified views of **Figure 26(g), (l), and (n))**. These noticeably deeper micro-notches and surface connected defects caused early crack initiation and were responsible for the reduced fatigue lives of C1, C7, and C8 specimens than those of the C4 ones.

The exception among C4 specimens that exhibited a much shorter fatigue life, i.e., Specimen 64-4 at 300 MPa, had crack initiation from a deep micro-notch (see **Figure 26(i)**), where a LoF defect was also connected with the free surface. This likely caused early crack initiation and led to premature failure. The other exception, which was Specimen 51-1 in C1 condition, endured the loading at 250 MPa for much longer than other specimens, showed a single crack initiation site from the specimen surface when retested at 400 MPa (see **Figure 26(k)**). Although the rough surface features existed at the initiation site, they appeared to be grooves along the loading direction/specimen axis, which likely formed due to the termination of laser scan tracks, and posed little stress concentration.

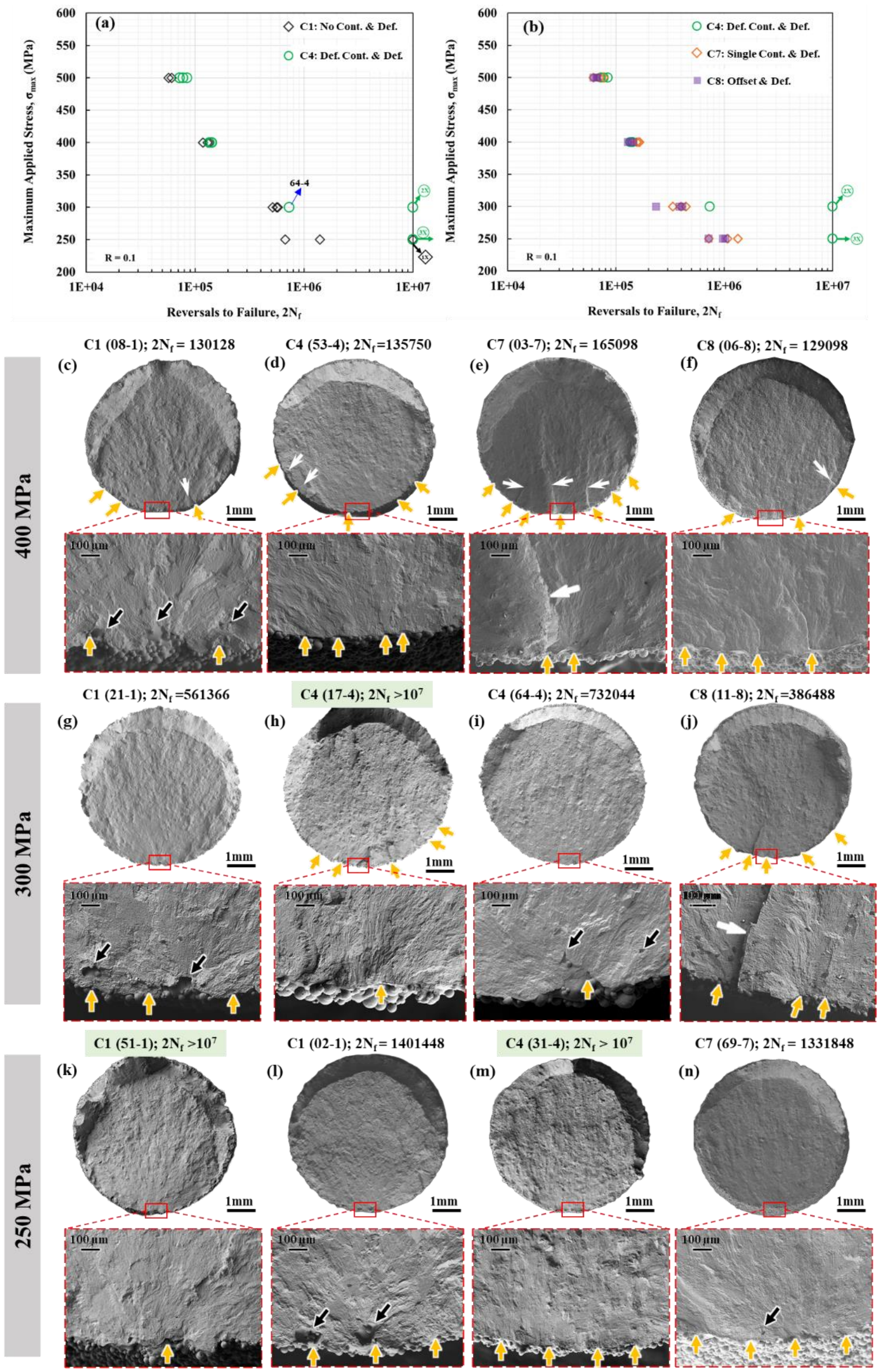

Figure 26 (a)-(b) Stress-life results showing the influence of contour strategies for Default infill conditions on the fatigue behavior of L-PBF Ti-6Al-4V. Corresponding representative fracture surfaces are also shown at maximum applied stresses of (c)-(f) 400 MPa, (g)–(j) 300 MPa, and (k)–(n) 250 MPa.

For the KH infill condition, contour passes had no effect on fatigue lives at 300 and 250 MPa; for the LoF condition, incorporating contour passes improved fatigue life at 250 MPa, where two C6 specimens achieved runout, except for the fractured Specimen 65-6. Fractography of one of the C6 runouts (i.e., Specimen 12-6, retested at 400 MPa) showed crack initiation from multiple sites, akin to the behavior of C4 runouts, with no near-surface or surface-connected defects due to relatively smooth surface features (see **Figure 27(k)**). In comparison, fractured specimens of C2, C3, and C5 conditions and Specimen 12-6 of C6 exhibited crack initiation from multiple closely spaced, deep surface micro-notches (see **Figure 27(g), (h), (i), and (j)**). In some cases, some near-surface and surface-connected volumetric defects were concentrated around the fracture periphery (see magnified views of **Figure 27(g), (h), and (i)**), which likely heightened the detrimental effects of these micro-notches. These characteristics likely led to accelerated crack initiation and caused shorter fatigue lives than the C6 runouts. On the other hand, irrespective of the contour strategy, specimens in both LoF and KH infill conditions showed similar fatigue lives at 300 MPa. Inspection of the fracture surface for both LoF and KH conditions at 300 MPa showed rough surface features, similar to the ones observed in **Figure 27(g), (h), (i), and (j)**, that caused rapid crack initiation and resulted in failure.

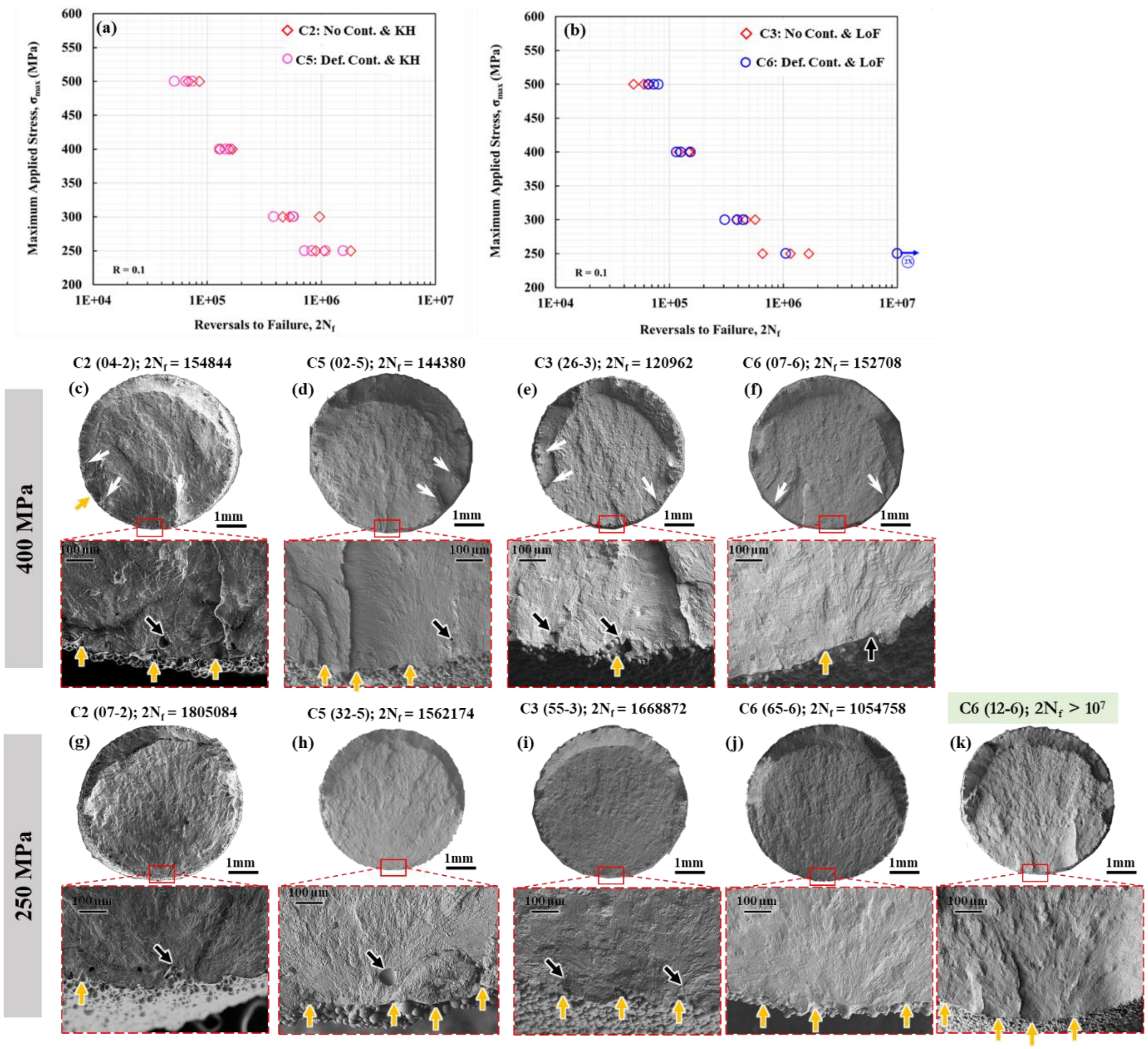

Figure 27 Stress-life results showing the effect of contour settings for (a) KH and (b) LoF infill conditions on the fatigue behavior of L-PBF Ti-6Al-4V. Corresponding representative fracture surfaces are also shown at maximum applied stresses of (c)-(f) 400 MPa, (g)–(j) 300 MPa, and (k)–(n) 250 MPa.

Stress-life results showing the effect of infill condition with the default-contour setting are shown in **Figure 28**. As seen, KH infill condition (i.e., C5 ones) showed shorter fatigue lives than Default (i.e., C4 ones) and LoF infill conditions (i.e., C6 ones), particularly at the stress level of 250 MPa. Fractography of a representative specimen from C5 condition tested at 250 MPa previously presented in **Figure 27(h)** has revealed deep surface micro-notches and the presence of near-surface volumetric defects. In contrast, the runouts from C4 and C6 conditions showed relatively smooth features and no near-surface volumetric defects (see **Figure 26(m) and 14(k)**). The interaction of surface and subsurface volumetric defects in C5 likely amplified the stress concentration [28,63], promoted early crack initiation, and reduced fatigue lives in C5 specimens.

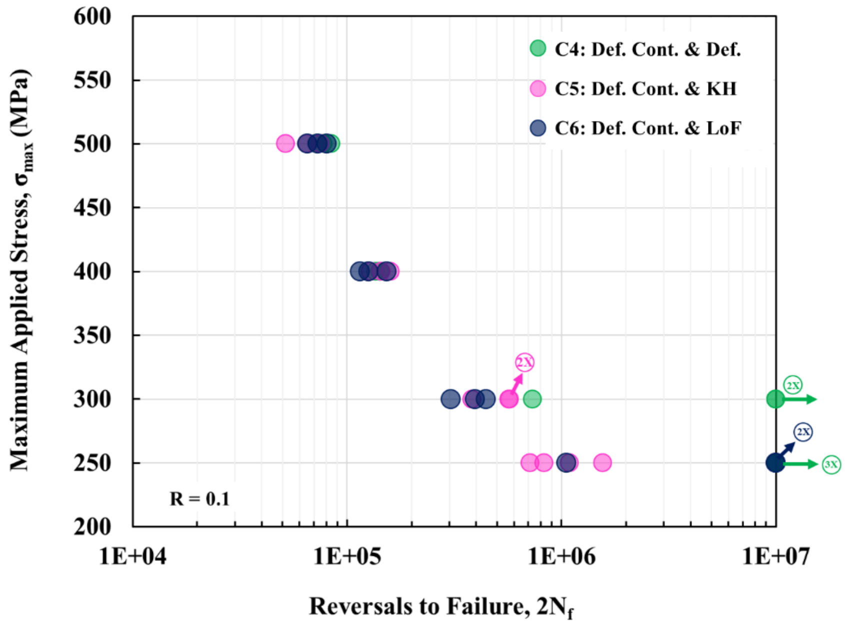

Figure 28 Stress-life results exhibiting the effect of infill parameters (and in default-contour condition) on the fatigue behavior of L-PBF Ti-6Al-4V.

The angular location of crack initiation was also visualized using a polar scatter plot, mimicking the circular cross-sections of the specimens in their physical orientation (see **Figure 29**). Each data point in the figure indicated the dominant crack initiation site of one specimen. The color intensity was used to reflect the KDE at each data point, where darker shades represented higher local crack initiation site density per unit angle along the perimeter. Interestingly, crack initiation tended to concentrate on the South side of specimens. One probable reason could be the predominantly higher surface roughness on the South side, which caused more severe stress concentration and favored fatigue crack initiation. These results highlight the importance of component's orientation during fabrication; specifically, if the particular side of part is fatigue-critical, it should be oriented away from South side.

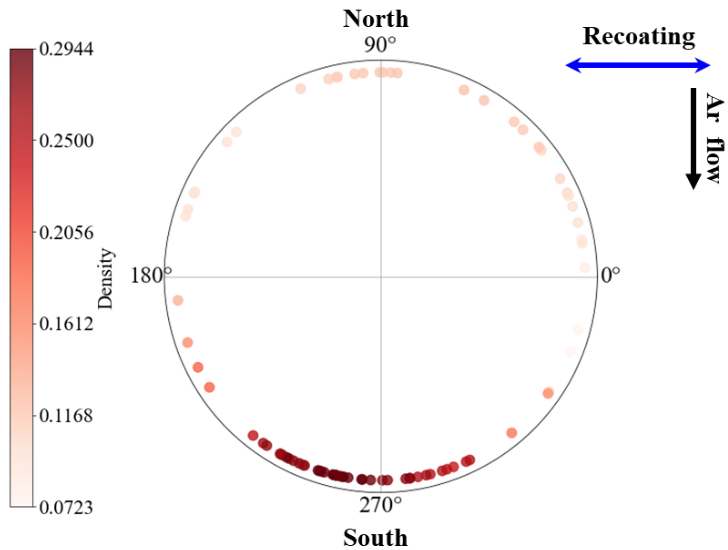

Figure 29 KDE plot of the fracture orientation of specimens in all process conditions and maximum applied stress amplitudes.

3.3.5 Fatigue modelling

Given that surface micro-notches mainly governed the fatigue behavior of the L-PBF Ti-6Al-4V specimens, the fatigue lives in all process conditions were estimated following the fatigue notch factor approach employed in Ref. [8]. Note that fatigue life predictions were made only for specimens scanned using XCT. For the modelling purposes, the reference data in machined and polished condition was extracted from the authors' previous work [8]. The fatigue lives of unmachined specimens were then estimated by applying the knockdown factor, K_f, to the fatigue limit of reference data. The severity of the notches was evaluated by Neuber's approach using the following formula:

$$K_f = 1 + \left[\frac{K_t - 1}{1 + \sqrt{\frac{\gamma}{\rho}}}\right], \qquad \text{Eq. (9)}$$

where K_t is an elastic stress concentration factor, ρ denotes curvature radius of micro-notch, and γ represents the material's characteristic length (the smallest microstructural unit), which was taken as 2.5 µm according to Ref. [73]. K_t was evaluated using the Inglis's equation, which incorporated two spatial parameters of the notch: the depth, *d*, and the width, *w*. The equation is as follows:

$$K_{t1} = 1 + \frac{2d}{0.5w}. \qquad \text{Eq. (10)}$$

The notch parameters, including both *d*, *w* and, ρ, were evaluated following the approach in authors' previous work [8], where for every scanned specimen *d*, ρ, and *w* of each valley in the gage surface were determined. The K_t values were then evaluated for all the surface valleys (totaling 30,000 to 35,000) of each specimen using the extracted *d*, ρ, and *w* values. Next, the corresponding fatigue notch factor, K_f, for each of those notches was evaluated. For modeling purposes, the surface valley with the highest K_f value in each specimen was selected to represent the most critical notch.

To estimate the fatigue lives of an unmachined specimen, first the fatigue strength at 2000 reversals, $\sigma_{f,2\times10^3}$, was determined. This was done using the fatigue strength fraction factor f = 0.85, which was evaluated based on the ultimate tensile strength of L-PBF Ti-6Al-4V [11]. Using an average UTS value of 1188 MPa, $\sigma_{f,2\times10^3}$ was evaluated to be ~1010 MPa. The fatigue limit, σ_e^{um}, was then calculated by applying the knockdown factor, K_f, to the fatigue limit of the reference data, σ_e [8]. The stress-life behavior of all the unmachined specimens was then evaluated by interpolating between the $\sigma_{f,2\times10^3}$ and σ_e^{um} using a power law function.

Excluding the runout specimens, 80% of the estimations fell within the scatter band of ±2, while 100% fell within the scatter band of ±3 (see **Figure 30**). Notably, predictions of runout tended to fall in the conservative side, where failure was predicted despite the runout. This is often desirable for safe design considerations. Overall, this approach of taking only the notch parameters (*d, w, ρ*) could reasonably predict the fatigue lives of the unmachined specimens, irrespective of the process conditions.

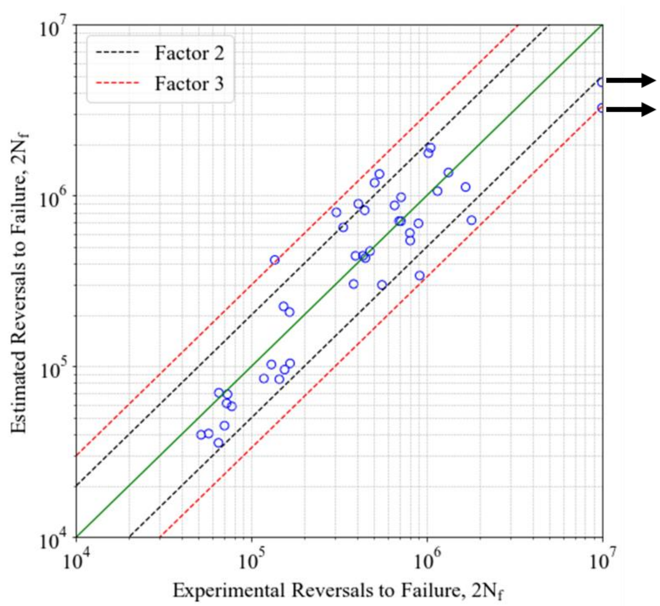

Figure 30 The predicted fatigue lives vs. the experimental fatigue lives of L-PBF Ti-6-Al-4V of unmachined specimens in all process conditions. The black and red dashed lines enclose the scatter bands of factors of 2 and 3, respectively, while black arrows indicate runouts.

3.4 Conclusions

This study examined the individual and combined influences of various process variables on the surface texture and near-surface conditions as well as the tensile and fatigue behaviors of laser powder bed fused Ti-6Al-4V. Both infill and contour settings were varied to generate a wide range of surface characteristics. X-ray computed tomography was used to characterize these surfaces, and scanning electron microscopy was used for fractography. In addition, the influence of surface roughness on fatigue lives was modelled utilizing a fatigue notch factor approach. Based on the findings, the following conclusions can be drawn:

1) Overheated infill conditions (both default and no-contour) exhibited a larger population of defects in the near-surface regions compared to underheated and EOS-recommended infill conditions. When subsurface defects were treated as valleys, no-contour specimens showed higher surface roughness than their counterparts with contour passes, except for ones with overheated infill conditions, where the near-surface defect population was similar. Applying single-contour or increasing the beam-offset partially remediated the near-surface defects and slightly reduced roughness.
2) Across all the process conditions, specimens with contour passes generally exhibited directional roughness, where the side facing away from the gas flow showed higher S_a and S_v values. This was ascribed to the preferential deposition of spatter along the direction of gas flow. This trend, however, was less noticeable near the gas-outlet where greater spatter accumulation, reduced gas velocities, and recoater-induced particle redistribution collectively influenced surface roughness.
3) Tensile strengths were largely insensitive to process-induced variations in surface texture and near-surface defects; however, the elongation to failure was slightly lower for no-

contour specimens than for specimens with contour passes due to increased roughness, which provided ample sites for void nucleation. Single-contour pass and modified beam-offset did not noticeably affect the elongation to failure.

4) The beneficial effect of contour passes on surface quality and fatigue lives was most evident in specimens with default infill condition and, to a lesser extent, in underheated conditions at lower applied stresses. However, the contour passes were not effective in removing the near-surface volumetric defects induced by the overheated infill condition and were ineffective in improving the fatigue life.

4 Tensile and fatigue behaviors of additively manufactured Ti-6Al-4V: Influence of surface texture and removal

4.1 Introduction

Ti-6Al-4V is widely used in aerospace and automotive industries owing to its attractive combination of high strength-to-weight ratio, acceptable fatigue performance, and corrosion resistance [41]. The growing demand for lightweighting with enhanced functionality in these industries calls for the development of robust and complex configurations of parts [109]. Recently, additive manufacturing (AM) has received increasing popularity due to its ability to manufacture complex topologically optimized geometries and consolidate several parts into monolithic components that significantly reduces processing and tooling cost [13]. For instance, by consolidation of multiple pieces of fuel nozzle into a single part, GE Aviation has achieved a 25% weight reduction and a 30% improvement in cost efficiency [3]. However, additively manufactured (AM) parts often show significant variability in their fatigue performance compared to their wrought counterparts [110,111] due to the presence of surface anomalies and volumetric defects (i.e., gas entrapped pores, keyholes, and lack of fusions) [112,113]. This hinders the qualification and widespread adoption of AM parts in fatigue-critical applications [114].

In order to mitigate the detrimental effects of surface and near-surface defects, prevailing approaches include non-conventional techniques (i.e., abrasive flow machining, chemical etching, and electrochemical polishing) and conventional ones such as machining [33,53,115]. While non-conventional processes could be employed due to their ability to access hard-to-reach regions in complex geometries, these processes typically fail to eliminate form error and, in some cases, are unable to meet geometric tolerances [116,117]. For components that rely on these tolerances, machining is still a necessary post-processing step. However, machining Ti-6Al-4V is challenging due to its low thermal conductivity, high chemical reactivity, and strength, which cause excessive tool wear [12].

Considering this, an important question arises: to what extent should material be removed to reduce machining challenges and costs while also eliminating surface and near-surface defects? One desirable approach could be direct polishing (P) the surface at critical locations along the direction of the principal stresses. This method may be a strategic choice for slender parts as it avoids the use of the high cutting forces of conventional machining that could compromise the dimensional accuracy. However, Lee et al. [20] noted no improvement in fatigue lives (despite significant enhancement in surface finish) of laser powder bed fused (L-PBF) Ti-6Al-4V specimens. This was because the P only removed powder granules and some surface peaks, yet residual valleys still existed below the free surface of the specimens that caused early failure. This issue could be circumvented by completely removing the as-fabricated characteristics of L-PBF (i.e., surface micro-notches and powder particles), that typically penetrate up to the depth of ~300 μm via shallow machining (SM) [63,116]. While SM was reported to achieve an average reduction of 98% in mean roughness, R_a, of L-PBF Ti-6Al-4V parts, fatigue lives showed mixed results: one study on L-PBF Ti-6Al-4V reported an average improvement by a factor of ~2 in fatigue lives [118], while another study on electron powder bed fused Ti-6Al-4V specimens observed no improvement in fatigue lives. The latter results were attributed to the exposure of near-surface defects to surface after material removal [116].

Given these subsurface defects, it may be tempting to opt to machine deeper into material, referred to as deep machining (DM), to eliminate them. However, the location of these volumetric defects cannot be ascertained as some large defects may reside deeper in the material [112]. This is critical because DM might inadvertently expose some internal defects to the surface, similar to

SM. In the worst case, DM may expose internal defects to near-surface regions, which may initiate fatigue cracks that quickly open to the surface during fatigue loading, rapidly forming large initial cracks that eventually lead to part failure and essentially negating any potential benefits of machining. Indeed, Yadollahi et al. [1] observed no improvement in fatigue lives of L-PBF Inconel 718 specimens due to exposure of internal defects to surface and near-surface regions after DM. The tensile properties, on the other hand, were reported to be insensitive to the presence of surface and near-surface defects after DM [11]. However, examinations of P and SM treatments' influence on tensile behavior have been lacking, and specifically the effect of material removal depth on tensile properties of L-PBF Ti-6Al-4V remains unclear.

Such a complex interplay between the depth of material removal and the random distribution of defects (both surface and subsurface) and their subsequent influence on the mechanical performance of AM Ti-6Al-4V parts due to their elevated defect sensitivity necessitates further research. Therefore, this work aims to investigate the influence of various forms of material removal on the tensile and fatigue behaviors of L-PBF Ti-6Al-4V. All the specimens were built in vertical orientation and stress relieved, followed by the application of four different material removal treatments: (1) P, (2) SM and polishing (SM+P), (3) DM, and (4) DM and polishing (DM+P). The texture of all treated and untreated (UT) surfaces was characterized using X-ray computed tomography (XCT), and the corresponding mechanical behavior was evaluated, with the UT specimens serving as the baseline. In addition, the fatigue modeling of the specimens with prominent surface roughness was performed following the fatigue notch factor approach.

4.2 Methodology

In this study, plasma-atomized powder from AP&C with chemical composition illustrated in **Table 9** was used to manufacture both tensile and fatigue sets. All sets were fabricated using the EOS M290 L-PBF system with recommended process settings, which were as follows: power of 280 W, scanning speed of 1200 mm/sec, hatching distance of 0.14 mm, and layer thickness of 30 μm. Following fabrication, both tensile and fatigue specimens were stress relieved at 704°C for 1h followed by furnace cooling. Both sets were then detached from build plates using a bandsaw.

Table 9 Chemical composition of Ti-6Al-4V powder provided by AP&C.

O	Al	V	Fe	C	N	H	Y	Ti
0.2	6.75	4.5	0.3	0.08	0.05	0.02	0.01	Bal.

The drawings of tensile and fatigue specimens in their final dimensions are shown in **Figure 31**. Tensile specimens were designed according to ASTM E8 standard [91], while the fatigue specimens were designed according to ASTM E466 standard [58] with some slight deviations. The gage length was reduced to 5 mm to allow the XCT of one entire gage section in each session with sufficient resolution. Note that SM+P and DM specimens (i.e., the specimens that underwent SM+P and DM treatments) were fabricated in their near net shapes and respectively oversized from the final geometries by 0.2 and 2 mm in diameters.

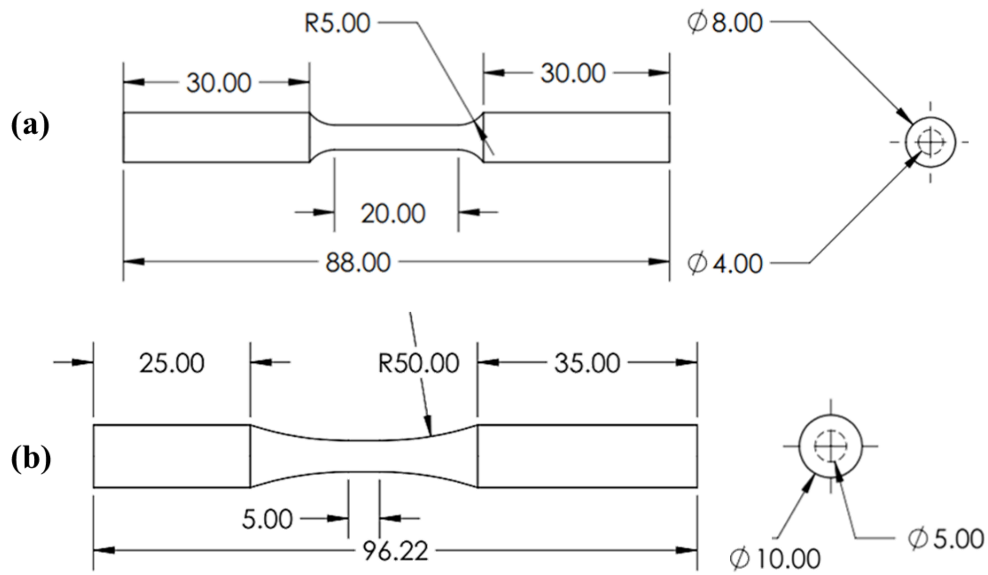

Figure 31 Design of (a) tensile and (b) fatigue specimens in their final dimensions. All the dimensions are in mm.

Prior to mechanical testing, surface and volumetric defect characterization was performed on two representative specimens from each condition using the Zeiss Xradia 620 XCT system. The scans were performed using a voxel size of 5.3 μm, an accelerating voltage of 140 kV, and a power of 21 W, covering a total scanned volume of 108 mm^3. For reconstruction, the proprietary software from Zeiss was utilized, while the volumetric defects were visualized using Dragonfly software. The surface texture analysis was carried out using the Python algorithm provided in the authors' previous work [8], and the surface topography parameters such as areal arithmetic mean roughness, S_a, and maximum areal valley depth, S_v, were evaluated following the ISO 25178-2:2021 standard [119]. Moreover, the optical microscopy (OM) using a Keyence VHX-6000) was employed to capture overall visual appearances of the surfaces.

An MTS servo-hydraulic machine with a 100 kN load cell was used to conduct both tensile and fatigue testing. Strain/displacement-controlled tension tests followed ASTM E8 [91], and they proceeded up to a strain value of 0.030 mm/mm, at which point the extensometer was removed to avoid extensometer's damage. The tests then continued in displacement mode until fracture. Three tests were conducted for each condition, and tensile properties including 0.2% offset yield strength (YS), ultimate tensile strength (UTS), and elongation to failure (EL) were recorded for all tests with their average and standard deviation values reported. Force-controlled fatigue testing was performed according to ASTM E466 [58] under a stress ratio, R_{σ}, of 0.1. For conditions such as UT and P, the maximum applied stress was calculated by dividing the applied force by the effective cross-sectional area. The diameter of these cross sections was determined by subtracting twice the maximum areal height, S_z, of the scanned surface from the gage diameter measured with vernier caliper. Each test continued until the complete specimen's separation or was considered a runout if the specimen survived 10^7 reversals. After testing, specimens were cleaned in a sonicator using a mixture of acetone and isopropanol, and then fractography was performed using a Zeiss Crossbeam 550 scanning electron microscope (SEM).

4.3 Experimental Results and Discussion

4.3.1 Surface Texture and Volumetric Defects Analyses

The specimens' surfaces in different conditions captured with XCT and OM are shown in **Figure 32(a) & (b),** respectively. In addition, the areal height maps of the representative specimens obtained after XCT surface texture analysis are presented in **Figure 32(c)**. Both XCT and OM views (see **Figure 32(a) & (b)**) revealed that the UT specimens had partially-melted/unmelted powder particles attached to the surface. To assess the effectiveness of P treatment in material removal, the XCT sliced views were compared before and after the treatment at the same location. The P treatment appeared to eliminate only the partially fused powder granules, while residual valleys and near-surface defects still existed. Additional comparison via the areal height maps (see **Figure 32(a)**) of both UT and P specimens showed the presence of interconnected residual valleys surrounded by flattened surface regions. This suggested that P treatment may not be effective in improving fatigue performance, as the residual valleys and near-surface defects still remained [20,120]. In SM+P condition, although the rough surface characteristics were adequately removed (see **Figure 32(a) & (b)**), some near-surface defects were still present. The OM view further revealed some surface defects, which were likely either near-surface defects that opened to the surface or residual valleys persisting at the surface. On the other hand, both DM and DM+P exhibited fully flattened surfaces (see **Figure 32(a) & (c)**). OM view (**Figure 32(b)**) showed that DM specimens had machining grooves that aligned perpendicular to the loading direction, while DM+P specimens exhibited polishing marks parallel to the build direction.

The evaluated surface roughness parameters, such as S_a and S_v, in all conditions are presented in **Figure 32(d) & (e)**. In general, S_a and S_v values decreased as the depth of material removal increased; P specimens recorded the highest values of S_a (4 μm) and S_v (25 μm), while DM+P specimens had the lowest values of S_a (1.2 μm) and S_v (4 μm). Notice that the overall values of S_a and S_v dropped in P despite the presence of surface valleys. This could be ascribed to the removal of powder granules that lowered the global mean plane level, which reduced both the average height values, S_a, (because of removal of peaks) and the distance from the mean plane to the lowest pit, S_v, of the scanned surface. These findings highlight a possible limitation of standard roughness parameters, which may not necessarily capture the localized features critical to mechanical performance because they are mere statistical measures of the surface topography and are highly influenced by the overall surface topography [20].

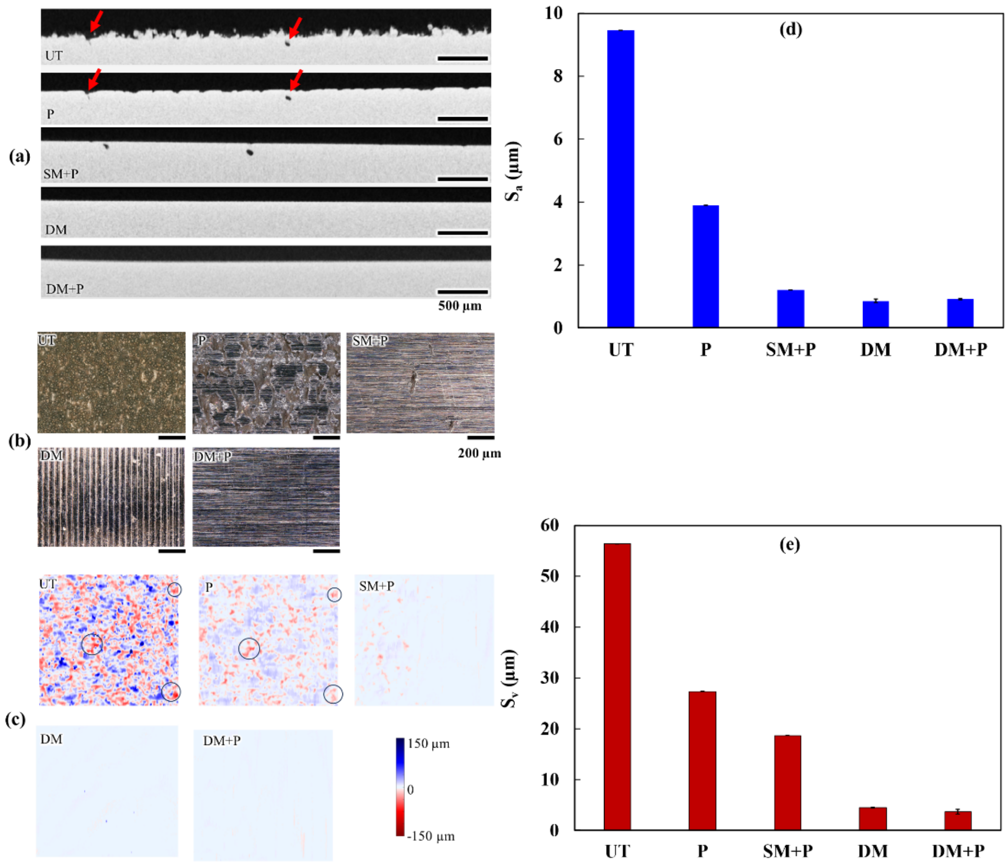

Figure 32 Surface quality of specimens in various material removal conditions: (a) XCT sliced view (red arrows in UT and P indicate the same location before and after material removal), (b) optical surface view, and (c) areal height maps of all conditions (UT, P, SM+P, DM, and DM+P), with circles indicating matching features in UT and P specimens. Panels (d) and (e) present bar plots of S_a and S_v parameters.

Additionally, the volumetric defects in the representative specimens were analyzed to understand the effects of various material removal processes on near-surface regions (see **Figure 33)**. Note that the color bar indicates the defect size by volume. The largest defect for each condition is magnified in the figure. The UT specimen and the ones that did not undergo significant material removal, including P and SM+P specimens, showed the clustering of defects that formed a ring near the periphery of specimens (see **Figure 33(b) & (c)**). The largest defects within each condition tended to exist near the ring, which likely corresponded to the interface between the contouring and infill conditions; this region extended up to ~300 μm below surface [88]. The shape of these defects ranged from somewhat irregular to spherical. These near-surface defects may result from insufficient overlap between infill and contouring regions or from the laser slowing down at the edges of the scan track, causing overheating and forming porosity [121,122]. P and SM+P respectively removed ~50 μm and ~150 μm of material from the surface (in radial depth), which appeared to be insufficient to eliminate near-surface defects (see **Figure 33(b) & (c)**). Following substantial material removal of 1 mm from surface, as in the cases of DM and DM+P, no near-surface defects were detected. Instead, defects appeared to be randomly distributed, mainly within the infill regions (see **Figure 33(d) & (e)**).

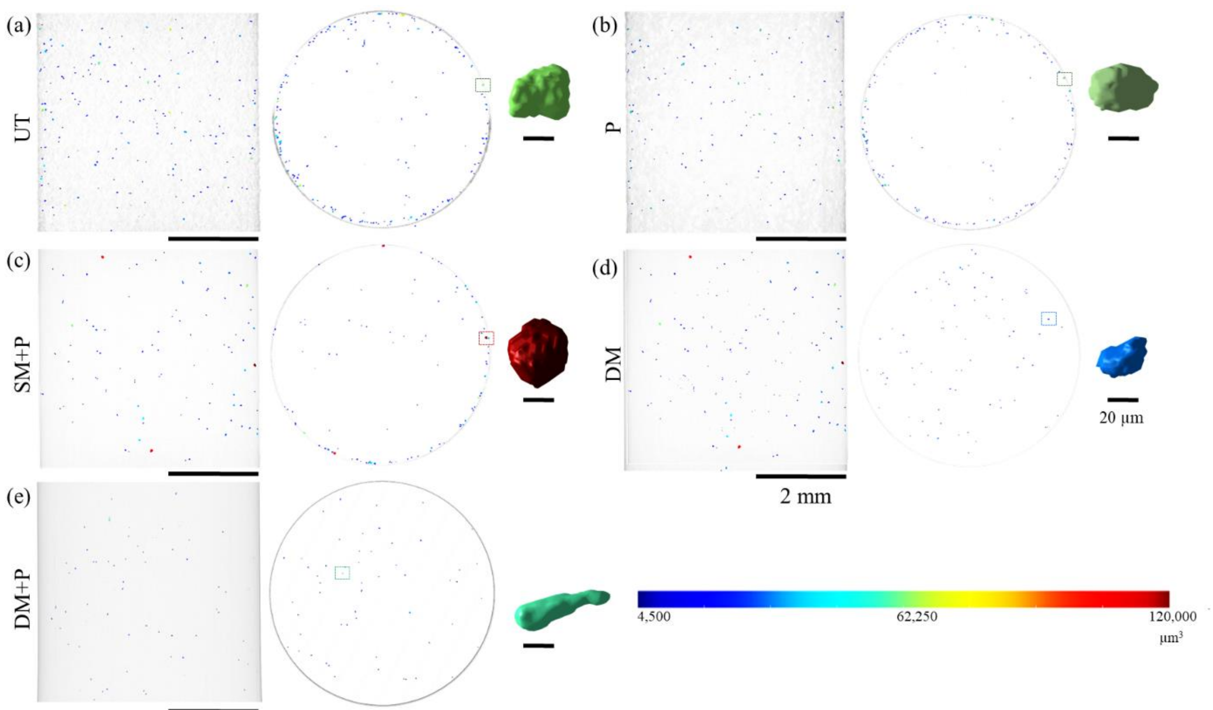

Figure 33 The 3D visualization of volumetric defects in various conditions: (a) UT, (b) P, (c) SM+P, (d) DM, and (e) DM+P. The magnified view of the largest defect is shown besides each corresponding condition.

4.3.2 Tensile Behavior

The tensile properties, including YS, UTS, and strain to fracture, ε_f, of specimens in various conditions are shown in **Figure 34**. YS and UTS were insensitive to the surface conditions. The slight variations in strengths could be due to minor errors in measuring the gage diameter with a caliper rather than microstructural differences since all the specimens underwent identical stress-relief treatment. On the other hand, strain to fracture, i.e., ε_f, significantly varied across different conditions; UT specimens showed the lowest ductility (~0.07), followed by P specimens (~0.22), while SM+P, DM, and DM+P specimens exhibited comparable ductility (~0.30), which was notably higher than those of UT and P specimens. Interestingly, SM+P specimens, despite being rougher and having higher S_a and S_v values compared to DM and DM+P specimens, did not show significant reduction in ductility. Compared to wrought [123] and cast (HIP and machined) Ti-6Al-4V [123] data, L-PBF specimens had higher UTS and YS across all the surface conditions. While the ductility of wrought specimens was somewhat similar to that of SM+P, DM, and DM+P conditions, cast specimens showed slightly lower ductility than these conditions but still higher than the UT condition.

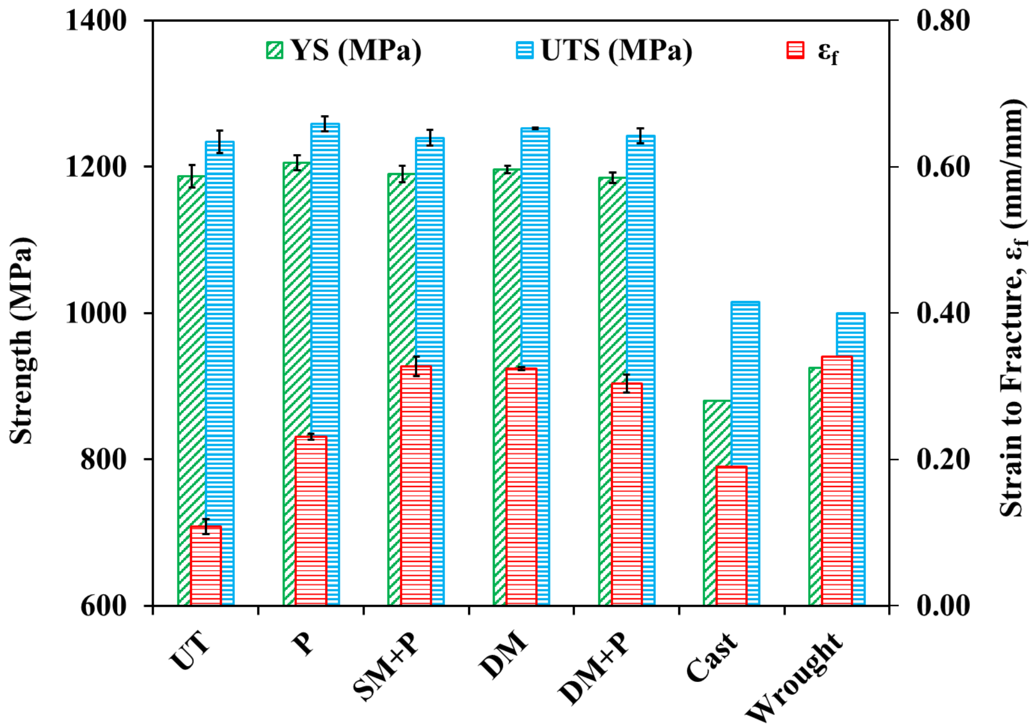

Figure 34 Quasi-static tensile properties of L-PBF Ti-6Al-4V in different surface conditions. Note that cast and wrought data was taken from Ref. [123].

To understand the variation in ductility across the conditions, some representative fractographs of each condition are compared in **Figure 35**. The SM+P, DM, and DM+P specimens (see **Figure 35 (a)-(c)**) showed typical cup-and-cone fracture characterized by a central flat region and enclosed by shear lips corresponding to the final tear-off stage at approximately 45° to the loading direction. The magnified views of the central regions revealed fibrous features with dimples of ~2-3 µm in size, which is indicative of ductile fracture. These fracture characteristics were the result of the nucleation, growth, and coalescence of voids that formed a central fibrous structure within the necked region of the gage section [107,108].

In comparison, UT and P specimens showed asymmetric or anomalous fracture morphology, where the central region was not fully enclosed by the shear lips and an "opening" to the surface was noticed (see **Figure 35(d)** & **(e)**). The cracks originated near the surface and along one side of the specimen (indicated by yellow arrows in **Figure 35(d)** & **(e)**), propagated towards the opposite edge, and ultimately culminated in shear lip formation. Higher magnification images from the central regions of both UT and P fractured specimens revealed fibrous structure, which indicated ductile fracture. These findings were summarized in a schematic illustration (see **Figure 35(f)** & **(g)**), where the specimen with relatively low roughness and symmetrical fracture was contrasted against the one with a rougher surface leading to asymmetric fracture. The reduced ductility in UT and P specimens could be ascribed to rough surface features and presence of near-surface volumetric defects, which possibly served as localized stress risers and provided ample sites for voids nucleation. As a result, crack initiation occurred much earlier, often without significant necking, and overall fracture deviated from the typical cup-and-cone fracture observed in SM+P, DM, and DM+P specimens. While SM+P specimens exhibited some surface anomalies, they appeared to be not severe enough (due to reduced roughness values) to compromise the ductility.

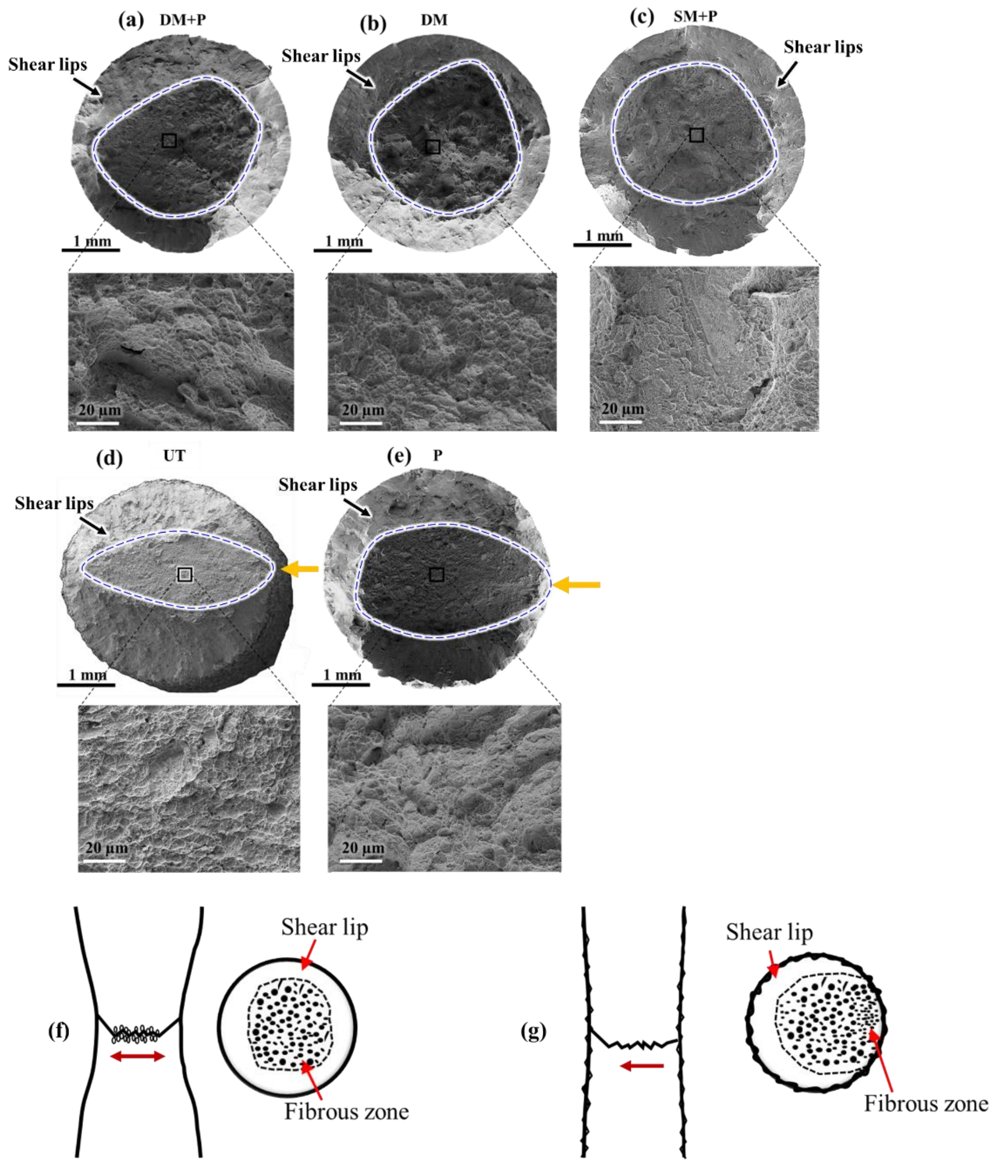

Figure 35 Tensile fracture surfaces of L-PBF Ti-6Al-4V in different conditions: (a) DM+P, (b) DM, (c) SM+P, (d) UT, and (e) P. Yellow arrows indicate surface crack initiation locations, while blue ellipses encircle fibrous regions surrounded by shear lips. Schematic illustration of tensile fracture modes: (f) typical cup-and-cone fracture and (g) asymmetric fracture morphology.

4.3.3 Fatigue Behavior

The influence of various material removal processes on fatigue behavior is visualized using a stress-life fatigue plot (see **Figure 36**), which shows maximum applied stress, σ_{max}, on the Y-axis and reversals to failure, $2N_f$, on the X-axis. The runout specimens for each condition are indicated using arrows. The fatigue lives significantly varied depending on the amount of material removed; the condition with minimal material removal, i.e., P, showed similar fatigue lives to UT specimens across all the maximum applied stresses, while SM+P exhibited slightly longer fatigue lives, and the difference in fatigue lives grew bigger at relatively low stress amplitudes (400 MPa and lower). DM and DM+P, on the other hand, exhibited over 2 orders of magnitude improvement in fatigue lives. Between the two conditions, the fatigue limit of DM+P was marginally better, with all tested specimens reaching runout at 600 MPa, whereas DM had all tested specimens reaching runout at 550 MPa. The fatigue performance across various surface conditions from this study was compared with literature data for wrought [124] and cast Ti-6Al-4V [125]. Wrought specimens had similar fatigue lives to those of the DM and DM+P conditions. In contrast, the cast specimens exhibited shorter fatigue lives than both DM conditions but had similar fatigue lives to SM+P at higher stress levels and notably longer lives than SM+P at lower stress levels.

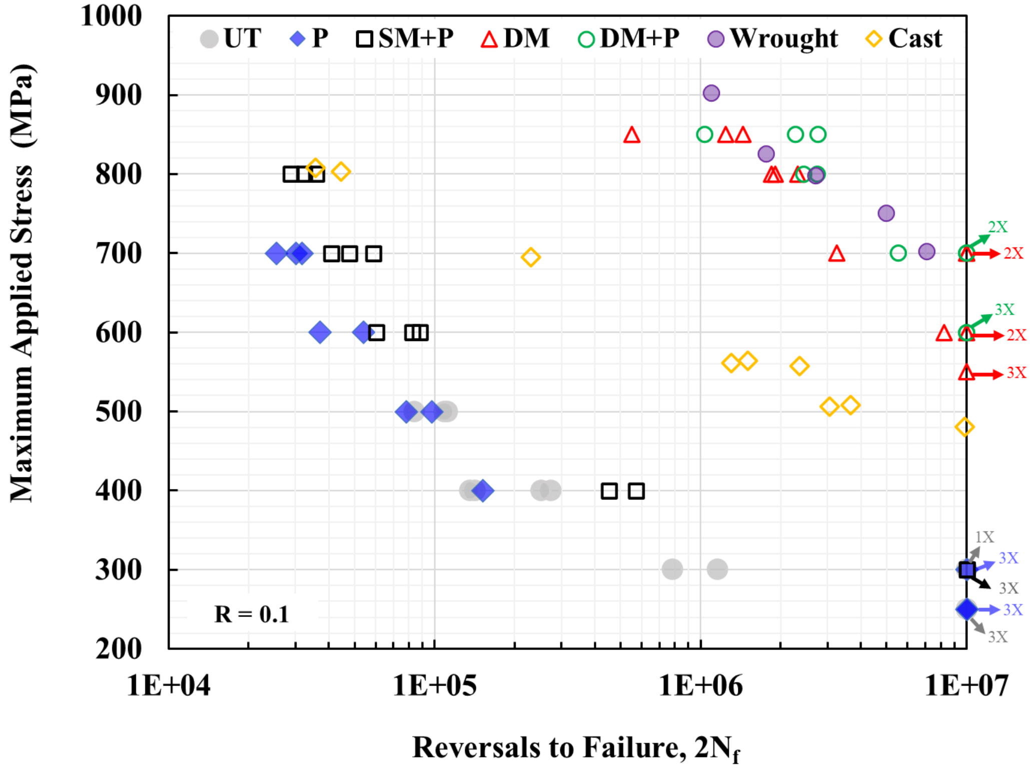

Figure 36 Stress-life fatigue results for all surface conditions of L-PBF Ti-6Al-4V. The arrows indicate the runouts. The fatigue data for wrought and cast Ti-6Al-4V was extracted from Refs. [124,125].

The variation in fatigue lives among various conditions could be attributed to the differences in surface roughness and volumetric defect characteristics such as type (i.e., lack of fusion, keyholes, and pores), size, and location, which influenced the crack initiation behavior. P specimens did not show any improvement in fatigue lives due to the presence of remnant surface valleys (see **Figure 32(b) &(e)**), which caused localized stress concentration, as the surface notches in UT specimens did, and accelerated the crack initiation stage of fatigue life. Fractography showed a similar fracture mechanism to UT specimens (compare **Figure 37(a)** with **Figure 37(b)**), where multiple crack initiation sites originated from the surface micro-notches. The SM+P, which mostly removed the partially melted powder and surface valleys, showed crack initiation predominantly from the surface-connected defects (see **Figure 37(c)**). Near-surface defects (indicated by yellow arrows in **Figure 37(b) & Figure 37(c)**) were often observed in both P and SM+P conditions, which likely exacerbated the detrimental effects of surface notches [63,67].

At a higher stress level of 700 MPa, SM+P showed multiple crack initiation sites once again originating from the surface-connected volumetric defects (see **Figure 37(d)**). Additionally, several volumetric defects were observed in the near-surface regions. The crack initiation from multiple sites suggested that cracks initiated simultaneously or in rapid succession from these surface defects. As these isolated cracks propagated from different locations and planes, they coalesced and formed larger cracks, each of which propagated over smaller areas and reduced fatigue life. On the other hand, longer fatigue lives in DM and DM+P were attributed to the complete removal of surface and near-surface defects, which shifted crack initiation away from the surface to a single, small feature in the specimen's interior (see **Figure 37(e) & (f)**). Fractography of both DM and DM+P conditions showed crack initiation from the gas entrapped pores located ~280 µm beneath the surface. According to Murakami's $\sqrt{area}$ approach [126], the size of these internal defects was measured to be ~20 µm, which was roughly 7 times smaller than the size of crack initiating defects in SM+P specimens. It is well known that the stress intensity factor of surface exposed cracks is higher than that of an internal crack of the same size [79], making surface and near-surface defects more detrimental than internal ones. Moreover, the crack initiations from internal regions propagated in an inert setting nearly similar to a vacuum environment, which reduced the surface oxidation and slowed down the crack growth rate compared to surface-connected defects such as in the case of UT, P, and SM+P conditions [127,128]; thus, DM and DM+P showed improvement in fatigue life of over two orders of magnitude.

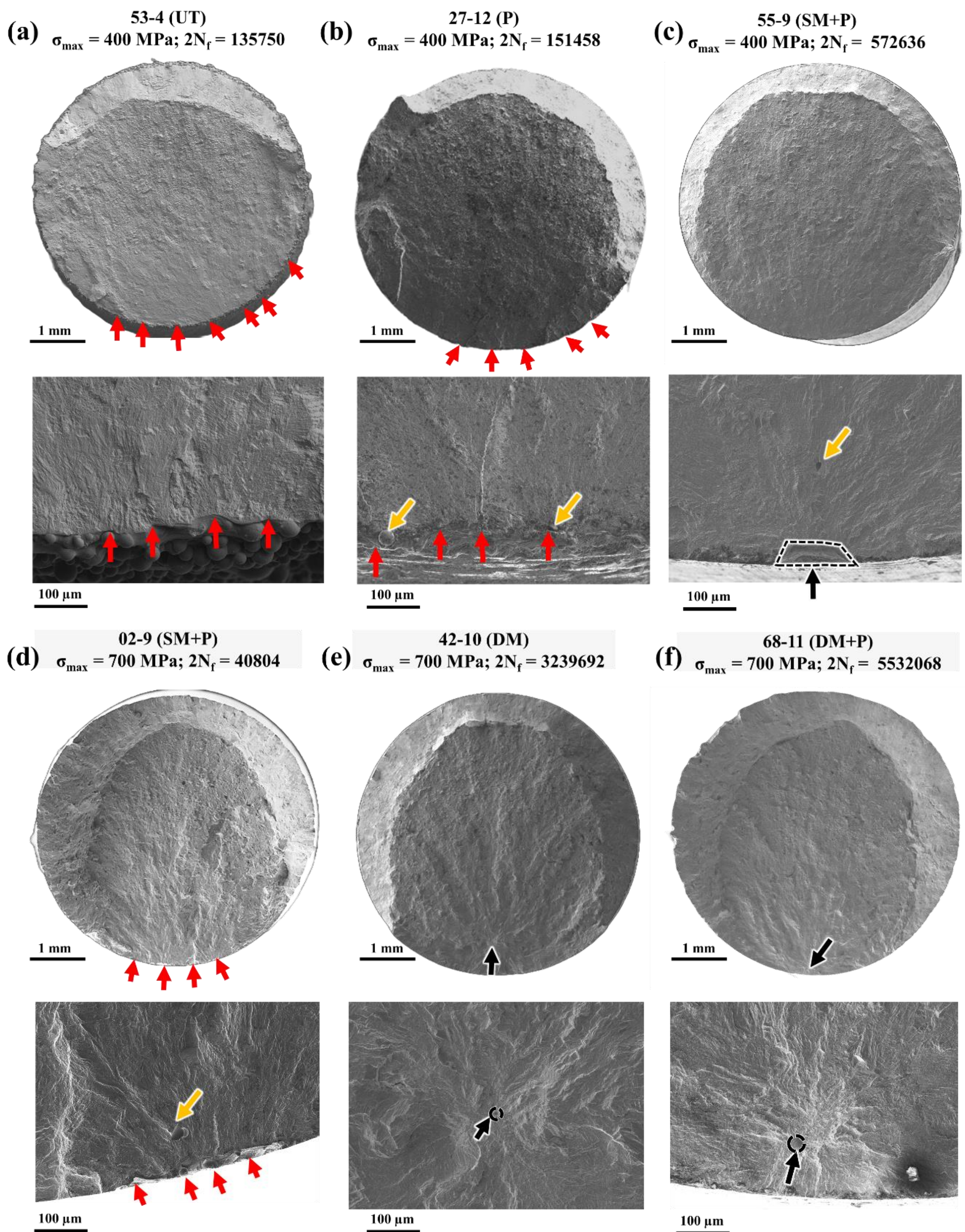

Figure 37 Fatigue fracture surfaces of specimens in various conditions: (a) UT, (b) P, (c) SM+P at maximum applied stress of 400 MPa; (d) SM+P, (e) DM, (f) DM+P at maximum applied stress of 700 MPa. Red and black arrows indicate surface micro-notches and volumetric defects respectively, while yellow arrows indicate near-surface volumetric defects.

4.4 Fatigue modelling

Treating the surface valleys as notches, the fatigue behavior of specimens in various conditions was modeled using the fatigue notch factor approach, as detailed in the authors' previous work [8]. In the approach, it was assumed that low cycle fatigue regime (LCF) (i.e., $<10^3$ cycles) is not significantly affected by the presence of surface notches due to profuse plastic deformation and dominance of crack propagation in fatigue life. However, towards the high cycle fatigue (HCF) regime, the crack initiation stage gradually dominates, and surface defects become more influential. Considering this, the fatigue notch factor approach applied in this study employed stress-life data of DM+P specimens as a reference, with the aim of predicting stress-life behavior of specimens with prominent surface roughness (i.e., UT, P, SM+P, and DM) by applying the knockdown, the fatigue notch factor, K_f, to the fatigue limit of DM+P specimens. The severity of these notches, K_f, can be quantified through Neuber's approach using the following formula:

$$K_f = 1 + \left[\frac{K_t - 1}{1 + \sqrt{\frac{\gamma}{\rho}}}\right], \qquad \text{Eq. (11)}$$

where K_t is an elastic stress concentration factor, ρ represents curvature radius of micro-notch, and γ is the material's characteristic length, which is typically the smallest microstructural unit. In this study, γ = 2.5 µm was used [8]. K_t was evaluated by treating notches as small elliptical holes in a plate using the Inglis's two parameter (depth, *d*, and width, *w*, of notch) formula:

$$K_{t1} = 1 + \frac{2d}{0.5w}. \qquad \text{Eq. (12)}$$

The notch parameters, d, w, and ρ, were evaluated using the algorithm from the authors' previous study [8]. The stress concentration factor, K_t, was evaluated for all surface micro-notches (comprising ~30,000 to 35,000 valleys) in the representative specimen from each condition, and then using the calculated K_t values, the corresponding fatigue notch factors, K_f, for all micro-notches were determined. Then, based on the approach presented in Ref. [8], the notch with the highest K_f value was chosen for fatigue modelling purposes. The average values of the surface parameters for each of the representative conditions along with the respective K_f values are listed in **Table 10**.

Table 10 Evaluated average notch radius, ρ, of representative specimens along with the corresponding averaged values of stress concentration factors, K_t and K_f values for each surface condition.

Conditions	$\boldsymbol{\rho}$	$\boldsymbol{K_t}$	$\boldsymbol{K_f}$
UT	24.24	4.70	3.80
P	31.22	3.67	3.08
SM+P	50.37	3.16	2.72
DM	641.82	1.62	1.17

To estimate the stress-life behavior for all conditions, first the fatigue strength at the LCF-HCF transition, corresponding to 2,000 reversals according to literature [19,20], was evaluated. Based on the ultimate tensile strength of L-PBF Ti-6Al-4V [11] and a suitable fatigue strength factor of f = 0.85 [74], the fatigue strength value was determined to be 1010 MPa. The experimental results indicated that the fatigue limit of reference specimens (i.e., DM+P), σ_e, at 10^7 reversals was 600 MPa (see **Figure 36**). The fatigue limit of each defective specimen, σ_e^D, across different conditions was then calculated by dividing the fatigue limit of the smooth specimen, σ_e, by the corresponding K_f value for each condition. Finally, the fatigue lives of the UT, P, and SM+P specimens were estimated by interpolating between the first point, the fatigue strengths at 2×10^3, and the corresponding σ_e^D for each specimen. The estimated fatigue strengths at 2×10^3 and 10^7

reversals in all surface conditions are presented in **Table 11**. In the case of DM, however, the cracks initiated predominantly from internal defects. This could be attributed to presence of compressive residual stress induced by machining, and the absence of any killer/critical surface defect. Therefore, the influence of the surface texture, if any, on the fatigue lives was assumed to be negligible, and the DM specimens were excluded from the fatigue modelling.

Table 11 The estimated fatigue strengths in all surface conditions at 10^7 reversals.

Surface conditions	**Estimated fatigue strengths (MPa) at 10^7 reversals**
UT	158
P	195
SM+P	221

The comparison between estimated and experimentally obtained fatigue lives of specimens across different conditions is shown in **Figure 38**. The red and black lines indicate the factors of 3 and 2, respectively. Excluding the runouts, for UT, 66% of predictions fell within the factor of 2, while 100% were within the factor of 3. In the case of P, 70% of the predictions were within a factor of 2, while all predictions (100%) fell within a factor of 3 excluding runouts. In the case of SM+P specimens, predictions were less accurate; specifically, 30% of predictions were within the factor of 2, while 60% fell within the factor of 3. Notably, the predicted fatigue lives were less than the experimental fatigue lives, indicating conservative predictions, which is typically desired in fatigue critical applications.

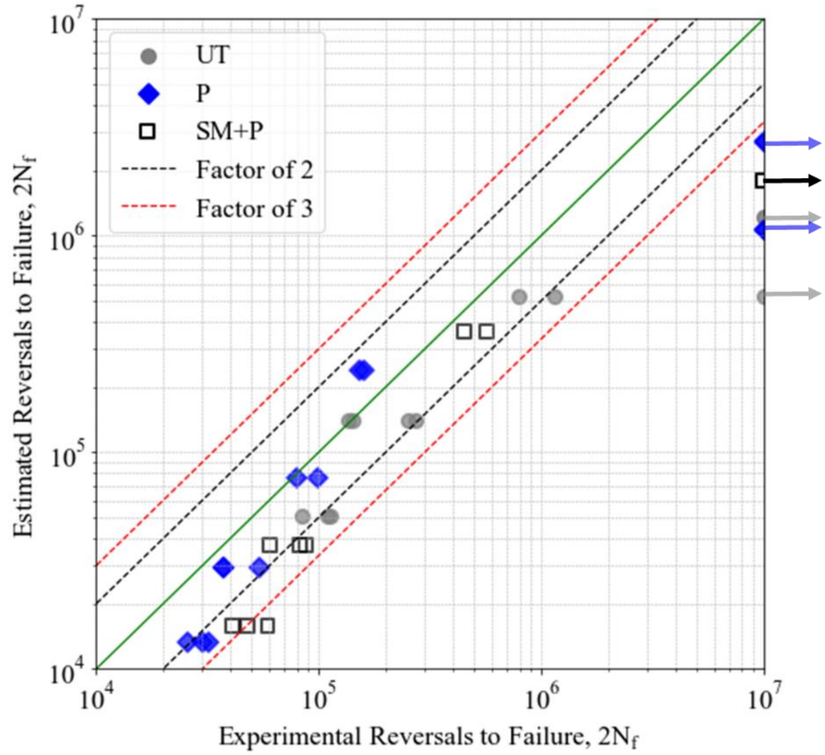

Figure 38 The predicted fatigue lives compared to experimental fatigue lives. The arrows indicate the runout specimens.

4.5 Conclusions

This study investigated the influence of four different material removal processes, which included direct polishing (P), shallow machining and polishing (SM+P), deep machining (DM), and deep machining and polishing (DM+P), on the tensile and fatigue behaviors of laser powder bed fused Ti-6Al-4V parts. X-ray computed tomography (XCT) was utilized to characterize these conditions, while scanning electron microscopy was employed to conduct fractography. In addition, the fatigue notch factor approach was applied to estimate the fatigue lives of specimens with prominent surface roughness. The following conclusions were drawn from this study:

1) The near-surface defects at the interface between contour and infill regions were not adequately removed in the P and SM+P conditions due to insufficient machining depths

of ~50 μm and 150 μm, respectively. Only the deeper machining of 1 mm in DM and DM+P effectively removed these defects.

2) The SM+P, DM, and DM+P specimens showed slightly higher ductility compared to untreated (UT) specimens due to adequate removal of as-fabricated surface roughness. The P specimens, on the other hand, still had remnant valleys that caused earlier crack initiation at the surface and resulted in similar fracture behavior to UT specimens and therefore similar ductility.
3) The DM and DM+P conditions significantly improved fatigue life by eliminating surface and subsurface defects, while SM+P showed modest improvements due to presence of surface-connected defects, which restricted its efficacy of surface post-processing. The P, however, showed no improvement at all due to the presence of surface micro-notches.

The fatigue notch factor approach, treating the surface roughness as micro-notches, could reasonably estimate the fatigue lives of UT, P, and SM+P specimens

5 Summary and Potential Future Work

The goal of this dissertation was to understand the influence of surface integrity on the tensile and fatigue behaviors of Ti-6Al-4V. This chapter provides an overall summary of each study presented in prior sections.

Chapter 2 presented a detailed investigation into the surface features that most significantly influence the fatigue behavior of unmachined L-PBF Ti-6Al-4V parts. This work combined XCT with classical stress concentration formulae to characterize and quantify micro-notches present on unmachined specimens. By leveraging XCT's ability to capture complex surface and subsurface features, including hidden valleys, a new method was introduced to extract key geometrical parameters of these notches, such as width, depth, opening angle, and radius of curvature. These parameters were then used to calculate fatigue stress concentration factors. It was found that the maximum valley depth, S_v, when measured with overhang method (i.e., looking from top towards the surface like optical profilometers) did not correlate strongly with fatigue life. However, upon excluding overhang structures (looking from inside towards the free surface), the correlation between S_v and fatigue performance improved noticeably. Moreover, the fatigue stress concentration factor, K_f, calculated using data from the captured geometrical features of micro-notches, was observed to be effective in identifying the crack-initiating surface features, where the crack initiating features tended to fall within top 1% of K_f values. A predictive framework following the notch factor approach, which employed the evaluated K_f, was shown to estimate fatigue lives with reasonable accuracy. All predicted fatigue lives fell within a scatter band of ±3 with respect to experimental data. This approach demonstrated potential for predicting fatigue behavior in unmachined components and were extended to lightly post-processed surfaces

(**Chapter 4**), provided that surface modifications do not substantially alter the microstructure or induce significant residual stresses.

Chapter 3 presented how various process parameters, specifically different infill and contour settings, influence the surface texture, near-surface condition, and subsequently, tensile and fatigue behaviors of L-PBF Ti-6Al-4V. Surface characterization was performed using the XCT, while SEM was employed to conduct fractography. The fatigue notch factor approach followed employed in Chapter 2 was used to further validate and to model the influence of surface texture on fatigue behavior. The results showed that overheated infill conditions showed a higher density of near-surface defects compared to underheated or EOS-recommended conditions. Amongst different process conditions, no-contour specimens had higher surface roughness than their counterparts with contour passes, except in overheated cases where near-surface defects persisted. Contour passes generally introduced directional roughness, where the surface texture was rougher on the side facing away from the gas due to preferential deposition of spatter particles. This trend, however, was less noticeable near the gas outlet. Tensile strength was relatively insensitive by process variations; elongation to failure, on the other hand, was slightly reduced in no-contour and specimens with overheated infill conditions due to rougher surfaces and larger population of near-surface defects, which promoted void nucleation. Contour passes improved fatigue life for default and underheated infill conditions, but its efficacy diminished in overheated conditions due to the combined effects of increased roughness and high near-surface defects.

In Chapter 4, the effects of four different surface material removal treatments including P, SM+P, DM, and DM+P on the tensile and fatigue behaviors of L-PBF Ti-6Al-4V parts were investigated. Surface and subsurface features of each condition were characterized using XCT, while SEM was employed for fractography. The results showed that SM+P, DM, and DM+P treatments yielded slightly improved ductility compared to UT specimens due to complete removal of as-fabricate surface characteristics. In contrast, P specimens still had remnant valleys that promoted early crack initiation, which resulted in similar tensile behavior to UT specimens. Fatigue life improved significantly for the DM and DM+P conditions due to the removal of both surface and subsurface defects, while SM+P slightly enhanced fatigue lives and was limited by remnant surface-connected defects. P did not yield any noticeable fatigue improvement due to the persistence of micro-notches. Fatigue lives of specimens with prominent roughness were then modelled using the approach described in Chapter 2 (i.e., incorporating localized geometrical features of micro-notch). It was demonstrated that the approach can reasonably predict fatigue lives of partially treated specimens.

In this dissertation, three main objectives were pursued through individual research studies presented in Chapters 2,3, and 4. The first objective was to identify the critical surface features affecting the fatigue behavior of unmachined L-PBF Ti-6Al-4V. It was hypothesized that XCT-based micro-notch quantification can better identify fatigue-critical surface features than traditional surface texture parameters. Moreover, it was hypothesized that fatigue life predictions incorporating localized geometrical features of micro-notches will be more accurate than those based on conventional surface texture parameters. The results supported these hypotheses: S_v showed poor correlation with fatigue life, while the fatigue notch factor, K_f, evaluated by combining micro-notch geometry (width, depth, opening angle, and radius of curvature) and the corresponding elastic stress concentration factor, K_t, could reasonably capture fatigue-critical features. Notably, the crack-initiating notches consistently fell within the top 1% of all notches ranked in terms of K_f. Furthermore, fatigue life predictions using fatigue notch approach, employing the evaluated K_f, showed better accuracy compared to S_v based approach.

The second objective investigated how combination of variations in infill and contour process parameters affect surface and near-surface conditions, and subsequently, mechanical performance of L-PBF Ti-6Al-4V. It was hypothesized that avoiding contour passes would deteriorate surface quality and reduce mechanical performance. Moreover, deviating from recommended infill conditions will exacerbate surface texture and reduce mechanical performance. The results obtained via XCT analyses and mechanical testing supported these hypotheses: no-contour specimens generally exhibited higher surface roughness than those with contour passes, except under overheated infill conditions where high population of subsurface defects reduced contouring efficacy. While strength did not change across all the process conditions, ductility was lower in no-contour specimens due to increased surface roughness promoting earlier void nucleation than specimens with contour. Overall, contour passes can improve fatigue life under default and underheated conditions. However, for overheated infill condition, no improvement in fatigue life was noticed due to the combined effects of increased roughness and a higher density of near-surface defects. Importantly, the fatigue life prediction based on the fatigue notch factor approach (described in Chapter 2) could adequately estimate fatigue lives across a wide range of process conditions. This validated the robustness of the framework developed in the first study.

The third objective examined the impact of surface texture modification through different material removal methods including P, SM+P, DM, and DM+P on the tensile and fatigue behaviors of L-PBF Ti-6Al-4V. It was hypothesized that P alone would not be sufficient to significantly improve mechanical performance. Moreover, fatigue life predictions using a notch factor approach that incorporates localized geometrical features of micro-notches can more accurately estimate fatigue lives of surface-treated specimens. Findings from the results validated these hypotheses. P specimens showed both similar ductility and fatigue life to UT ones. This was ascribed to the presence of remnant surface valleys and near-surface defects. SM+P specimens had tensile properties comparable to DM+P, but their fatigue performance was inferior, which could likely be due to residual surface-connected defects. In contrast, DM and DM+P treatments, which effectively removed both surface and subsurface defects, led to substantial improvements in fatigue life. The fatigue notch-based framework developed in Chapter 2 was also applied to specimens with prominent roughness, and it predicted fatigue lives with reasonable accuracy in conditions.

Overall, this dissertation provided a novel XCT-based NDE framework to identify the critical surface features influencing the fatigue behavior of L-PBF parts. Future work can include a wider range of material systems, stress ratios, environment, surface, and manufacturing conditions. This can facilitate with predicting fatigue behavior and designing more fatigue-resistant components for a wide range of applications. Moreover, advanced statistical techniques (e.g., Bayesian inference, regression analysis, and machine learning algorithms including support vector machines and neural networks) can be incorporated to model complex interactions among surface notch parameters and their effects on fatigue life. Future studies can also explore machine learning based segmentation and thresholding techniques (beyond the conventional Otsu method), especially those more suitable for detecting sharp surface features. Considering XCT's capability is limited by its resolution, future work can include probabilistic frameworks to infer critical surface features that may not be directly observable.

6 Supplemental Materials

S1: Thresholding Algorithms

Different thresholding algorithms, including Otsu, triangle-based, and minimum error, were evalauted for segmenting the surface from the scanned volume (see **Figure S1**). While Otsu's method is versatile and efficient, it tended to remove some sharp and deep valleys and near-surface defects, which could potentially initiate fatigue cracks. In contrast, the triangle-based thresholding method could somewhat capture sharp features and sub-surface defects, but introduced excessive noise, as indicated by the red arrows in **Figure S1(c)**. The minimum error thresholding method performed moderately, achieving a balance between Otsu's versatility and the triangle-based method's ability to identify surface feature. This made it the preferred threshold algoritham for the study.

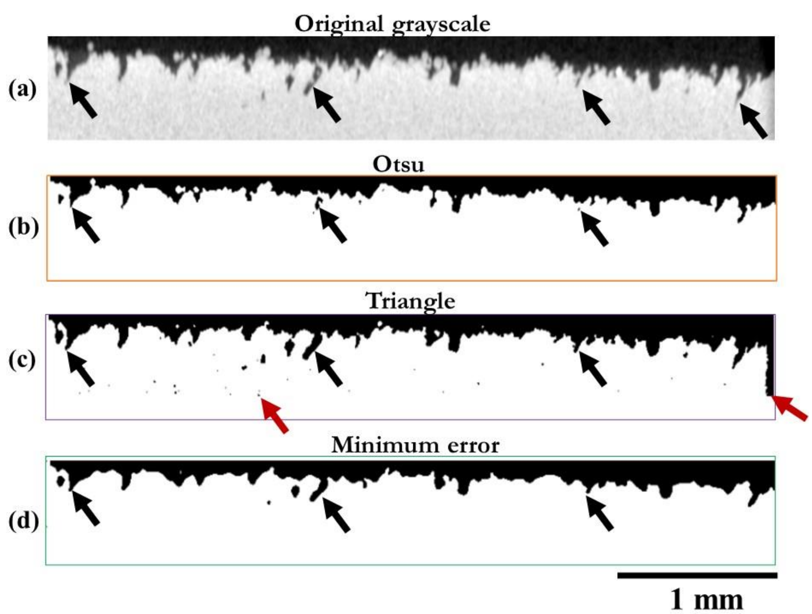

Figure S1 Application of different thresholding algorithms to the grayscale image: (a) original grayscale image, (b) Otsu, (c) triangle-based, and (d) minimum error thresholding. Black arrows highlight the same features in each image across the different thresholding methods, while red arrows indicate the noise.

S2: Capturing Micro-Notch Parameters

To fit an ellipse, first a piece-wise cubic spline was applied to the valley points to obtain a mathematical representation of the valley [92]. For a valley with *n* points, the function of spline is represented as:

$$f(x) = \begin{cases} P_1(x), & x_1 < x < x_2 \\ P_i(x), & x_i < x < x_{i+1} \\ P_n(x), & x_n < x < x_{n+1} \end{cases}, \qquad \text{(E1)}$$

where $P_i = A_i + B_i x + Cx^2 + D_i x^3$ and $A_i,\ B_i,\ C_i,\ D_i$ are to be determined for each i^{th} point.

Then, to determine the interval within which the ellipse was fitted, the closest inflection point was identified by calculating the spline's second derivative along the valley on both sides of the deepest point until the closest zero value (indicating an inflection point) was reached. The distance between the nearest inflection point and the deepest point defines the semi-width of the fitted interval. If no inflection point is found before reaching the valley's end, the distance between the nearest valley termination point and the deepest point is used instead. Then, the valley points within this neighborhood were normalized to account for scale variations. The normalization was done using the following relations [129]:

$$x_i = \frac{x_i' - \overline{x'}}{\sigma_{x'}}, \quad z_i = \frac{z_i' - \overline{z'}}{\sigma_{z'}}, \qquad \text{(E2)}$$

where x_i and z_i are the normalized while x_i' and z_i' are the original coordinates of the i^{th} point. $\overline{x'}$ and $\overline{z'}$ are the mean values, and $\sigma_{x'}$ and $\sigma_{z'}$ is the standard deviation of the original x and z coordinates of all points in the valley respectively.

After normalization, a circle was fitted to the points using an objective function (see **Eq. E3**) designed to minimize the deviation of all points from the boundary of circle. The circle was then transformed back to an ellipse in the original data scale.

$$\underset{c_x, c_z, r}{\operatorname{argmin}} \sum_{i=1}^{n} \left[\{(x_i - c_x)^2 + (z_i - c_z)^2\}^{\frac{1}{2}} - r \right]^2, \qquad \text{(E3)}$$

where c_x and c_z are the coordinates of the center, and r is the radius of the fitted circle. Minimizing this objective function using the normalized coordinates yields c_x, c_z and r. The visual representation of the fitted spline, its second derivative, and inflection points on normalized valley is shown in **Figure S2**.

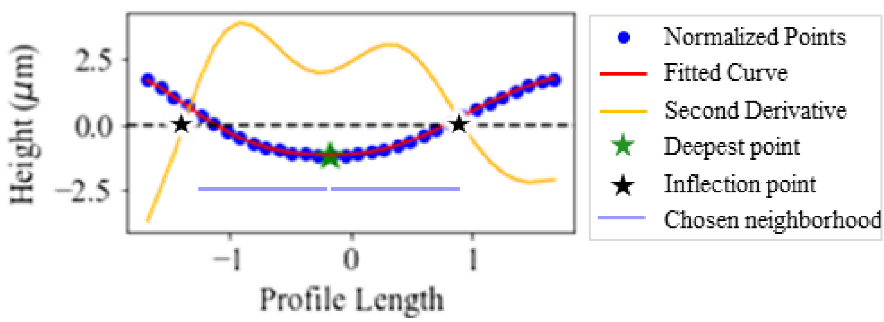

Figure S2 A visual representation of detailed steps adopted to obtain various notch parameters.

To find the opening angle, α_1, the first derivative of the spline is calculated along the valley on both sides of the deepest point. The process continues until the first derivative equals zero or a maximum is reached. These identified points represent the walls on both sides of the deepest point. A linear regression line is then fitted separately for both walls:

$$z_i = \beta_0 + \beta_1 \times x_i , \qquad \text{(E4)}$$

where β_0 is the intercept and β_1 is the slope of the fitted line. After the slopes were calculated from both sides, the respective angles (α_1 and α_2) were determined using relation: $\alpha = \tan^{-1} \beta_1$. These angles were then used to find the angle between the walls of the valley as:

$$\theta = 180° - (\alpha_1 + \alpha_2). \quad \text{(E5)}$$

S3: Critical Surface Features

To further investigate the critical surface features and associated fatigue stress concentration factors (K_f), the crack initiating defects in the scanned volumes of four specimens were analyzed. This includes those shown in **Figures 9(g)-(i)** and **11(a)-(c)** in the main text, and **Figure S3**. The crack initiating defects in **Figure S3** were identified by scanning the specimens before and after testing, and these were then correlated with the fractography data. Once the crack initiating defects in the scanned volume of the untested specimens were identified, K_f for the entire scanned surface was calculated. A probability density function (PDF) was then plotted (see **Figure S4**) for all surface valleys using the K_{f1} formula (see **Eq.1** in the main text). The resulting PDF exhibited a long tail, indicative of sharp features that could potentially initiate fatigue cracks. To validate, the K_{f1} of the crack initiating valley is marked on the PDF plot. Notice that all the identified crack initiation defects were found within this tail region, falling within the top 1% of the distribution.

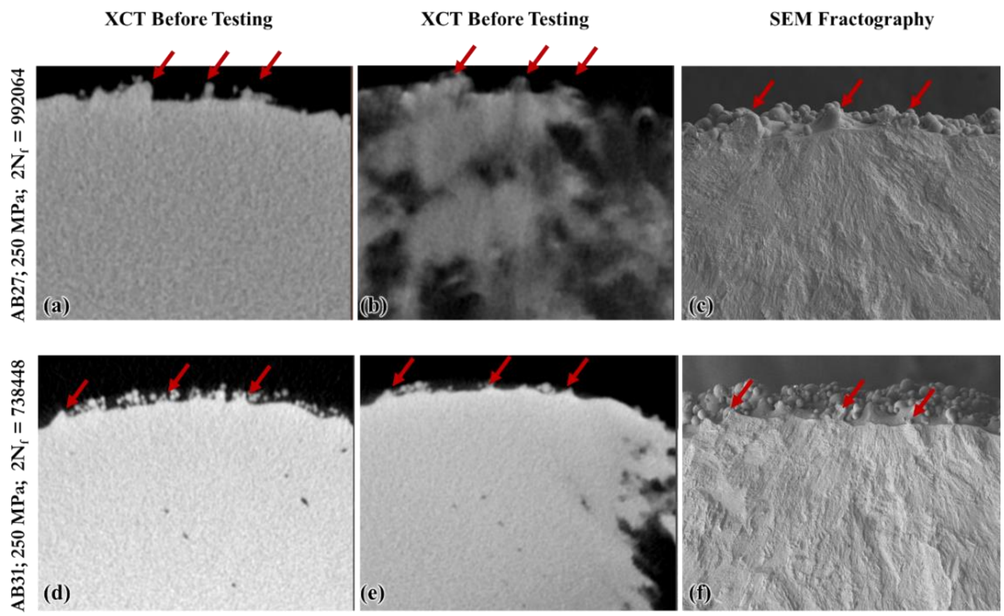

Figure S3 Identification of crack initiating defects in the 3D scanned volume: XCT slice views of the crack initiation site (a) & (d) before, and (b) & (e) after fatigue testing. Fractography in (c) and (f) confirms the corresponding crack initiation locations. Red arrows point at the matching features in both XCT slices and fractographs.

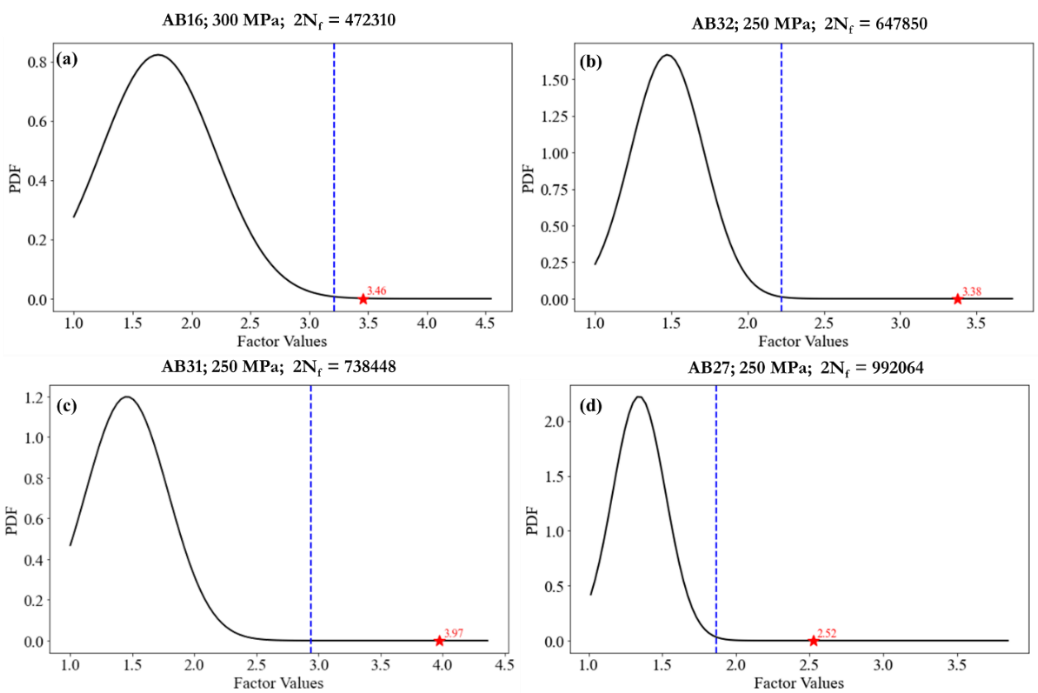

Figure S4 PDF plots showing the distribution of K_{f1} values for specimens tested at different maximum applied stresses: (a) 300 MPa, (b)-(d) 250 MPa. The red star marks the K_{f1} value at the crack initiation site, while the blue vertical line indicates the 99th percentile of K_{f1} values.

S4: Stress-Life Results of Machined & Polished Specimens

The fatigue testing was performed at maximum applied stresses of 850, 800, 700, and 600 MPa. All specimens tested at 600 MPa exhibited lives exceeding 10^7 reversals and were classified as runouts (see **Figure S5**).

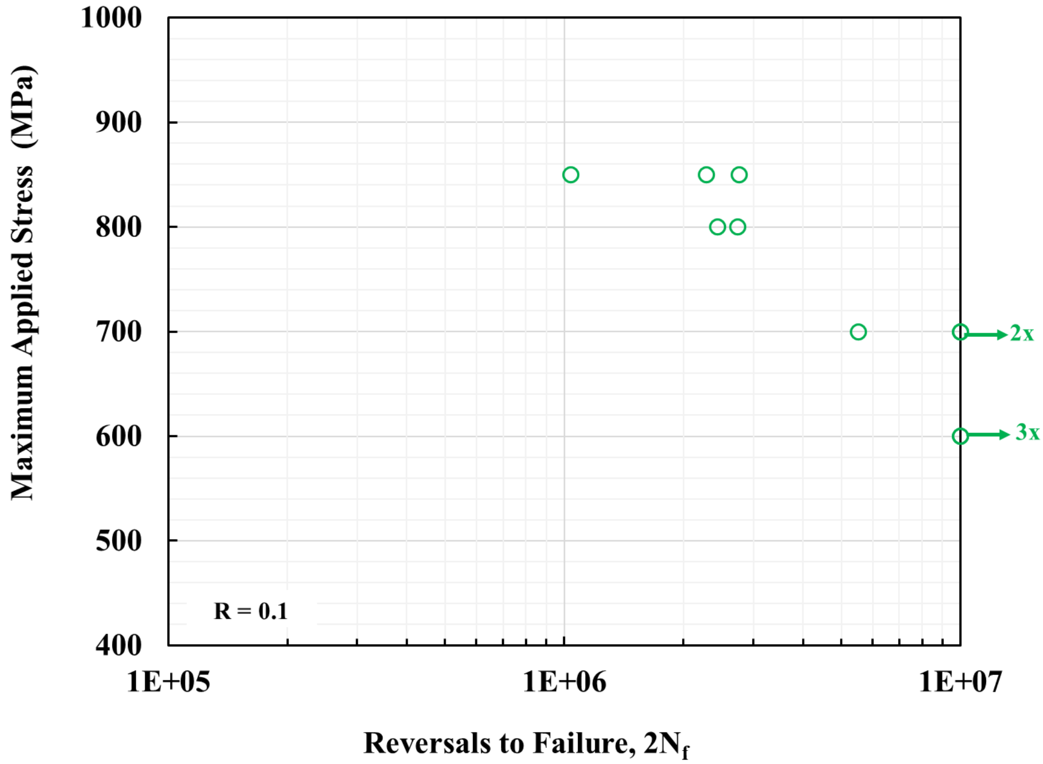

Figure S5 Stress-life results of machined and polished specimens.

7 References

[1] Yadollahi A, Shamsaei N. Additive manufacturing of fatigue resistant materials: Challenges and opportunities. Int J Fatigue 2017;98:14–31. https://doi.org/10.1016/j.ijfatigue.2017.01.001.

[2] Mostafaei A, Zhao C, He Y, Reza Ghiaasiaan S, Shi B, Shao S, et al. Defects and anomalies in powder bed fusion metal additive manufacturing. Curr Opin Solid State Mater Sci 2022;26:100974. https://doi.org/10.1016/j.cossms.2021.100974.

[3] Schmelzle J, Kline E V., Dickman CJ, Reutzel EW, Jones G, Simpson TW. (Re)Designing for Part Consolidation: Understanding the Challenges of Metal Additive Manufacturing. J Mech Des 2015;137:111404. https://doi.org/10.1115/1.4031156.

[4] Davies S. A flying start: GE Aerospace's additive manufacturing journey n.d. https://www.tctmagazine.com/additive-manufacturing-3d-printing-industry-insights/aerospace-insights/ge-aerospace-additive-manufacturing-journey/.

[5] Cramer E. Soldier feedback helps shape future 3-D printing system for enhanced readiness 2020. https://www.army.mil/article/232945/soldier_feedback_helps_shape_future_3_d_printing_system_for_enhanced_readiness.

[6] DebRoy T, Wei HL, Zuback JS, Mukherjee T, Elmer JW, Milewski JO, et al. Additive manufacturing of metallic components – Process, structure and properties. Prog Mater Sci 2018;92:112–224. https://doi.org/10.1016/j.pmatsci.2017.10.001.

[7] Poudel A, Yasin MS, Ye J, Liu J, Vinel A, Shao S, et al. Feature-based volumetric defect classification in metal additive manufacturing. Nat Commun 2022;13:6369.

https://doi.org/10.1038/s41467-022-34122-x.

[8] Ahmad N, Irfan S, Maleki E, Lee S, Liu JP, Shao S, et al. Determining critical surface features affecting fatigue behavior of additively manufactured Ti-6Al-4V. Int J Fatigue 2025;197. https://doi.org/10.1016/j.ijfatigue.2025.108956.

[9] Pegues J, Roach M, Scott Williamson R, Shamsaei N. Surface roughness effects on the fatigue strength of additively manufactured Ti-6Al-4V. Int J Fatigue 2018;116:543–52. https://doi.org/10.1016/j.ijfatigue.2018.07.013.

[10] Tammas-Williams S, Withers PJ, Todd I, Prangnell PB. Porosity regrowth during heat treatment of hot isostatically pressed additively manufactured titanium components. Scr Mater 2016;122:72–6. https://doi.org/10.1016/j.scriptamat.2016.05.002.

[11] Soltani-Tehrani A, Isaac JP, Tippur H V., Silva DF, Shao S, Shamsaei N. Ti-6Al-4V powder reuse in laser powder bed fusion (L-PBF): The effect on porosity, microstructure, and mechanical behavior. Int J Fatigue 2023;167:107343. https://doi.org/10.1016/j.ijfatigue.2022.107343.

[12] Pramanik A, Littlefair G. Machining of titanium alloy (Ti-6Al-4V)-theory to application. Mach Sci Technol 2015;19:1–49. https://doi.org/10.1080/10910344.2014.991031.

[13] Blakey-Milner B, Gradl P, Snedden G, Brooks M, Pitot J, Lopez E, et al. Metal additive manufacturing in aerospace: A review. Mater Des 2021;209:110008. https://doi.org/10.1016/j.matdes.2021.110008.

[14] ISO 25178-2:2021. Geometrical product specifications (GPS) — Surface texture: Areal 2021.

[15] Gockel J, Sheridan L, Koerper B, Whip B. The influence of additive manufacturing processing parameters on surface roughness and fatigue life. Int J Fatigue 2019;124:380–8. https://doi.org/10.1016/j.ijfatigue.2019.03.025.

[16] Lee S, Shao S, Wells DN, Zetek M, Kepka M, Shamsaei N. Fatigue behavior and modeling of additively manufactured IN718: The effect of surface treatments and surface measurement techniques. J Mater Process Technol 2022;302:117475. https://doi.org/10.1016/j.jmatprotec.2021.117475.

[17] Novovic D, Dewes RC, Aspinwall DK, Voice W, Bowen P. The effect of machined topography and integrity on fatigue life. Int J Mach Tools Manuf 2004;44:125–34. https://doi.org/10.1016/j.ijmachtools.2003.10.018.

[18] Arola D, Williams CL. Estimating the fatigue stress concentration factor of machined surfaces. Int J Fatigue 2002;24:923–30. https://doi.org/10.1016/S0142-1123(02)00012-9.

[19] Lee S, Pegues JW, Shamsaei N. Fatigue behavior and modeling for additive manufactured 304L stainless steel: The effect of surface roughness. Int J Fatigue 2020;141:Under Review. https://doi.org/10.1016/j.ijfatigue.2020.105856.

[20] Lee S, Rasoolian B, Silva DF, Pegues JW, Shamsaei N. Surface roughness parameter and modeling for fatigue behavior of additive manufactured parts: A non-destructive data-driven approach. Addit Manuf 2021;46:102094. https://doi.org/10.1016/j.addma.2021.102094.

[21] Witkin DB, Patel D, Albright T V., Bean GE, McLouth T. Influence of surface conditions and specimen orientation on high cycle fatigue properties of Inconel 718 prepared by laser powder bed fusion. Int J Fatigue 2020;132:105392.

https://doi.org/10.1016/j.ijfatigue.2019.105392.

[22] Kantzos CA, Cunningham RW, Tari V, Rollett AD. Characterization of metal additive manufacturing surfaces using synchrotron X-ray CT and micromechanical modeling. Comput Mech 2018;61:575–80. https://doi.org/10.1007/s00466-017-1531-z.

[23] N. N. Standardization Roadmap for Additive Manufacturing - Version 2.0. vol. 2. 2018.

[24] Yadollahi A, Shamsaei N, Thompson SM, Seely DW. Effects of process time interval and heat treatment on the mechanical and microstructural properties of direct laser deposited 316L stainless steel. Mater Sci Eng A 2015;644:171–83. https://doi.org/10.1016/j.msea.2015.07.056.

[25] Soltani-Tehrani A, Shrestha R, Phan N, Seifi M, Shamsaei N. Establishing specimen property to part performance relationships for laser beam powder bed fusion additive manufacturing. Int J Fatigue 2021;151:106384. https://doi.org/10.1016/j.ijfatigue.2021.106384.

[26] McConnell S, Gaber Y, Kourousis KI, Tanner D. Increasing productivity for Laser Powder Bed Fusion of Ti-6Al-4V parts through increased layer heights. Prog Addit Manuf 2024:1–19.

[27] Metallic Materials Properties Development and Standardization (MMPDS) n.d. https://www.mmpds.org/.

[28] Hamidi Nasab M, Romano S, Gastaldi D, Beretta S, Vedani M. Combined effect of surface anomalies and volumetric defects on fatigue assessment of AlSi7Mg fabricated via laser powder bed fusion. Addit Manuf 2020;34:100918.

https://doi.org/10.1016/j.addma.2019.100918.

[29] Beretta S, Romano S. A comparison of fatigue strength sensitivity to defects for materials manufactured by AM or traditional processes. Int J Fatigue 2017;94:178–91. https://doi.org/10.1016/j.ijfatigue.2016.06.020.

[30] Romano S, Brandão A, Gumpinger J, Gschweitl M, Beretta S. Qualification of AM parts: Extreme value statistics applied to tomographic measurements. Mater Des 2017;131:32–48. https://doi.org/10.1016/j.matdes.2017.05.091.

[31] Molaei R, Fatemi A, Sanaei N, Pegues J, Shamsaei N, Shao S, et al. Fatigue of additive manufactured Ti-6Al-4V, Part II: The relationship between microstructure, material cyclic properties, and component performance. Int J Fatigue 2020;132:105363. https://doi.org/10.1016/j.ijfatigue.2019.105363.

[32] Ahmad N, Shao S, Seifi M, Shamsaei N. Additively manufactured IN718 in thin wall and narrow flow channel geometries: Effects of post-processing and wall thickness on tensile and fatigue behaviors. Addit Manuf 2022;60:103264. https://doi.org/10.1016/j.addma.2022.103264.

[33] Maleki E, Bagherifard S, Bandini M, Guagliano M. Surface post-treatments for metal additive manufacturing: Progress, challenges, and opportunities. Addit Manuf 2021;37:101619. https://doi.org/10.1016/j.addma.2020.101619.

[34] Morgan K, Wells D. Overview of Fatigue and Damage Tolerance Performance of SLM Alloy 718. 2016.

[35] Maleki E, Shamsaei N. A comprehensive study on the effects of surface post-processing on

fatigue performance of additively manufactured AlSi10Mg: An augmented machine learning perspective on experimental observations. Addit Manuf 2024;86:104179. https://doi.org/10.1016/j.addma.2024.104179.

[36] Chen LY, Liang SX, Liu Y, Zhang LC. Additive manufacturing of metallic lattice structures: Unconstrained design, accurate fabrication, fascinated performances, and challenges. Mater Sci Eng R Reports 2021;146:100648. https://doi.org/10.1016/j.mser.2021.100648.

[37] Malakizadi A, Mallipeddi D, Dadbakhsh S, M'Saoubi R, Krajnik P. Post-processing of additively manufactured metallic alloys – A review. Int J Mach Tools Manuf 2022;179:103908. https://doi.org/10.1016/j.ijmachtools.2022.103908.

[38] Oliveira JFG, Silva EJ, Guo C, Hashimoto F. Industrial challenges in grinding. CIRP Ann - Manuf Technol 2009;58:663–80. https://doi.org/10.1016/j.cirp.2009.09.006.

[39] Rhoades L. Abrasive flow machining: a case study. J Mater Process Tech 1991;28:107–16. https://doi.org/10.1016/0924-0136(91)90210-6.

[40] Gradl P, Cervone A, Colonna P. Development and experimental evaluation of surface enhancement methods for laser powder directed energy deposition microchannels. Virtual Phys Prototyp 2024;19. https://doi.org/10.1080/17452759.2024.2345389.

[41] Pegues JW, Shao S, Shamsaei N, Sanaei N, Fatemi A, Warner DH, et al. Fatigue of additive manufactured Ti-6Al-4V, Part I: The effects of powder feedstock, manufacturing, and post-process conditions on the resulting microstructure and defects. Int J Fatigue 2020;132:105358. https://doi.org/10.1016/j.ijfatigue.2019.105358.

[42] du Plessis A, Beretta S. Killer notches: The effect of as-built surface roughness on fatigue failure in AlSi10Mg produced by laser powder bed fusion. Addit Manuf 2020;35:101424. https://doi.org/10.1016/j.addma.2020.101424.

[43] Macek W, Masoudi Nejad R, Zhu SP, Trembacz J, Branco R, Costa JDM, et al. Effect of bending-torsion on fracture and fatigue life for 18Ni300 steel specimens produced by SLM. Mech Mater 2023;178:104576. https://doi.org/10.1016/j.mechmat.2023.104576.

[44] Macek W, Branco R, Podulka P, Kopec M, Zhu SP, Domingos Costa J. A brief note on entire fracture surface topography parameters for 18Ni300 maraging steel produced by LB-PBF after LCF. Eng Fail Anal 2023;153:107541. https://doi.org/10.1016/j.engfailanal.2023.107541.

[45] Kobayashi T, Shockey DA. Fracture surface topography analysis (FRASTA)-Development, accomplishments, and future applications. Eng Fract Mech 2010;77:2370–84. https://doi.org/10.1016/j.engfracmech.2010.05.016.

[46] Camacho J, Martins RF, Branco R, Raimundo A, Malça C. The influence of printing strategies on fatigue crack growth behavior of an additively manufactured AISI 316L stainless steel. Fatigue Fract Eng Mater Struct 2023;46:3953–65. https://doi.org/10.1111/ffe.14112.

[47] Barricelli L, Patriarca L, du Plessis A, Beretta S. A comparison of fatigue analysis methods for L-PBF net-shape surfaces in Ti6Al4V parts. Theor Appl Fract Mech 2023;128:104143. https://doi.org/10.1016/j.tafmec.2023.104143.

[48] Barricelli L, Patriarca L, du Plessis A, Beretta S. Orientation-dependent fatigue assessment of Ti6Al4V manufactured by L-PBF: Size of surface features and shielding effect. Int J

Fatigue 2023;168:107401. https://doi.org/10.1016/j.ijfatigue.2022.107401.

[49] Tardi D, Gli Y, Chan KHK, Blunt L, Bache MR. Surface topography and the impact on fatigue performance. Surf Topogr Metrol Prop 2015;3. https://doi.org/10.1088/2051-672X/3/1/015007.

[50] Whip B, Sheridan L, Gockel J. The effect of primary processing parameters on surface roughness in laser powder bed additive manufacturing. Int J Adv Manuf Technol 2019;103:4411–22. https://doi.org/10.1007/s00170-019-03716-z.

[51] Kafka OL, Benzing J, Derimow N, Schumacher P, Koepke L, Beamer C, et al. Effects of as-built surface with varying number of contour passes on high-cycle fatigue behavior of additively manufactured nickel alloy 718. Int J Fatigue 2023;176:107872. https://doi.org/10.1016/j.ijfatigue.2023.107872.

[52] Yadollahi A, Mahtabi MJ, Khalili A, Doude HR, Newman JC. Fatigue life prediction of additively manufactured material: Effects of surface roughness, defect size, and shape. Fatigue Fract Eng Mater Struct 2018;41:1602–14. https://doi.org/10.1111/ffe.12799.

[53] Maleki E, Bagherifard S, Ahmad N, Shao S, Unal O, Guagliano M, et al. Fatigue performance of U-notched additively manufactured AlSi10Mg parts: The effects of chemical and thermal post-treatments. Addit Manuf Lett 2023;7:100175. https://doi.org/10.1016/j.addlet.2023.100175.

[54] Pegues JW, Shamsaei N, Roach MD, Williamson RS. Fatigue life estimation of additive manufactured parts in the as-built surface condition. Mater Des Process Commun 2019;1:e36. https://doi.org/10.1002/mdp2.36.

[55] Townsend A, Senin N, Blunt L, Leach RK, Taylor JS. Surface texture metrology for metal additive manufacturing: a review. Precis Eng 2016;46:34–47. https://doi.org/10.1016/j.precisioneng.2016.06.001.

[56] Lou S, Jiang X, Sun W, Zeng W, Pagani L, Scott PJ. Characterisation methods for powder bed fusion processed surface topography. Precis Eng 2019;57:1–15. https://doi.org/10.1016/j.precisioneng.2018.09.007.

[57] Inglis CE. Stress in a plate due to the presence of cracks and sharp corners. Spring Meet Fifty-Fourth Sess Inst Nav Archit 1913;55:219–41.

[58] ASTM. Standard Practice for Conducting Force Controlled Constant Amplitude Axial Fatigue Tests of Metallic Materials. vol. 03. 2002. https://doi.org/10.1520/E0466-21.2.

[59] Kittler J, Illingworth J. Minimum error thresholding. Pattern Recognit 1986;19:41–7. https://doi.org/10.1016/0031-3203(86)90030-0.

[60] Steinhilber F, Lachambre J, Coeurjolly D, Buffiere JY, Martin G, Dendievel R. A methodology for the 3D characterization of surfaces using X-ray computed tomography: Application to additively manufactured parts. Addit Manuf 2024;84:104144. https://doi.org/10.1016/j.addma.2024.104144.

[61] Zack GW, Rogers WE, Latt SA. Automatic measurement of sister chromatid exchange frequency. J Histochem Cytochem 1977;25:741–53. https://doi.org/10.1177/25.7.70454.

[62] Alves IF, Neves C. Extreme Value Distributions. 2011. https://doi.org/10.1007/978-3-642-04898-2_246.

[63] Romano S, Nezhadfar PD, Shamsaei N, Seifi M, Beretta S. High cycle fatigue behavior and

life prediction for additively manufactured 17-4 PH stainless steel: Effect of sub-surface porosity and surface roughness. Theor Appl Fract Mech 2020;106:102477. https://doi.org/10.1016/j.tafmec.2020.102477.

[64] Ahmad N, Ghiaasiaan R, Gradl PR, Shao S, Shamsaei N. Low cycle fatigue behavior of additively manufactured Haynes 282: Effect of post-processing and test temperature. Int J Fatigue 2023;176:107880. https://doi.org/10.1016/j.ijfatigue.2023.107880.

[65] Fuchs HO, Stephens RI, Saunders H. Metal Fatigue in Engineering (1980). vol. 103. 2nd ed. Second edition. New York : Wiley, [2001] ©2001; 1981. https://doi.org/10.1115/1.3225026.

[66] Fuchs HO, Stephens RI, Saunders H. Metal Fatigue in Engineering (1980). vol. 103. 1981. https://doi.org/10.1115/1.3225026.

[67] Ahmad N, Ghiaasiaan R, Gradl PR, Shao S, Shamsaei N. Low cycle fatigue behavior of additively manufactured Haynes 282: Effect of post-processing and test temperature. vol. 176. 2023. https://doi.org/10.1016/j.ijfatigue.2023.107880.

[68] Neuber H. Theory of stress concentration for shear-strained prismatical bodies with arbitrary nonlinear stress-strain law. J Appl Mech Trans ASME 1960;28:544–50. https://doi.org/10.1115/1.3641780.

[69] Hosford WF. Mechanical behavior of materials. vol. 9780521846. Second. Cambridge University Press; 2005. https://doi.org/10.1017/CBO9780511810930.

[70] Tada H, Paris PC, Irwin GR. The Stress Analysis of Cracks Handbook, Third Edition. 3rd ed. ASME Press; 2010. https://doi.org/10.1115/1.801535.

[71] Noda NA, Takase Y. Stress concentration formula useful for all notch shape in a round bar (comparison between torsion, tension and bending). Int J Fatigue 2006;28:151–63. https://doi.org/10.1016/j.ijfatigue.2005.04.015.

[72] Calignano F. Investigation of the accuracy and roughness in the laser powder bed fusion process. Virtual Phys Prototyp 2018;13:97–104. https://doi.org/10.1080/17452759.2018.1426368.

[73] Shao S, Poudel A, Shamsaei N. A linear elastic finite element approach to fatigue life estimation for defect laden materials. Eng Fract Mech 2023;285:109298. https://doi.org/10.1016/j.engfracmech.2023.109298.

[74] Budynas-Nisbett. Mechanical Engineering : Shigley's Mechanical Engineering Design. vol. 01. McGRAW-HILL SERIES; 2006.

[75] You JH, Park K. Design and additive manufacturing of thermal metamaterial with high thermal resistance and cooling capability. Addit Manuf 2021;41:101947. https://doi.org/10.1016/j.addma.2021.101947.

[76] Aiza I, Baldi C, de la Vega FM, Sebastiani S, Veronese NE, Yousefi M, et al. Effects of build orientation and inclined features on physical, microstructural and mechanical properties of powder bed fusion additively manufactured metallic parts. Prog Mater Sci 2025;147:101357. https://doi.org/10.1016/j.pmatsci.2024.101357.

[77] Gradl P, Tinker DC, Park A, Mireles OR, Garcia M, Wilkerson R, et al. Robust Metal Additive Manufacturing Process Selection and Development for Aerospace Components. J Mater Eng Perform 2022;31:6013–44. https://doi.org/10.1007/s11665-022-06850-0.

[78] Vasco JC. Additive manufacturing for the automotive industry. Addit. Manuf., Elsevier; 2021, p. 505–30. https://doi.org/10.1016/B978-0-12-818411-0.00010-0.

[79] Masuo H, Tanaka Y, Morokoshi S, Yagura H, Uchida T, Yamamoto Y, et al. Influence of defects, surface roughness and HIP on the fatigue strength of Ti-6Al-4V manufactured by additive manufacturing. Int J Fatigue 2018;117:163–79. https://doi.org/10.1016/j.ijfatigue.2018.07.020.

[80] Dilip JJS, Zhang S, Teng C, Zeng K, Robinson C, Pal D, et al. Influence of processing parameters on the evolution of melt pool, porosity, and microstructures in Ti-6Al-4V alloy parts fabricated by selective laser melting. Prog Addit Manuf 2017;2:157–67. https://doi.org/10.1007/s40964-017-0030-2.

[81] Shrestha R, Shamsaei N, Seifi M, Phan N. An investigation into specimen property to part performance relationships for laser beam powder bed fusion additive manufacturing. Addit Manuf 2019;29. https://doi.org/10.1016/j.addma.2019.100807.

[82] Klingaa CG, Zanini F, Mohanty S, Carmignato S, Hattel JH. Characterization of geometry and surface texture of alsi10mg laser powder bed fusion channels using x-ray computed tomography. Appl Sci 2021;11:4304. https://doi.org/10.3390/app11094304.

[83] Yu CH, Peng RL, Luzin V, Sprengel M, Calmunger M, Lundgren JE, et al. Thin-wall effects and anisotropic deformation mechanisms of an additively manufactured Ni-based superalloy. Addit Manuf 2020;36:101672. https://doi.org/10.1016/j.addma.2020.101672.

[84] Wan HY, Luo YW, Zhang B, Song ZM, Wang LY, Zhou ZJ, et al. Effects of surface roughness and build thickness on fatigue properties of selective laser melted Inconel 718 at 650 °C. Int J Fatigue 2020;137:105654. https://doi.org/10.1016/j.ijfatigue.2020.105654.

[85] Ma M, Wang Z, Gao M, Zeng X. Layer thickness dependence of performance in high-power selective laser melting of 1Cr18Ni9Ti stainless steel. J Mater Process Technol 2015;215:142–50. https://doi.org/10.1016/j.jmatprotec.2014.07.034.

[86] Shi X, Ma S, Liu C, Chen C, Wu Q, Chen X, et al. Performance of high layer thickness in selective laser melting of Ti6Al4V. Materials (Basel) 2016;9:975. https://doi.org/10.3390/ma9120975.

[87] Mallipeddi D, Hajali T, Rännar LE, Bergström A, Hernandez S, Strandh E, et al. Surface Integrity of Machined Electron Beam Melted Ti6Al4V Alloy Manufactured with Different Contour Settings and Heat Treatment. Procedia CIRP 2020;87:327–32. https://doi.org/10.1016/j.procir.2020.02.091.

[88] Artzt K, Mishurova T, Bauer PP, Gussone J, Barriobero-Vila P, Evsevleev S, et al. Pandora's box-influence of contour parameters on roughness and subsurface residual stresses in laser powder bed fusion of Ti-6Al-4V. Materials (Basel) 2020;13:3348. https://doi.org/10.3390/ma13153348.

[89] Buchenau T, Amkreutz M, Bruening H, Mayer B. Influence of Contour Scan Variation on Surface, Bulk and Mechanical Properties of LPBF-Processed AlSi7Mg0.6. Materials (Basel) 2023;16:3169. https://doi.org/10.3390/ma16083169.

[90] Mu J, Sun T, Leung CLA, Oliveira JP, Wu Y, Wang H, et al. Application of electrochemical polishing in surface treatment of additively manufactured structures: A review. Prog Mater Sci 2023;136. https://doi.org/10.1016/j.pmatsci.2023.101109.

[91] ASTM Standard E8/E8M-13a. "Standard Test Methods for Tension Testing of Metallic Materials." ASTM International; 2013.

[92] Virtanen P, Gommers R, Oliphant TE, Haberland M, Reddy T, Cournapeau D, et al. SciPy 1.0: fundamental algorithms for scientific computing in Python. Nat Methods 2020;17:261–72.

[93] Piette TD, Spangenberger AG, Stoner BE, Lados DA. Influence of contour processing parameters on porosity, surface roughness, and fatigue life in laser powder bed Al-10Si-0.4Mg. J Manuf Process 2024;118:419–31. https://doi.org/10.1016/j.jmapro.2024.03.047.

[94] Andreau O, Pessard E, Koutiri I, Penot JD, Dupuy C, Saintier N, et al. A competition between the contour and hatching zones on the high cycle fatigue behaviour of a 316L stainless steel: Analyzed using X-ray computed tomography. Mater Sci Eng A 2019;757:146–59. https://doi.org/10.1016/j.msea.2019.04.101.

[95] Kim FH, Yeung H, Garboczi EJ. Characterizing the effects of laser control in laser powder bed fusion on near-surface pore formation via combined analysis of in-situ melt pool monitoring and X-ray computed tomography☆. Addit Manuf 2021;48:102372. https://doi.org/10.1016/j.addma.2021.102372.

[96] Ali U, Esmaeilizadeh R, Ahmed F, Sarker D, Muhammad W, Keshavarzkermani A, et al. Identification and characterization of spatter particles and their effect on surface roughness, density and mechanical response of 17-4 PH stainless steel laser powder-bed fusion parts. Mater Sci Eng A 2019;756:98–107. https://doi.org/10.1016/j.msea.2019.04.026.

[97] Donaldson B. What Effect Does Gas Flow Have in Metal Additive Manufacturing? Addit Manuf 2018.

[98] Carrion PE, Sausto F, Beretta S, Shamsaei N. Multiaxial fatigue behavior and modelling of additive manufactured Ti-6Al-4V parts: The effects of layer orientation and surface texture.

Int J Fatigue 2023;176:107860. https://doi.org/10.1016/j.ijfatigue.2023.107860.

[99] Anwar A Bin, Ibrahim IH, Pham QC. Spatter transport by inert gas flow in selective laser melting: A simulation study. Powder Technol 2019;352:103–16. https://doi.org/10.1016/j.powtec.2019.04.044.

[100] Weaver JS, Deisenroth DC, Moylan SP. Inert Gas Flow Speed Measurements in Laser Powder Bed Fusion Additive Manufacturing NIST Advanced Manufacturing Series 100-43 Inert Gas Flow Speed Measurements in Laser Powder Bed Fusion Additive Manufacturing. US Department of Commerce, National Institute of Standards and Technology; 2021.

[101] Esmaeilizadeh R, Ali U, Keshavarzkermani A, Mahmoodkhani Y, Marzbanrad E, Toyserkani E. On the effect of spatter particles distribution on the quality of Hastelloy X parts made by laser powder-bed fusion additive manufacturing. J Manuf Process 2019;37:11–20. https://doi.org/10.1016/j.jmapro.2018.11.012.

[102] Ferrar B, Mullen L, Jones E, Stamp R, Sutcliffe CJ. Gas flow effects on selective laser melting (SLM) manufacturing performance. J Mater Process Technol 2012;212:355–64. https://doi.org/10.1016/j.jmatprotec.2011.09.020.

[103] Reijonen J, Revuelta A, Metsä-Kortelainen S, Salminen A. Effect of laser focal point position on porosity and melt pool geometry in laser powder bed fusion additive manufacturing. Addit Manuf 2024;85:101030. https://doi.org/10.1016/j.addma.2024.104180.

[104] Ladewig A, Schlick G, Fisser M, Schulze V, Glatzel U. Influence of the shielding gas flow on the removal of process by-products in the selective laser melting process. Addit Manuf 2016;10:1–9. https://doi.org/10.1016/j.addma.2016.01.004.

[105] Meyers MA, Chawla KK. Mechanical behavior of materials. Cambridge university press; 2008.

[106] Nandi I, Ahmad N, Shamsaei N, Shao S. Revealing texture induced abnormal tensile deformation behavior in additively manufactured Haynes 282 using crystal plasticity simulations, 2022, p. 2271–81.

[107] Ahmad N, Ghiaasiaan R, Gradl PR, Shao S, Shamsaei N. Revealing deformation mechanisms in additively manufactured Alloy 718: Cryogenic to elevated temperatures. Mater Sci Eng A 2022;849:143528. https://doi.org/10.1016/j.msea.2022.143528.

[108] Tao P, Li H xue, Huang B ying, Hu Q dong, Gong S li, Xu Q yan. Tensile behavior of Ti-6Al-4V alloy fabricated by selective laser melting: effects of microstructures and as-built surface quality. China Foundry 2018;15:243–52. https://doi.org/10.1007/s41230-018-8064-8.

[109] Zhu L, Li N, Childs PRN. Light-weighting in aerospace component and system design. Propuls Power Res 2018;7:103–19. https://doi.org/10.1016/j.jppr.2018.04.001.

[110] Boyce BL, Salzbrenner BC, Rodelas JM, Swiler LP, Madison JD, Jared BH, et al. Extreme-Value Statistics Reveal Rare Failure-Critical Defects in Additive Manufacturing. Adv Eng Mater 2017;19. https://doi.org/10.1002/adem.201700102.

[111] Russell R, Wells D, Waller J, Poorganji B, Ott E, Nakagawa T, et al. Qualification and certification of metal additive manufactured hardware for aerospace applications. Addit Manuf Aerosp Ind 2019:33–66. https://doi.org/10.1016/B978-0-12-814062-8.00003-0.

[112] Yasin MS, Stonaker K, Shao S, Shamsaei N. Mechanical performance of laser powder bed

fused Ti-6Al-4V: The influence of filter condition and part location. Addit Manuf Lett 2024;11:100255. https://doi.org/10.1016/j.addlet.2024.100255.

[113] Maleki E, Bagherifard S, Unal O, Shao S, Shamsaei N, Guagliano M. Assessing the efficacy of several impact-based mechanical techniques on fatigue behavior of additive manufactured AlSi10Mg. Mater Sci Eng A 2023;872:144940. https://doi.org/10.1016/j.msea.2023.144940.

[114] Seifi M, Gorelik M, Waller J, Hrabe N, Shamsaei N, Daniewicz S, et al. Progress Towards Metal Additive Manufacturing Standardization to Support Qualification and Certification. Jom 2017;69:439–55. https://doi.org/10.1007/s11837-017-2265-2.

[115] Maleki E, Shamsaei N. A comprehensive study on the effects of surface post-processing on fatigue performance of additively manufactured AlSi10Mg: An augmented machine learning perspective on experimental observations. Addit Manuf 2024;86:104179. https://doi.org/10.1016/j.addma.2024.104179.

[116] Childerhouse T, Hernández-Nava E, Tapoglou N, M'Saoubi R, Franca L, Leahy W, et al. The influence of finish machining depth and hot isostatic pressing on defect distribution and fatigue behaviour of selective electron beam melted Ti-6Al-4V. Int J Fatigue 2021;147:106169. https://doi.org/10.1016/j.ijfatigue.2021.106169.

[117] Maleki E, Bagherifard S, Sabouri F, Bandini M, Guagliano M. Hybrid thermal, mechanical and chemical surface post-treatments for improved fatigue behavior of laser powder bed fusion AlSi10Mg notched samples. Surf Coatings Technol 2022;430:127962. https://doi.org/10.1016/j.surfcoat.2021.127962.

[118] Sun YY, Lu SL, Gulizia S, Oh CH, Fraser D, Leary M, et al. Fatigue Performance of

Additively Manufactured Ti-6Al-4V: Surface Condition vs. Internal Defects. Jom 2020;72:1022–30. https://doi.org/10.1007/s11837-020-04025-7.

[119] Of R, Draft T, Invited ARE, Comments WT, Any OF, Patent R, et al. ISO 25178-2:2021, Geometrical product specifications (GPS) — Surface texture: Areal — Part 2: Terms, definitions and surface texture 2021;2021.

[120] Edwards P, O'Conner A, Ramulu M. Electron beam additive manufacturing of titanium components: Properties and performance. J Manuf Sci Eng 2013;135:61016. https://doi.org/10.1115/1.4025773.

[121] du Plessis A, Yadroitsava I, Yadroitsev I. Effects of defects on mechanical properties in metal additive manufacturing: A review focusing on X-ray tomography insights. Mater Des 2020;187:108385. https://doi.org/10.1016/j.matdes.2019.108385.

[122] Martin AA, Calta NP, Khairallah SA, Wang J, Depond PJ, Fong AY, et al. Dynamics of pore formation during laser powder bed fusion additive manufacturing. Nat Commun 2019;10:1987. https://doi.org/10.1038/s41467-019-10009-2.

[123] Donachie J, M J. Titanium – A Technical Guide. vol. 55. Second Edi. 2000.

[124] Jeong D, Kwon Y, Goto M, Kim S. High cycle fatigue and fatigue crack propagation behaviors of β-annealed Ti-6Al-4V alloy. Int J Mech Mater Eng 2017;12:1–10.

[125] Oh J, Lee JG, Kim NJ, Lee S, Lee EW. Effects of thickness on fatigue properties of investment cast Ti-6Al-4V alloy plates. J Mater Sci 2004;39:587–91.

[126] Nakatani M, Masuo H, Tanaka Y, Murakami Y. Effect of Surface Roughness on Fatigue Strength of Ti-6Al-4V Alloy Manufactured by Additive Manufacturing. Procedia Struct

Integr 2019;19:294–301. https://doi.org/10.1016/j.prostr.2019.12.032.

[127] Bonneric M, Saintier N, El Khoukhi D, Bega J. Influence of the defect size, type, and position on the High Cycle Fatigue behavior of Ti-6Al-4V processed by laser powder bed fusion. Int J Fatigue 2025;193:108783. https://doi.org/10.1016/j.ijfatigue.2024.108783.

[128] Yoshinaka F, Nakamura T, Takaku K. Effects of vacuum environment on small fatigue crack propagation in Ti-6Al-4V. Int J Fatigue 2016;91:29–38. https://doi.org/10.1016/j.ijfatigue.2016.05.024.

[129] Rasoolian B, Pegues J, Shamsaei N, Silva D. An automated method for geometrical surface characterization for fatigue analysis of additive manufactured parts. Solid Free Fabr 2019 Proc 30th Annu Int Solid Free Fabr Symp - An Addit Manuf Conf SFF 2019 2019:2004–14.